Functional doped metal oxide films:
Zinc oxide (ZnO) as transparent conducting oxide (TCO)
Titanium dioxide (TiO_2) as thermographic phosphor and protective coating

Von der Fakultät für Ingenieurwissenschaften, Abteilung Maschinenbau und
Verfahrenstechnik der
Universität Duisburg-Essen
zur Erlangung des akademischen Grades

eines

Doktors der Naturwissenschaften

Dr.rer.nat.

genehmigte Dissertation

von

Abdelkader Nebatti Ech-Chergui
aus
Oran, Algerien

Gutachter: Uni.-Prof. Dr.rer. nat. Burak Atakan

Uni.-Prof. Dr.rer. nat. Volker Buck

Tag der mündlichen Prüfung: 29.07.2011

Abstract

There is a considerable interest in the use of doped metal oxides in the research and development of new materials and device applications, such as transparent conducting oxides (TCOs), thermographic phosphor, and protective coatings, among others. The present work deals with two promising metal oxides, namely, zinc oxide and titanium dioxide. These materials have gained substantial interest in the research community due to their usage in a wide variety of potential applications.

Zinc oxide is a II-VI compound semiconductor with a wide band gap of 3.37 eV at room temperature. Its wide band gap makes it suitable for LED and LASER applications. Al-doped ZnO is emerging as a possible replacement of indium tin oxide films as TCOs due to its low cost, high electrical conductivity, high optical transparency and chemical stability. Based on their potential applications many researchers have explored a variety of deposition techniques to judge their industrial suitability. Metalorganic chemical vapor deposition (MOCVD) was used in the present work it is a promising method for the development of un-doped and doped zinc oxide (ZnO) films. Un-doped and Al-doped ZnO films were developed using two reactors: Halogen Lamp Reactor (HLR) (a type of Cold Wall Reactor) and Hot Wall Reactor (HWR), and a comparison was made between them in terms of the film properties. Zinc acetylacetonate was used as precursor for ZnO films while aluminum acetylacetonate was used for doping. These precursors are inexpensive, so low-cost films can be achieved. The amount of

Al doping can be controlled by varying the gas flow rate. Well–ordered films with aluminum content between 0 and 8 % were grown on borosilicate glass and silicon. The films obtained are 0.3 to 0.5 µm thick, highly transparent and reproducible. The growth rate of ZnO films deposited using HLR is less than HWR. In HLR, the ZnO films are well oriented along c-axis ((002) plane). ZnO films are commonly oriented along the c-axis due to its low surface free energy. On the other hand, the HWR films are polycrystalline and with Al doping these films aligned along the a-axis ((100) plane) which is less commonly observed. The best films were obtained with the HLR method showing a minimum electrical resistivity of 2.4 mΩcm and transmittance of about 80 % in the visible range. The results obtained for Al-doped films using HLR are promising to be used as TCOs.

The second material investigated in this work was un-doped and doped titanium dioxide (TiO_2) films- its preparation and characterization. It is well known that thermographic phosphors can be used as an optical method for the surface temperature measurement. For this application, the temperature-dependent luminescence properties of europium (III)-doped TiO_2 thin films were studied. It was observed that only europium doped anatase films show the phosphorescence. Rutile phase do not show phosphorescence. The films were prepared by the sol-gel method using the dip coating technique. The structures of the films were determined by X-ray diffraction (XRD). The excitation and the emission spectra indicate that the red characteristic emission of $TiO_2 : Eu^{3+}$ due to electric dipole $^5D_0 \longrightarrow ^7 F_2$transition occurring after ultraviolet excitation is the strongest. The decay time of the phosphorescence after UV excitation with a Nd:YAG laser (355 nm, f=10Hz) is temperature dependent in the range from 200°C up to 400°C. The results demonstrate that anatase doped europium (III) can be considered as a thermographic phosphor in this temperature regime. Finally, it has been found that the lifetime show a significant dependency on europium concentration.

Titanium dioxide films are also interesting as protective coating, thus the development of rutile phase of titanium dioxide films on stainless steel substrates as protective coatings were investigated. Generally the rutile phases of TiO_2 thin films do not adhere well on stainless steel substrates. In order to improve the adhesion, stainless steel substrates were first coated with titanium films using cathodic vacuum arc deposition. Then these titanium coatings were partially transformed to the rutile phase of titanium dioxide by thermal oxidation. The presence of the rutile phase of titanium dioxide and metallic titanium were confirmed by XRD. Cavitation erosion was used for the first time to investigate the adhesion properties of these coatings. Cavitation erosion tests confirmed that rutile films with a Ti inter layer are well adherent to stainless steel substrates and protect the substrate from erosion. The total mass loss of the thermally oxidized samples of Ti coated stainless steel was found around 3.5 times lower than of the uncoated samples.

Kurzfassung

Dotierte Metalloxide erfahren ein großes Interesse in der Forschung und Entwicklung neuer Materialien wie zum Beispiel als transparente, leitende Oxide (TCOs, transparent conducting oxides), thermographische Phosphore und als Schutzfilme. Die hier vorgestellten Arbeiten befassen sich mit zwei sehr viel versprechenden Oxiden: Zinkoxid und Titandioxid. Diese Materialien sind in den Fokus einer Reihe von Forschungsvorhaben gekommen, da sie für eine Vielzahl möglicher Anwendungen interessant sind.

Zinkoxid (ZnO) ist ein II-VI Verbindungshalbleiter mit einer breiten Bandlücke von 3,37 eV bei Raumtemperatur. Aufgrund dieser breiten Bandlücke ist es sowohl für LED als auch für Laser Anwendungen geeignet. Aluminium-dotiertes ZnO entwickelt sich zu einer möglichen Alternative zu Indium-Zinnoxid-Filmen als TCO aufgrund seiner niedrigen Kosten, hoher elektrischer Leitfähigkeit, hoher optischer Transparenz und chemischer Stabilität. Eine Reihe unterschiedlicher Abscheidungsverfahren wurden in den letzten Jahren erforscht, um ihre Eignung zur industriellen Anwendung zu bewerten. In dieser Arbeit wurde die Metall-organische chemische Gasphasenabscheidung (MOCVD, metalorganic chemical vapor deposition) verwendet, was eine sehr viel versprechende Methode zur Herstellung von dotierten und undotierten ZnO-Schichten ist. Undotierte und Al-dotierte ZnO Schichten wurden mit zwei unterschiedlichen Reaktoren hergestellt: einerseits mit einem Halogen-Reaktor, was eine Art

von Kaltwandreaktor ist, und andererseits mit einem Heißwandreaktor. Die beiden Verfahren wurden auf Basis der Eigenschaften der produzierten Schichten miteinander verglichen. Zink-acetylacetonat wurde als Vorläufer für die ZnO-Schichten verwendet, während Aluminium -acetylacetonat zur Dotierung benutzt wurde. Diese Vorläufer sind kostengünstig, so dass günstige Schichten produziert werden können. Die Menge an Al-Dotierung kann durch den Gasdurchfluss kontrolliert werden.

Gutgeordnete Schichten mit einem Aluminiumgehalt zwischen 0 und 8 % wurden auf Borosilikatglas und auf Silizium abgeschieden. Die Schichten hatten eine Dicke zwischen 0,3 und 0,5 µm und waren hochtransparent und reproduzierbar. Die Wachstumsrate von ZnO-Schichten ist geringer im Halogenreaktor im Vergleich zum Heißwandreaktor. Im Halogenreaktor waren die ZnO Schichten gut entlang der c-Achse ((002) Ebene) orientiert. ZnO-Schichten sind üblicherweise entlang der c-Achse orientiert aufgrund der dann geringen freien Oberflächenenergie. Auf der anderen Seite sind die Heißwandreaktor-Schichten polykristallin und mit Al-Dotierung entlang der a-Achse ((00)1 Ebene) orientiert, was seltener beobachtet wird. Die besten Schichten wurden mit dem Halogenreaktor realisiert. Diese haben einen minimalen elektrischen Widerstand von 2,4 mΩcm und eine optische Durchlässigkeit von ca. 80% im sichtbaren Bereich. Die Ergebnisse für die Al-dotierten Schichten aus dem Halogenreaktor sind vielversprechend für eine Nutzung als TCO.

Das zweite Material, was in dieser Arbeit untersucht wurde, ist dotiertes und undotiertes Titandioxid (TiO_2). Dabei wurde sowohl die Herstellung als auch die Charakterisierung der Schichten betrachtet. Es ist weithin bekannt, das thermographische Phosphore als optische Methode zur Oberflächentemperaturmessung eingesetzt werden können. Für diese Anwendung werden die Temperatur abhängigen Lumineszenzeigenschaften von Eurorpium-(III)-dotieren TiO_2 Schichten untersucht. Dabei wurde festgestellt, dass nur die Europium-dotierten Anatas-Schichten eine Phosphorenz aufweisen, wohingegen die Rutil-Phase nicht phosphoresziert. Die Filme wurde mit einer Sol-Gel-Methode hergestellt. Die Struktur der Filme wurde mittels Röntgenstrahlen analysiert. Die Anregungs- und Emissionsspektren legen nahe, dass die rote charakterisches Emission von $TiO_2 : Eu^{3+}$ aufgrund des $^5D_0 \longrightarrow ^7F_2$ Dipolübergangs nach einer Anregung im UV Bereich am stärksten ist. Die Abklingzeit der Phosphoreszenz nach der Anregung mit einem Nd:YAG Laser (355mm, f=10Hz) ist im Bereich von 200°C bis 400°C temperaturabhängig. Die Ergebnisse zeigen, dass Europium-dotiertes Anatas als ein thermographischer Phosphor in diesem Temperaturbereich angesehen werden kann. Außerdem wurde gezeigt, dass die Phosphoreszenzlebensdauer eine signifikante Abhängigkeit von der Europiumkonzentration hat.

Titanoxidschichten sind außerdem interessant als Schutzschichten. Ihre Eignung als Schutzschicht wurde anhand der Rutil-Phase von TiO_2 auf Edelstahlproben untersucht. Normalerweise haftet Rutile nicht gut an Edelstahlproben. Um die Haftung zu verbessern, wurden die Proben zunächst mit Titan beschichtet, wobei Vakuumkathaporese verwendet wurde. Durch thermische Oxidation wurden diese Titanschichten teilweise in die rutile Phase von Titandioxid umgewandelt. Mithilfe von XRD wurde gezeigt, dass diese Filme aus der Rutilen Phase von TiO_2 und metallenem Titan bestehen. Kavitationserosion wurde erstmals benutzt, um die Haftungseigenschaften dieser Schichten zu untersuchen. Dabei konnte bestätigt werden, dass rutile Schichten mit einer Ti-Zwischenschicht sehr gut an Edelstahl haften und die Probe vor Erosion schützen. Der Gesamtmassenverlust der thermisch oxidierten Ti-beschichteten Edelstahlproben war ca. 3,5 mal niedriger als der der unbeschichteten Proben.

Acknowledgement

As the formal completion of my doctoral studies in the Department of Thermodynamic is under way, I am very pleased to have the honor to express my gratitude from the pages of my thesis to all those who were involved in this journey in research and applied knowledge.

Initially, I would like to thank my thesis adviser, Professor Burak Atakan, who gave me the opportunity to join his group. I feel gratitude for his continuous support and encouragement that helped me overcome the disappointments that are so abundant in any experimental problem.

I am also grateful and indebted to Priv.-Doz. Dr. Christian Pflitsch for all his help and his guidance during this research.

I am especially indebted to Dr Susanne Staude ,Dr. Christopher Eckert, Mr Erdal Akyildiz and Dr. Ulf Bergmann, Mr Larid hasni, Dr Adjdir mehdi, Miss Rahmani rabea, Dr Amrani Bouhalouin with whom I engaged in vastly entertaining discussions. They always encouraged me and stand by my side whenever I needed them. Their contribution to the work presented in the next pages cannot be overstated. Last, but not least,

I would like to express my gratitude to all those who made me feel at home with their love, friendship, and care, and especially to Dipl.-Ing. Andreas Görnt and Mr.

Manfred Richter. Of course, I will always be indebted to my old friends at home and abroad. Finally, I would like to express my deep gratitude and love to my mother (fatima), father(Lakhdar), brothers (Kouider, Omar, Abdelrahman, Bilal) for their unconditional trust and multifaceted support through all these years.

Finaly, I acknowledge supports from Deutscher Akademischer Austausch Dienst (DAAD) for the scholarship in the program Research Grants for Doctoral Candidates under the matriculation: A/06/91318

(Abdelkader Nebatti Ech-Chergui)

Contents

5 Deposition of un-doped and doped TiO_2 films 117

List of Figures

List of Tables

1 Introduction

Thin films are microscopically thin layer of materials deposited onto substrates to achieve properties unattainable or not easily attainable in the substrate alone. In thin films, deviations from the properties of the corresponding bulk materials arise because of their thickness, large surface-to-volume ratio, and unique structure which are a direct consequence of the growth process. Thin films normally show different properties than the bulk materials because of many factors such as smaller crystallite size, enhanced crystallographic defects such as, dislocations, vacancies, grain boundaries, etc. thin films are preferred in a variety of applications, such as in reflective/antireflective coatings [8, 9, 10], decorative coatings [11, 12, 13], transparent conducting oxides [14, 15, 16], triboligical coatings [17, 18], memory devices [19, 20], etc.

1.1 Introduction to functional metal oxide films

Metal oxide films are observed to have a variety of functionalities which provide a rich platform for exploring novel device applications. There are many metal oxide systems which have traditionally been used as important device materials like transparent conducting oxides, temperature sensors, dielectric insulators, phosphors, etc. The metal oxide materials specific to this thesis are introduced in the following.

1.1.1 Zinc oxide (ZnO) thin films

Zinc oxide is a II-VI compound semiconductor with a wide band gap of 3.37 eV at room temperature [21]. ZnO has gained substantial interest in the research community because of its use in diverse commercial applications such as paint pigment, as ultra–violet absorber in cosmetic and polymers, as transparent thin film transistors, transducers, and so on. It's wide band gap makes it an appropriate candidate for UV-LEDs and LASER. With small amount of doping with elements like aluminium (Al), Gallium (Ga), Boron (B), etc., its electrical conductivity can be tailored significatly without effecting its optical transparency. Al-doped ZnO is emerging as a suitable replacement for indium tin oxide (ITO) films due to its low cost, high electrical conductivity, chemical stability, abundant raw materials, and non toxic features [22, 23]. In addition, Al seems to be promising for doping ZnO because the covalent bond length of Al-O (0.192 nm) is only slightly smaller than that of Zn-O (0.197 nm)[24] . For this reason aluminum can be doped easily in a ZnO lattice. Hence, it's easy to fabricate.

The motivation behind choosing ZnO, with Al as dopant in this work stems from its applications in potential optical devices and as transparent conducting oxides, for which ZnO is well suited. Keeping the potential market of these applications in mind, it is obvious that the development of low-cost and powerful deposition techniques is important. Until now, several strategies have been followed to deposit thin zinc oxide films, including wet chemical methods like sol-gel deposition [25] and spray pyrolysis [26]. Also physical vapor deposition, such as rf-magnetron sputtering and molecular beam epitaxy (MBE), or chemical vapor deposition (CVD) have been used [27]. Rees et al [3] has given a brief review on the above mentioned techniques. Among these techniques, metal-organic chemical vapor deposition (MOCVD) is a versatile method for the preparation of high quality films with high deposition rates [28]. MOCVD techniques are known due to their versatility in controlling the various thermodynamic interactions involved in films deposition [28]. For the present work, MOCVD techniques with two different types of reactors, namely a halogen lamp reactor (a type of cold wall reactor) and a hot wall reactor have been used. Cold wall reactors allow better control over the deposition process and thus produce films with high reproducibility. In cold wall reactors, high intensity radiation lamps or electric heating is generally used for substrate heating. For the present work, the light irradiation using tungsten halogen lamps was used for substrate heating. Light irradiation not only can raise the substrate temperature by the absorption of light, especially the infrared photons, but also can cause thermal decomposition of the source precursor in the gas phase and substrate surface. There are a variety of light sources for light irradiated MOCVD such as mercury lamps [29] excimer lasers [30], tungsten halogen quartz lamps [31]. Tungsten-halogen lamps were used for the first time by Nishiyama et al [32], in 1980 as a continuous source of radiation for annealing boron implanted wafers. Since then this technique has been extended for many other processes [31]. There are very few reports on the deposition of un-doped ZnO films using halogen lamp reactors [33]. It is also noteworthy that Al-doped ZnO films has not been deposited using halogen lamp reactor so far. As such, the potentials of the halogen lamp reactor in developing un-doped and Al-doped ZnO films were investigated here in terms of their optical and electrical properties. Zinc and aluminum acetylacetonate were used as precursors. Very few literatures are available specifying the use of such precursors in the deposition of ZnO and Al-doped ZnO. Such precursors have been used because they are commercially available, cheap, non toxic and easy to handle. High purity nitrogen was used as a carrier gas while high purity oxygen as oxidant. Along with various advantages there are a set of limitations associated with HLR. Although, halogen lamp reactor produce high quality films, one can deposit only one sample at a time. Another type of reactor i.e. a hot wall reactor, is less costly, simple to operate and can deposit several samples in one deposition. It can also deposit films on complex shapes. Thus, hot wall reactor deposition was also investigated for developing un-doped and Al- doped ZnO films. The precursor used were the same as in case of halogen lamp reactors but only synthetic air was used for the deposition process in order to reduce the production cost.

1.1.2 Titanium dioxide (TiO_2) thin films

Titanium dioxide is one of the most excellent materials that have attracted much interest due to their interesting chemical and physical properties [34]. This make it useful for several applications in wide field of engineering, such as protective layers or hard coatings [35, 34], interference coatings [36], solar cells [37, 38], gas sensors [39, 40], as photo catalysts [41, 42], etc. The properties of films are strongly influenced by the crystal structure of TiO_2, which can occur in several phases. The mostly observed phases are rutile, the stable phase of titanium dioxide, and anatase, which is a metastable phase [34]. While rutile is mostly used as hard coating, the anatase has other applications, such as photocatalysts or component of dye-sensitized solar cells. [43, 44, 45]. The catalyst reaction take place on the surface of the catalyst and are in general temperature dependent, hence it is necessary to know the surface temperature in order to characterize the reaction. Therefore multifunctional coatings on the base of titanium dioxide (TiO_2) can be produced primarily as catalyst and secondly as thermographic phosphor (as an additional feature). It is necessary to dope the host material (TiO_2,) with an activator ion, like europium (used in the present case), to achieve phosphorescence which indicates the temperature. To my knowledge, doped titanium dioxide has not yet been investigated for this application. Apart from this work, un-doped TiO_2 films on stainless steel substrates were also studied as protective coatings. Due to its wide variety of applications,many techniques have been investigated to deposit TiO_2 films till date. These include metal organic chemical vapor deposition [46], ion-assisted deposition [47], chemical spray pyrolysis [48], sputtering [49], thermal oxidation [50], and sol–gel process [51, 52]. For the present work, two methods were used for the preparation of titanium dioxide. Firstly, a sol gel method followed with dip coating technique were used to prepare undoped and europium doped films. Sol gel method has been used as it is cheap, do not need complex system for synthesis and is capable of producing films with better reproducibility, controllability and reliability. Secondly, attempts have been made to deposit titanium coatings onto stainless steel substrate by cathodic vacuum arc, and then to convert the titanium coatings to titanium dioxide TiO_2 by thermal oxidation. By this process highly adhesive and pure rutile phase titanium dioxide films were obtained which are the desirable features for protective coatings.

1.2 Outline of the thesis

The present thesis includes six chapters and is organized as follows:

Chapter 2 presents the theory of the various deposition techniques used for developing films in the present work. It also discusses the parameters associated with the experimental representation of various structural, compositional, optical and electrical properties of such films. The theories of the preliminary characterization techniques for the determination of such parameters are briefly stated. At the end of the chapter a brief overview of ZnO and TiO_2 is also presented.

Chapter 3 illustrates the experiments that were carried out in the course of this work. This includes the description of the experimental setups of the reactors used for deposition like the halogen lamp reactor which is a type of cold wall reactor, hot wall reactor, etc. This chapter also describes the instrumentations involved in the characterisation of the films.

Chapter 4 investigates un-doped and Al-doped ZnO films deposited using metal organic chemical vapour deposition (MOCVD) on silicon and borosilicate glass substrates as transparent conducting oxides (TCOs). This chapter is broadly divided into two sections: one for films deposited using halogen lamp reactor and the other for films deposited using a hot wall reactor. This chapter also remarks a comparative description of the structural, optical and electrical properties of these films deposited using these two above mentioned systems.

Chapter 5 explores the possibility of another functional oxide material, TiO_2, as temperature sensor and as protective coating. Two deposition techniques were chosen to obtain pure anatase and pure rutile phase which are specific for such applications. These techniques are sol gel and cathodic vacuum arc. For temperature sensor application, anatase-TiO_2 was doped with europium (Eu) while for protective coatings Ti films were thermally oxidized to obtain pure rutile phase.

Chapter 6 concludes the thesis and summarizes the results. At the end, future scope of the present work was presented

2 Theoretical background

This chapter reviews the theoretical concepts that are related to the work presented in this thesis. Firstly, different possibilities to deposit thin films are introduced with three techniques are presented in details, such as chemical vapor deposition (CVD), sol-gel, cathodic vacuum arc deposition (CVA). The used film characterisation methods are described, such as x-ray diffraction (XRD), scanning electron microscopy (SEM), energy dispersive x-ray spectroscopy (EDX), resistivity, and the photoluminescence (PL), followed by a description of essentials of luminescence lifetime thermometry as results of fluorescence emission. In the last section, an overview of the principles properties of titanium dioxide TiO_2 and zinc oxide ZnO films and applications, relevant to these materials, are presented.

2.1 Film deposition techniques

A large number of deposition techniques exist for the deposition of thin films in the range of a few nanometres to some micrometers. The selection of a specific process for the formation of films can be based on a variety of considerations, for example :

- Material of interest
- Properties needed
- Cost

- Growth rate
- Adhesion to substrate
- Purity of the film
- Ecological considerations[53].

Each of the methods has its own advantages and disadvantages and often more than one method could be used to deposit a specific film. A classification scheme is presented in Figure 2.1 where we have grouped thin film deposition according to physical or chemical deposition process. Thin film deposition could be classified as given below.

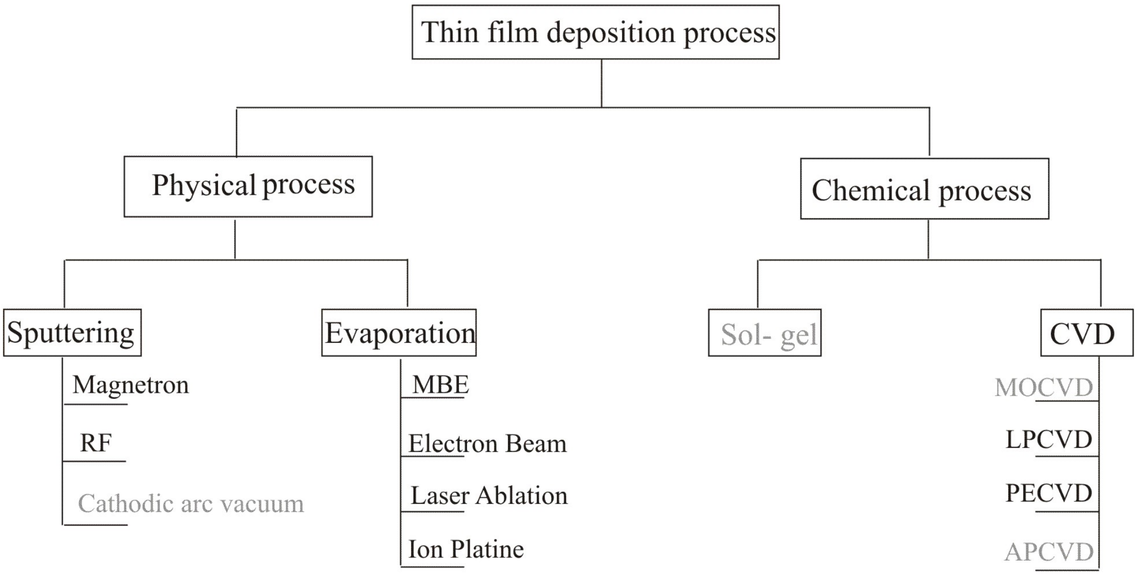

Figure 2.1: Overview of thin film deposition techniques [1]. RF (Radio Frequence), CVD(Chemical Vapor Deposition), MOCVD (Metal Organic Chemical Vapor Deposition), LPCVD (Low Pressure Chemical Vapor Deposition), PECVD (Plasma Enhaced Chemical Vapor Deposition), APCVD (Atmospheric Pressure Chemical Vapor Deposition)

2.1.1 The Chemical vapour deposition (CVD)

The chemical vapor deposition process is used for deposition of thin films on a substrate material by gas phase chemical reaction of vapor phase precursor. The process involves evaporation of precursor molecules. The vapor of the precursor is carried with a help of carrier gas to a substrate. There the thermal energy is provided to initiate the chemical reaction for the formation of a thin film. The basic process steps in CVD are shown schematically in Figure 2.2 and are summarized in the following sequence [2] :

(1) Vaporization of the precursor.

(2) Transport of the precursor molecules into the reaction chamber by a help of carrier gas.

(3) Gaseous reactants undergo gas phase reactions forming intermediate species :

(a) At higher temperatures, above the decomposition temperature of the precursor in the gas phase, homogeneous gas phase reaction can occur. The powder will be collected on the substrate surface and may act as crystallisation centres, and the by-products are transported away from the deposition chamber. The deposited film may have poor adhesion.

(b) In contrast, at temperatures below the decomposition temperature of the precursor, heterogeneous gas phase reaction can occur. A thin layer is obtained due to diffusion of the precursor through the boundary layer.

(4) Adsorption of gaseous reactants onto the heated substrate, and the heterogeneous reaction occurs at the gas-solid interface (i.e. heated surface) which produces the deposit and by-product species.

(5) The deposits will diffuse along the heated substrate surface forming the crystallisation centre and growth of the film.

(6) Gaseous by-products are removed from the boundary layer through diffusion.

(7) The waste by-products are transported away from the deposition chamber.

It should be noted that for the deposition of dense films and coatings, the process conditions are adapted to favour the heterogeneous reaction (3b) step (see the Figure

2.2). While, a combination of heterogeneous and homogeneous gas phase reaction is preferred for the deposition of porous coatings.

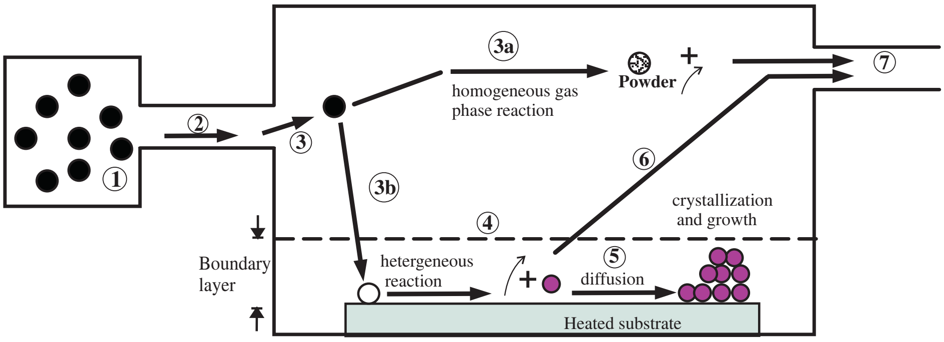

Figure 2.2: A schematic illustration of the key CVD steps during deposition [2]

2.1.1.1 Growth kinetics of the CVD-process

Chemical vapour deposition (CVD) is a non equilibrium process. The kinetics of the CVD process involves chemical reactions in the gas phase, on the substrate surface, chemisorptions and desorption. Ideally, the chemical kinetics of a CVD process could be derived from the analysis of all possible reaction pathways including those sequential and competing reactions. Surface reaction and chemical reaction in the gas must ideally be described by their rate equation. In general the global reaction rate is limited by the slowest reaction step. Three different cases can be distinguished [2].

1. At lower growth temperatures the growth rate is controlled by the kinetics of chemical reactions occurring either in the gas-phase or on the substrate surface. This region is generally termed the region of kinetic growth control and the film growth rate increases exponentially with substrate temperature according to the Arrhenius equation2.1

   $$k = k_0 \exp\left(\frac{-E_a}{RT}\right) \tag{2.1}$$

   Where k is growth rate , E_a is the apparent activation energy, R is the gas constant and T is the temperature.

2. At higher growth temperature, the growth rate becomes nearly independent of temperature and is controlled by the mass transport of reactents through the boundary layer to the growth surface, and this is termed the region of mass transport or diffusion-controlled growth.
3. At even higher temperature a decrease in the growth rate is observed due to the depletion of reactants [2]. At these high temperatures homogeneous reaction in gas can occur in addition to heterogeneous reaction on the substrate surface. This process gives rise to the formation of particles in the gas phase and to the reduction of the film growth and will, therefore, affect the adherence of the film.

It should be mentioned that an Arrhenius plot as in Figure 2.3, has to be used to obtain an activation energy for a kinetic process. The slope of the ‘‘kinetic region’’will give a value of the activation energy which is the amount of energy required to start a chemical reaction .

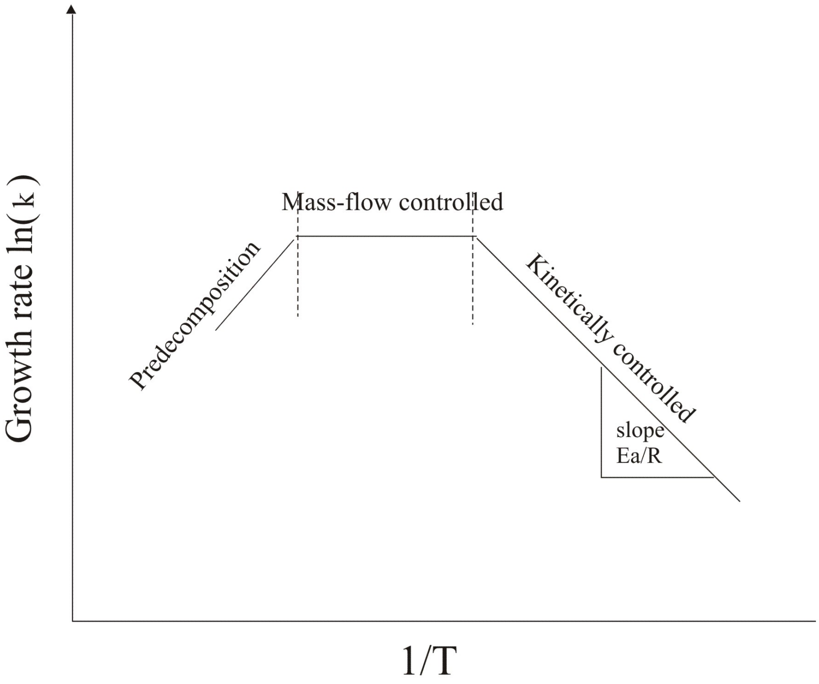

Figure 2.3: Arrhenius plot behaviour of deposition rate [3]

In general, in CVD processes thermal energy is used to initiate chemical reactions. However, the chemical reaction can be initiated using different types of energy sources. This has given rise to other variants of the CVD methods such as photo-assisted CVD (PACVD) and plasma enhanced CVD (PECVD) which uses light and plasma, respectively, to activate chemical reactions. In conventional CVD methods inorganic precursors are generally used (for example metal hydrides, Halides). These precursors have the disadvantage of a very high decomposition temperature. This disadvantage had been overcome by using metalorganic or organometalic compound which allow relatively low decomposition temperature and uniform deposition over large area. The variant of CVD process where metalorganic precursors are used is called MOCVD. CVD is widely used for deposition of high quality thin films with well defined structure uniformity (surface morphology and orientation). This method has the capability of producing highly dense and pure films with good reproducibility and very good substrate adhesion at reasonably high deposition rate. The main disadvantage of this method includes the use of toxic, corrosive, flammable and some times explosive precursors [28, 2]. The other difficulty is to deposit multicomponent material with well controlled stiochiometry (controled doping) due to different vaporization rates of the precursors.

2.1.1.2 Metalorganic chemical vapour deposition (MOCVD)

As previously mentioned, MOCVD is a variant of CVD, which has been classified according to the use of metalorganic compound as precursors. MOCVD can be used to deposit a wide range of materials as almost every metallic element has a known volatile organometallic compound. Good MOCVD precursors should have following qualities

- Good volatility

- High purity
- Good thermal stability during the evaporation and transport process in the gas phase
- Non-toxic, non-explosive, and inflammable.

There are five categories of metalorganic compounds which are frequently used :

1. Alkoxide, such as ethoxide, isoproxide and butoxide
2. Alkylmetal, such as ethylzinc and phenylbismuth
3. Metal carbonyl
4. Metal cyclopentadienyl
5. Metal β-diktonates, such as 2,2,6,6-tetramethyl-3, 5-heptanedioate (thd).

Among the above mention compound metal β-diketonates and metal cyclopentadienyl compounds are commonly used precursors for MOCVD process. These precursors are commercially available at very cheap price and posses all the desirable qualities of good MOCVD precursors.

Acetylacetonate compounds Metal acetylacetonate or shortened (M-ac.ac) where M= Al, Zn, Cu, etc , also known as pentanedionates, are produced by reacting metals and acetylacetone [28]. They have the following chemical structure 2.4 :

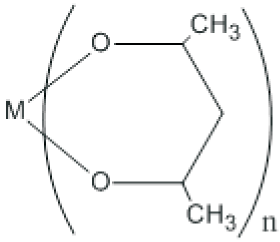

Figure 2.4: Chemical structure of Metal acetylacetonate (M-ac.ac)

The acetylacetonates are stable in air and readily solube in organic solvents. From this standpoint, they have the advantage over the alkyls and other alkoxides, which, with the exception of the iron alkoxides, are not as easily soluble. They can be readily synthesized in the laboratory. Many are used extensively as catalyst and are readily available. they are also used in CVD in the deposition of metals such as iridium, scandium and of metal oxide, such as aluminium oxide, zinc oxide, and thin oxide etc. Acetyacetonates are commercially available [28].

2.1.1.3 Features of Hot- and Cold-wall reactors

The chemical vapor deposition reactors are often differentiated by the method employed for heating the substrate [54].

In a hot wall reactor (HWR), the reactor is surrounded by a heating source, often a tube furnace [3]. I summarise the advantages of hot wall systems in the following. First, they are very simple to operate. Furthermore, in this system the coating of several substrates with different orientation and position relative to the flow direction can be produced. The main problem is that deposition can occur not only on the substrate but also on the reactor walls. Consequently, these deposits will eventually contaminate the substrate surface. This can lead to the problems of reproducing deposition conditions because the fraction of the reactor surface area can change with time during an experiment and from one experiment to another. Nevertheless, industry utilizes them sometimes for CVD of various materials when the vapour pressure of the precursor is high [55].

In a cold-wall reactors, the substrate to be coated is heated directly either by induction or by radiant heating i.e halogen lamps while the walls of the reactor are kept at lower temperature than the substrate [3, 28]. Since the risk of depositing a film on the reactor wall is reduced, the quantity of precursor required is generally smaller and the deposition rate increases significantly compared to the previous types of reactor. Moreover, cold-wall reactors are more suitable for selective CVD and to measure kinetic parameters [55].

Finally, it should be noted that, in this work, the MOCVD of un-doped and aluminum doped Zinc oxide (ZnO) have been carried out in two reactors one is a “Halogen lamp reactor” (HLR), which is a type of a cold-wall and the other a hot-wall reactors (HWR).

2.1.1.4 Thermal analysis theory

CVD processes involve the evaporation of the precursors. For obtaining high quality, reproducible and uniform films, it must be ensured that during the evaporation no decomposition of the precursor takes place. Recently a method to quantify the thermal stability of precursors using a thermogravimetric analysis was described by our research group. (The detail of the method is described elsewhere [56]). In this work the same methodology was used to study the thermal stability of the metalorganic precursors. The experiments for all the precursors were done in non isothermal mode where the temperature was raised as a function of time. The attention was paid to amount of the residue. If a single step curve is obtained for mass loss versus time plot and substance evaporates without leaving any residue, (or if some residue is found, then it should be below 5%) it is then considered to be a thermally stable substance and used for CVD experiments. If the mass loss with time is not constant i.e. evaporation proceeds in multi-steps and also when the substance leaves a considerable amount of residue, then it means that the evaporation might be accompanied by the decomposition of the substance. Generally a sharp endothermic peak from the DTA signal is the indication of a melting point of the sample whereas exothermic/ endothermic peaks corresponds to the decomposition of the substance.

2.1.2 The sol-gel method

The sol gel method is a wet chemical deposition process for preparation of thin films. The process consists of preparation of the precursor sol (colloidal solution). The precursor sol is deposited on to a substrate to form a film by spin coating or dip coating which is then heated (see figure 2.5). The heat treatment of the deposited films is carried out in two steps in most cases. For the first step, a pre-heat treatment (40–500°C) is applied during a short time for solvent evaporation and organic compounds removal [57, 58, 59, 60, 61]. The second step, an annealing treatment is done in order to obtain a well-crystallized films and the final decomposition of organic by-products.

In general, sol –gel processing can also be done with a variety of precursors[62, 63]. The sol-gel chemistry can be described in terms of two classes of reactions [64]

1. An initiation reaction, a hydroxylation of a metallic alkoxide via hydrolysis

   $$M\left(OR\right)+H_2O\rightarrow HO-M\left(OR\right)_{n-1}+ROH \tag{2.2}$$

   (M(OR)n) as a precursors (where M is a metal)

2. A propagation or condensation reaction

   $$\left(OR\right)_{n-1}M-OH\dot{+}HO-M\left(OR\right)_{n-1}\rightarrow\left(OR\right)_{n-1}M-OM\left(OR\right)_{n-1}+H_2O \tag{2.3}$$

   $$\left(OR\right)_{n-1}M-OR+HO-M\left(OR\right)_{n-1}\rightarrow\left(OR\right)_{n-1}M-OM\left(OR\right)_{n-1}+ROH. \tag{2.4}$$

Sol gel method has the following distinctive advantages in comparison with other deposition methods :

- Since liquid precursors are used it's possible to coat complex shapes.
- Simple operative procedure (no complex reactor system).

- Precise doping is easily achieved.
- Cheap precursor material is available commercially.

Despite all the advantages ; the sol-gel method still has some limitations. Solvents, such as alcohol and water, are involved in the process, so it's not appropriate for fabrication for substrates which are very sensitive to solvents. Additionally, stress induced cracks appears after pre-heat treatment and which remain even after densification. Very careful attention is needed to avoid cracking, then a very slow pre-heat treatment has to be applied. Despite of the disadvantages, the sol-gel method is a very simple and flexible method for fabrication of thin films that possess properties (precise dopant concentration) not attainable by other methods.

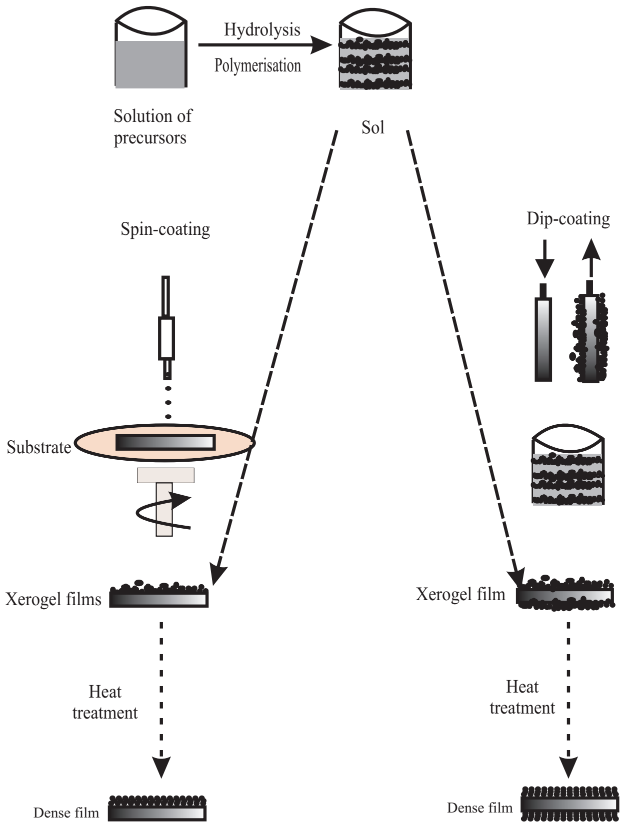

FIGURE 2.5: The sol–gel method ; Spin-coating and Dip-coating

2.1.3 The cathodic vacuum arc theory

Cathodic arc deposition is a plasma-based technology for the fabrication of thin films. In this technique an electrical arc discharge is used to vaporize material from the surface of the cathode. Such an arc discharge is termed as cathodic arc. A cathodic arc is a low-voltage, high-current plasma discharge that takes place between two metallic electrodes in vacuum. This deposition process can be carried out either at high vacuum or in a low pressure gaseous environment. Figure **??** shows a schematic representation of the phenomena occuring in a cathodic arc deposition.

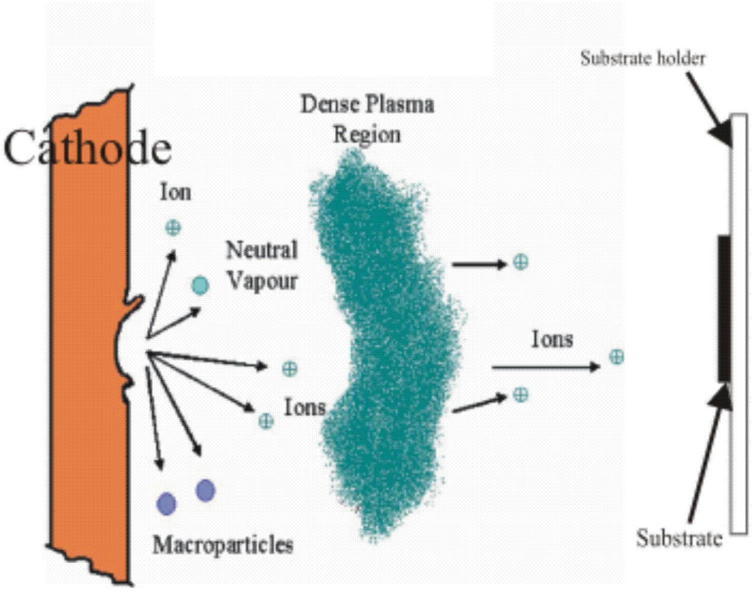

Figure 2.6: Diagramm of the cathodic arc spot with the generation of plasma

When an arc discharge is generated under medium and higher vacuum, in general, a cathode spot is formed. The cathode spot is very active with high temperature and evaporates the cathode material. At the cathode spot region, a very dense plasma is generated, and the evaporated cathode material is ionized and the ions are deposited as a solid film upon reaching the solid surface. Such vacuum arc deposition is a major method in physical vapor depositions (PVDs) and has the advantage of higher ion energy, compared to the other PVD methods [65, 66]. The ion source of the arc cathode is generally a solid. Therefore, no crucible is needed, and the sources can be freely mounted on the wall of the process chamber. In principle, no gas introduction is necessary. However, vacuum arc deposition is suitable for reactive deposition because the ions generated in the vacuum are highly reactive with the gases due to their high energy. Cathodic arc deposition systems are in widespread use around the world for producing thin films of a variety of materials involving metals, metal oxides [67, 68], ceramics, diamond like carbon, some semiconductors and superconductors, and more [66, 69]. Its major industrial use is to make protective coatings on cutting/machining tools and sliding materials. Examples of film materials are TiN, TiC, CrN, and TiAlN [70, 69, 66, 71].

2.2 Film chacterisation techniques

The goal of any deposition process is a film or coating with specific properties, tailored to a particular need. which could be ascertained by film properties evaluation. This could be done by various film characterisation technique as given below. The structural properties of the films are studied by scanning electron microscopy (SEM) and the presence of crystalline phases are studied by x-ray diffraction (XRD). The chemical composition of the thin films were determined by energy dispersive x-ray spectroscopy (EDX). The optical properties of the films were evaluated by UV-Vis spectroscopy, while the electrical properties of the materials were investigated by standard four-point probe. A brief description of the theory and methodology of each characterization technique is given below.

2.2.1 X-ray Diffraction (XRD)

The structural characterisation of the deposited thin films were performed by X-ray diffraction. XRD is a routine method in materials science in the elucidation of structures and also to verify phase purity.

Interaction of X-rays with a sample creates secondary diffracted beams (actually generated in form of cones) of X-ray related to interplanar spacings in the crystalline powder according to a relation called Bragg's Law

$$2d \sin\theta = n\lambda \tag{2.5}$$

derived by W.H.Bragg and his son W.L Bragg in 1913 to explain why the cleavage faces of crystals appear to reflect X-ray beams at certain angles of incidence (θ). The variable d is the distance between layers in a crystal, and the variable λ is the wavelength of the incident x-ray beam (see Figure 2.7) ; n is an integer.

Diffractometers come in two basic geometries : theta-2theta geometry (called also detector scan or grazing incidence) in which the X-ray source (incident beam) and the sample are fixed, and the detector moves through a range of angles (see Figure 2.8a). This type of scan allows to identify the phase composition of the analyzed films if they are crystalline where the atoms of crystalline film are arranged in a regular pattern (see Figure 2.9a), while amorphous films where atoms are arranged in a random way (see Figure 2.9b) can not be analysed by X-ray diffraction. Concerning the information about the growth as preferred orientation is acquired by performing a Bragg scan analysis where both the X-ray source and the detector move in vertical plan in opposite directions above the centre of the sample, and the sample is fixed (see Figure 2.8b). This type of scan can give more information about possible preferred orientations.

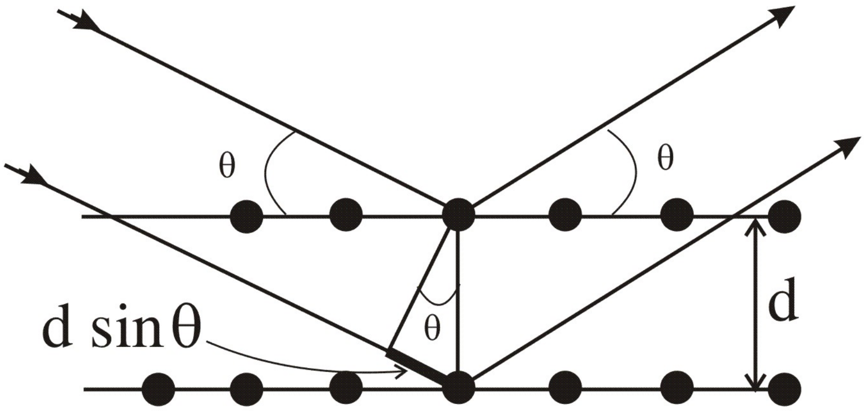

Figure 2.7: Schematic description of Bragg's Law

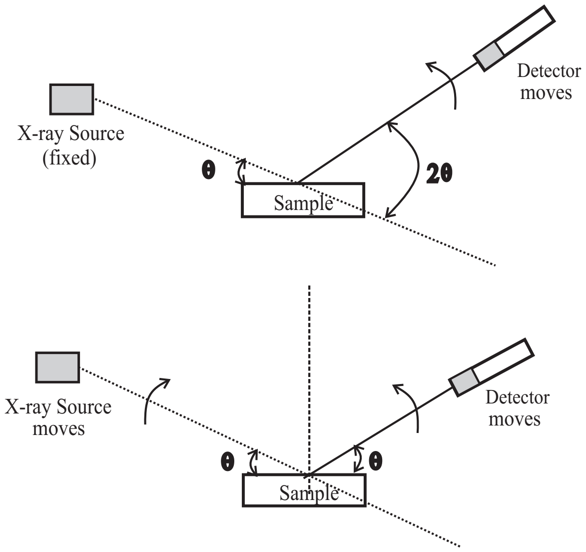

Figure 2.8: Geometry of XRD measurment ;(a)θ-2θ scans(detoctor scan or granzing incidence)(b)$\theta-\theta$scan (Braag scan)

The angle of the diffraction (recorded as 2θ by convention) is related to the interplanar spacing, d, by the Bragg law, and the intensity of diffraction maximum is related to the strength of those diffractions in the sample. A patterns of the reflections of the family of planes parallel to the sample surface is obtained. The analysis of this pattern permits the identification of the crystalline species. This identification is done by comparing the measured d- spacing in the diffraction patterns and, to, a lesser extent, their integrated intensities with known standards in the JCPDS Powder Diffraction File (Joint Committee on Powder Diffraction Standards, Swathmore, Pennsylvania 1986)[[72]

Finally, it should be noted that for the XRD measurements a Bruker - model D8 Advance X-ray the diffractometer working with Cu radiation (λ =1.5406 , (CuKα) was used in the present work. The working conditions were typically : 2θ scanning between 20° and 80°, with 0.07° step.

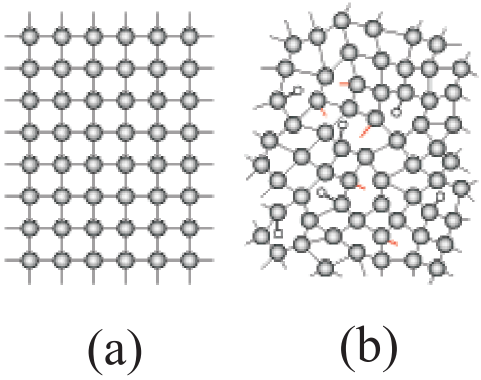

Figure 2.9: a)Crystalline form, b) amorphous form

2.2.2 Morphology and chemical composition

2.2.2.1 Scanning electron microscopy (SEM)

Scanning electron microscope is one of the most widely used instruments for morphological studies. In SEM, an electron beam is focused (in vacuum) into a fine probe that is rastered over the surface of the sample. As the electron beam penetrates the surface a number of interactions occur which leads to the generation of electrons and X–ray photons [73]. Figure 2.10 show a schematic of such interactions of a sample with a well collimated beam of accelerated electrons. These energetic electrons interact with the sample both elastically and inelastically. In elastic collision, the electron beam suffers only a deviation in its trajectory without changing the energy. Backscattered electrons are the examples of elastic scattering [74]. Backscattered electrons are used to form diffraction images, called electron backscattered diffraction (EBSD) image that describe the crystallographic structure of the sample. In inelastic scattering the beam transfers its energy to the sample and (partly or fully) it gets excited and emits secondary electrons, X–rays and some longer wavelength photons. Secondary electrons are produced when an incident electron excites an electron in the sample and loses most of its energy in the process [75]. The collected beam intensity at the secondary electron detector from the different pixels are different that gives a unique image known as the secondary electron image. This image gives information about surface morphology of the sample.

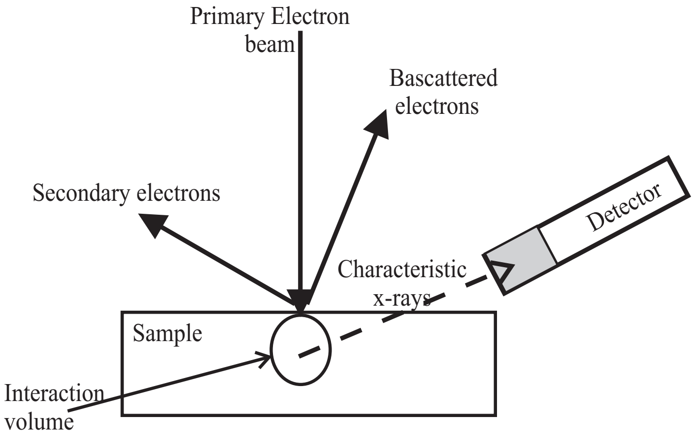

FIGURE 2.10: Schematic representation of interaction of electron with sample

2.2.2.2 Energy dispersive X-ray spectroscopy (EDX)

In addition to secondary electrons, X-rays photons are also emitted during inelastic scattering. During electron bombardment, the atoms of the elements present in the

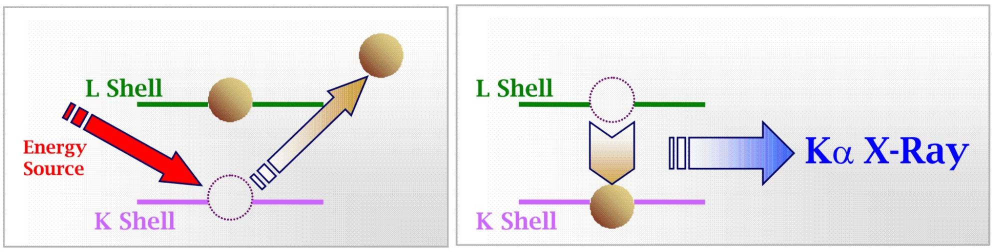

Figure 2.11: Schematic representation of interaction of the process involved in X-ray emission in EDX

sample absorb the incident electron energy and get excited to higher level. When these electrons return to ground level, they emit the X–rays which are characteristic of element (electronic shells) [73, 76]. Figure 2.11 shows the schematic representation of how the incident electron beam creates a vacancy in K-shell. This vacancy is filled by an L-shell electron resulting in the emission of K_α X-rays. Likewise, if an M-shell electron fills the K-shell vacancy (not shown in the figure) then K_β X-rays are emitted. The EDX spectrum is a plot of intensity of X-ray versus energy of the emitted X-ray. An EDX spectrum normally displays peaks corresponding to the energy levels for which the most X-rays had been received. Each of these peaks is unique to an atom, and therefore corresponds to a single element. The higher the intensity of peak in a spectrum, the more concentrated the element is in the sample. An EDX spectrum plot not only identifies the element corresponding to each of its peaks, but the type of X-ray, for example K_α, K_β, L_α, L_β etc., to which it corresponds as well [77, 73].

2.2.3 Photoluminescence (PL)

Photoluminescence is the phenomena in which electronic states of solids are excited by light of particular energy and the excitation energy is released as light. The wavelength of emitted light generally is equal to or longer than that of the exciting light (Stoke's law). This difference in wavelength is caused by a transformation of the exciting light,

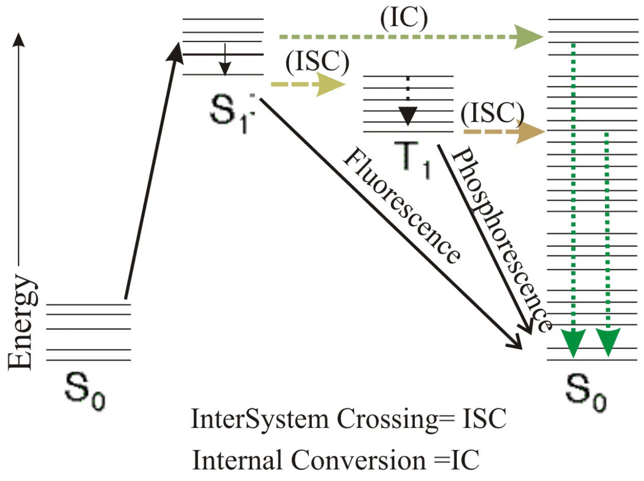

Figure 2.12: Partial energy diagram for a photoluminescence system (Jablonski diagram)

to non-radiative vibration energy of atoms or ions[78, 79]. In photoluminescence spectroscopy, photons with energy greater than the band gap of the material studied are directed onto its surface, the incident photon beam is partially reflected, absorbed, and transmitted by the material being probed. The absorbed photons create electron-hole pairs in the semiconductor. The electrons are excited to the conduction band, or to the energy states within the gap. These electrons can lose part of their energy and transfer from the conduction band to energy levels within the gap. Photons produced as a result of the various recombination of electrons and holes are emitted from the sample surface and it is the resulting photon emission spectra.

There are a number of routes by which an excited electron loses energy. These processes are shown in Figure 2.12 which is widely known as Jablonski diagram. If the photon emission occurs between levels having same spin states for example, $S_1 \rightarrow S_0$this is called fluorescence. If the spin state of the initial and final energy levels are different for example, $T_1 \rightarrow S_0$, the emission is termed as phosphorescence. The phosphorescence is statistically much less likely than fluorescence. The lifetime of phosphorescence is much longer than fluorescence. It can vary from 10^{-3} to 100 sec while in fluorescence the life time lies typically less than 10^{-8} sec [80]. Apart from these two radiative transitions, three nonradiative deactivation processes are also significant as shown in Figure 2.12. These are internal conversion (IC), intersystem crossing (ISC) and vibrational relaxation. Internal conversion is the nonradiative transition between energy states of the same spin state. Intersystem crossing is a nonradiative transition between different spin states. Vibrational relaxation, the most common of the three-for most molecules, occurs very quickly ($< 10^{-12}$ seconds) and is enhanced by physical contact of an excited molecule with other particles with which energy can be transferred through collisions.

In the present work, PL study was done to investigate temperature dependent phosphorescence behaviour of the films to use them as thermographic phosphor. This study was chosen because phosphorescence phenomena are thermally driven which makes the emission sensitive to temperature and allows the thermographic phosphor thermometry technique to work [81, 4, 82]. In order to have a better understanding, the principle of thermographic phosphor is discussed in the following section.

2.2.3.1 Principle of thermographic phosphor

A simplified luminescent system is depicted in Figure 2.13, which shows the energy levels of a dopant in a host. An incident light pulse excites some portion of the dopant population from the ground state (level 0) to an excited state (level 1), after which ions in the excited state decay probabilitically back to the ground state either by reemitting the absorbed energy as a photon or by dissipating that energy as heat.

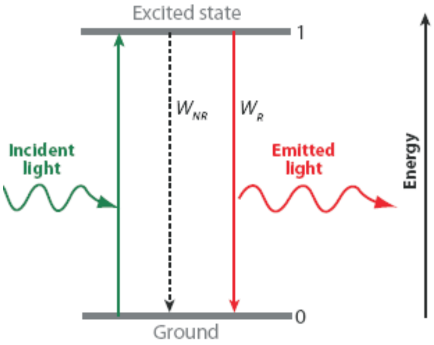

FIGURE 2.13: Schematic diagram showing a simplified, two-level system. Deextation occurs by competing radiative and non-radiative process[4]

These processes have different probabilities of occurring (considering a single excited ion), or different rates (considering the whole population of excited ions), and are competitive with each other. The emission (and absorption) spectrum of this simple system is a single peak corresponding to the energy difference between levels 1 and 0. The lifetime, τ , of the emission is determined by the rates, W, of all decay processes, both radiative and non-radiative.

The measured emission intensity I is proportional to the rate of change excited luminescence centre N_1

$$I \propto \frac{dN_1}{dt} = -\left(W_{Radiative} + W_{Non-radiative}\right) \cdot N_1 \tag{2.6}$$

where $W_{Radiative}$ and $W_{Non-Radiative}$ are the transtion rates of radiative and non-radiative mechanisms, respectively, N_1 is the number of excited luminescence centers, and the negative sign indicates emission. The transition are usually treated as a single term, known as the overall lifetime,τ, such that [83]

$$\frac{1}{\tau} = W_{Radiative} + W_{Non-radiative} \tag{2.7}$$

In general, this lifetime is temperature dependent. When the excitation source is removed, the number of excited atoms/ ions N_1 is gouverned by the differential equation

$$\tau\left(T\right)\frac{dN_1}{dt}+N_1=0 \tag{2.8}$$

where $\tau\left[T\left(t\right)\right]$is the electron lifetime, which is a function of temperature that can change in time. Assuming the electron lifetime is constant during the decay, the solution to equation 2.8 is given as

$$N_1\left(t\right)=N_1^0\exp\left(-\frac{t}{\tau}\right) \tag{2.9}$$

where N_1^0 is the number of electrons at $t=0$, which is when the excitation source is switched off. By differentiating equation 2.9 and recalling equation 2.6, the intensity can be expressed in terms of decay time as

$$I\left(t\right)=I_0\exp\left(-\frac{t}{\tau}\right) \tag{2.10}$$

Where I_0 is the initial emission intensity when the excitation source is removed, at time $t=0$. The monoexponential 2.10 is used to describe the decay phosphor of the intensity in non contact- thermometry. If the temperature is constant, then the decay time τ, which is a function of temperature, also remains constant. The emission intensity of a phosphor at a given temperature is recorded, and the decay time is extracted from the emission data by using fitting procedures. Normally; the decay characteristics are not mono-exponential and need multi-exponential terms for fitting [84, 85, 86]. However, practically a mono-exponential approach should be employed in order to extract a quantity (in the present case; it is the “lifetime”) that is an unambiguous measure for temperature. As such, an algorithm for an unambiguous reduction of multi-exponential decaying phosphorescence signal was used for extracting the lifetime at different temperatures. This algorithm is known as Brübach’s algorithm[83].

2.2.3.2 Decay analysis (Brübach’s algorithm)

The temporal variation of intensity of the phosphorescence signal were normally approximated using Levenberg- Marquardt algorithm [87, 88]. This algorithm is based on mono-exponential decay expression of the form :

$$I\left(t\right) = I_0 \exp\left(-\frac{t}{\tau}\right) + I_{offset} \tag{2.11}$$

where I_{offset} is the offest intensity can be eliminated by substracting the mean value of the respective intensity prior to the laser pulse. The fitting based on this equation 2.11is not sufficient to get an accurate, precise and reliable fitting of the multi-exponential signal. To avoid this inaccuracy, Brübach’s algorithm was employed according to which the temporal variation of phosphorescence signal was divided into several fitting windows. The size of the fitting window is related to lifetime. The fitting window starts at

$$t_1 = t_0 + c_1 \tau \tag{2.12}$$

and ends at

$$t_2 = t_0 + c_1\tau \tag{2.13}$$

where t_0 (laser trigger point) and c_1 and c_2 are the fitting constants. These constants are chosen with regard to balance of a high precision and high accuracy, since these optimal settings generally vary for different phosphors materials [83]. The lifetime in equations 2.12 and 2.13 is unknown and can be obtained by successive iteration [89][83].

2.2.4 Resistivity measurement by four-point probe

Electrical resistivity is one of the most important parameters in electrical characterization of semiconductors. Four point-probe technique is normally used for the determination of electrical resistivity [90]. In this technique, the probe tips are generally arranged along a straight line with equal spacing as shown in Figure 2.14. A current (I) is forced between the two outer probes and the potential (V) between the two inner probes is measured. Typical values for the tip spacing range (s) from 0.5 to 1.5 mm. Four point-probe technique is generally preferred to two point probe as the later leads to an error resistance measurement due to additional wire resistance. Four probe measurements eliminate the effect of wire and contact resistance in the measurement. In four probe method ideally no current will pass through the voltage probe, as the internal resistance of the voltmeter is very high. Therefore, the measured voltage is effectively due the portion of sample during the measurements, which allow us to measure the accurate resistance of the sample eliminating wire resistance.

The sample's resistance to the flow of electrical current causes a potential drop as the current flows along the sample. The resistance of the sample between inner probes is the ratio of the voltage drop to the value of the output current of the power supply. If the samples measured can be considered semi-infinite (i.e the thickness (d), width and length of the sample are each greater than the tap spacing) then the resistivity can be expressed as [91]

$$\rho = 2\pi s \left(\frac{V}{I} \right) \tag{2.14}$$

where ρ is resistivity. Nevertheless, the four-point probe method is commonly used to measure samples which are not semi-infinite and in that case a correction factor (F) is added to equation 2.14 to correct for the sample geometry [92, 93]. The resistivity in such cas can be expressed as

$$\rho = 2\pi s F \left(\frac{V}{I} \right) \tag{2.15}$$

Most applications of four-point probe method for testing materials represent a special case where the thickness (d) of the film is much less than the tap spacing (s). In this case, the equation 2.15 can be reduced to

$$\rho = \frac{\pi}{Ln2} d \left(\frac{V}{I} \right) \approx 4.53d \left(\frac{V}{I} \right) \tag{2.16}$$

Where F =4.53d is correction factor which depends on the shape of the sample and positioning of the probe tips[94].

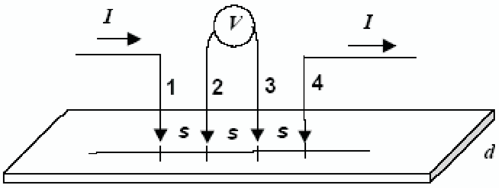

Figure 2.14: Four point probe measurments

2.2.5 UV-Visible spectrophometer

The optical characterisations of the films were done using UV-Visible spectrophometer. It measures the intensity (I) of the light passing through a sample, and compares it to the intensity (I_0) of the light before it passes through the sample. The ratio $\frac{I}{I_0}$ is called the transmittance, and is usually expressed as the percentage (%).

2.2.6 Thickness measurements

The thickness of the film has an influence on the properties of the film such as phosphorescence, transparency, and resistivity. The thickness of the film was determined from the mass change of the substrate (before and after coating procedure) using a high precision weight balance (Sartorius, model CP225D). The thickness of the film can be determined by using the formula [95]

$$d_f = \frac{\Delta m.\rho_s}{m_s.\rho_f}.d_s \tag{2.17}$$

Where ρ, d_s, and m_s are the density and the thickness and the mass of uncoated substrate respectively. ρ_f the density of the film deposited. In table 2.1 the values for calculation of film thickness [96] are given

TABLE 2.1: Numerical values for calculating thicknesses

	Silicon	brosilicate glass	ZnO	TiO_2
Density g/cm^3	2.33	2.23	5.6	4.23
Thickness (μm)	525	150		

2.2.7 Zinc oxide (ZnO)

Zinc oxide crystallizes in three forms: hexagonal wurtzite, cubic zincblende, and the rarely observed cubic rocksalt. The structural properties of ZnO are listed in Table 2.2

Table 2.2: Zinc oxide information [6]

Phase	Crystal structure	Lattice parameters	Zn-O	Density
		A^0	A^0	g/cm^3
ZnO (I)	Wurtzite	$a = 3.246$,$c = 5.207$		5.67
ZnO(II)	Zincblende	$a = 4.60$		
ZnO(III)	Rocksalt	$a = 4.271$		

The wurtzite structure is most stable at ambient conditions and thus most common. The zincblende form can be stabilized by growing ZnO on substrates with cubic lattice structure. The rocksalt (NaCl-type) structure is only observed at relatively high pressures about 10 GPa [6]

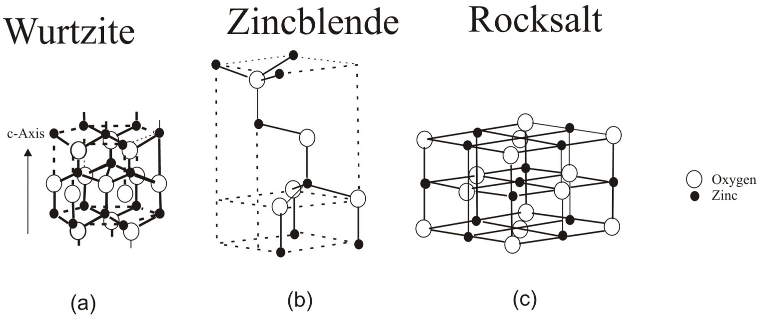

Figure 2.15: Stick and ball representation of ZnO crystal structures. .

ZnO films occur in wide variety of structures [97, 98, 99] .These structures depends largely on the growth conditions and also on deposition techniques. ZnO films are extensively used in a wide variety of applications. A list of application is shown in table 2.3

Table 2.3: Properties and application of ZnO

ZnO Properties	Applications	References
Electrical	Solar cells	[100, 101, 102]
	Piezoelctric devices	[6]
	Sensor	[103, 104, 105]
	Metal oxide varistors	[106, 107]
Electronic	Transparent thin-film transistors	[108]
Optoelectronic	Transparent conducting oxide	[109]

2.2.8 Titanium dioxide (TiO_2)

Titanium dioxide is one of the most investigated functional metal oxides due to their interesting chemical, electrical, optical and physical properties [34]. TiO_2 occurs in three well know phases, rutile, anatase, and brookite. Each phase possesses different crystal lattice structures and therefore different physical properties. The structural properties of TiO_2 are listed in Table 2.4. Rutile is thermodynamically the most stable form. Generally, anatase and brookite rearrange at elevated temperature of 915°C and 750°C respectively, monotropically to rutile. This phase is stable all the way up to its melting point approximately 1830°C to 1850°C. The rearrangement from anatase to rutile is exotherm by 12.6kJ/mol [110].

$$Brookite \longrightarrow^{750^{\circ}C} Anatase \rightarrow^{915^{\circ}C} Rutile \longrightarrow^{1850^{\circ}C} Solution$$

Table 2.4: Titanium oxide information [7]

Phase	Lattice	lattice parameters	Ti-O bond length	Density
		A^0	A^0	g/cm^3
Rutile	Tetragonal	$a= b = 4.584$, c=2.952	1.988	4.27
Anatase	Tetragonal	$a= b = 3.782$, c=9.502	1.91	3.9
Brookite	Rhomohedrical	$a= 5.436, b = 9.166$, c=5.135	$1.84 - 2.03$	4.13

Brookite occurs rarely compared to the anatase and rutile form of titanium dioxide [34]. For that reason, brookite has been excluded from the further description. Rutile and anatase crystallizes in the tetragonal system. Their unit cells are shown in Figure 2.16.

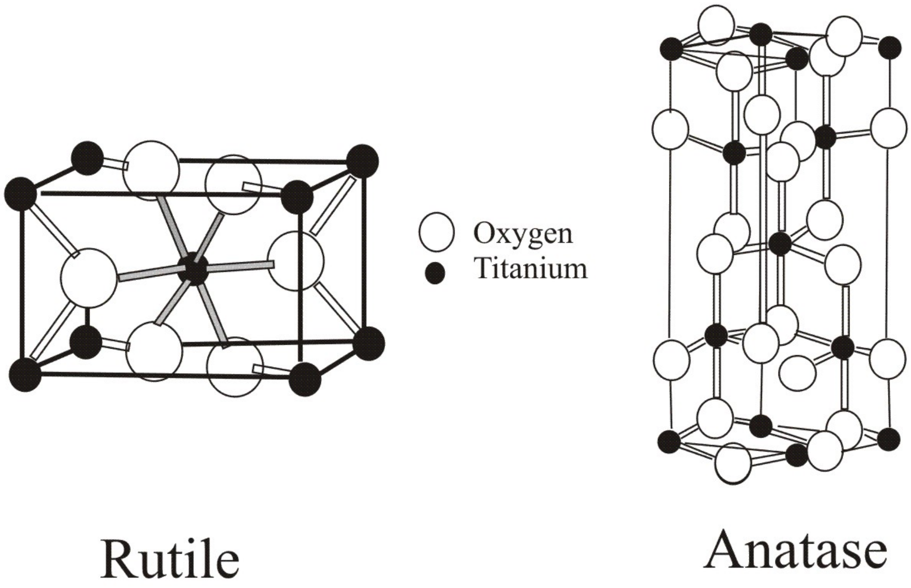

Figure 2.16: Bulk stucture of rutile and anatase

In both structures, the basic building block consists of a titanium atom surrounded by six oxygen atoms in a more or less distorted octahedral configuration. The covalency in the bonds between Ti and O atoms is presumably higher in the rutile phase than in the anatase phase. In TiO_2 films, rutile and anatase phase depends largely on the growth conditions and deposition techniques [34]. They can be used in a wide range of applications. Each phase has a set of properties which make them suitable for specific applications. A list of application is shown in table 2.5

Table 2.5: Properties and application of TiO_2

TiO_2 properties	Phase	Application	References
Optical	Rutile/Anatase	Reflective/antireflective coating Interference coating	[111] [36]
Electrical	Anatase	Solar cells Gas sensor	[37, 38] [39, 40]
Chemical	Anatase	Photocatalyst	[41, 42]
Mechanical	Rutile	In paints	[112]

2.3 Summary

The theoretical background of the various thin films deposition technique and characterisations tools relevant to this thesis was given, this chapter also a literatures review on the structure and application of functional metal oxide films investigate in this work (ZnO and TiO_2) was presented. Further details of the experiments involved in thin films deposition and its characterisation are discussed in the next chapter.

3 Experimental

In this chapter, general descriptions of the experimental setups for the development of functional doped metal oxide films and their characterization are presented. The first section describes various deposition methods that were used in the present work. These include halogen lamp reactor, hot-wall reactor, cathodic vacuum arc reactor and sol gel. The following section describes the characterization tools for the structural, chemical, electrical, optical, adhesion and thermal analysis. As the film properties depend largely on the experimental procedures and parameters involved in film deposition, it is found suitable to describe them in details in the subsequent chapters where the experimental results are discussed.

3.1 Deposition methods

3.1.1 Halogen lamp reactor (HLR)

At the beginning it should be noted that the halogen lamp (HLR) reactor was home built, used for the first time for the deposition of beta iron disilicide (ß-$FeSi_2$) films disilicide (ß-$FeSi_2$) films [113]. Here, the set-up (see Figure3.1) was used to explore the possibilities to deposit un-doped and aluminium doped zinc oxide films and to investigate, by varying some of the parameters, the limitations in terms of deposition and films qualities. So far no previous work was done on the deposition of doped ZnO films using such a set-up.

The CVD setup mainly consists of four units: the gas delivery unit (I), the precursor delivery unit (II), the deposition reactor unit (III) and the pumping unit (IV), as shown in Figure 3.1. The gas delivery unit consists of two gas cylinders of nitrogen gas (N_2) and oxygen gas (O_2), which were used as carrier gas and reactive gas, respectively. Five mass flow controllers (MKS instruments) were used to control the gas flows. The precursor delivery unit consists of a temperature-controlled oil bath to hold the temperature of sublimation constant and two fluidized bed evaporators filled with solid precursors, one filled with $Zn(acac)_2$ and the other with $Al(acac)_3$ (see the picture 3.2). This part was connected with feed pipes to the gas delivery unit. The pipes are stainless steel tubes with an inner diameter of 4 mm.

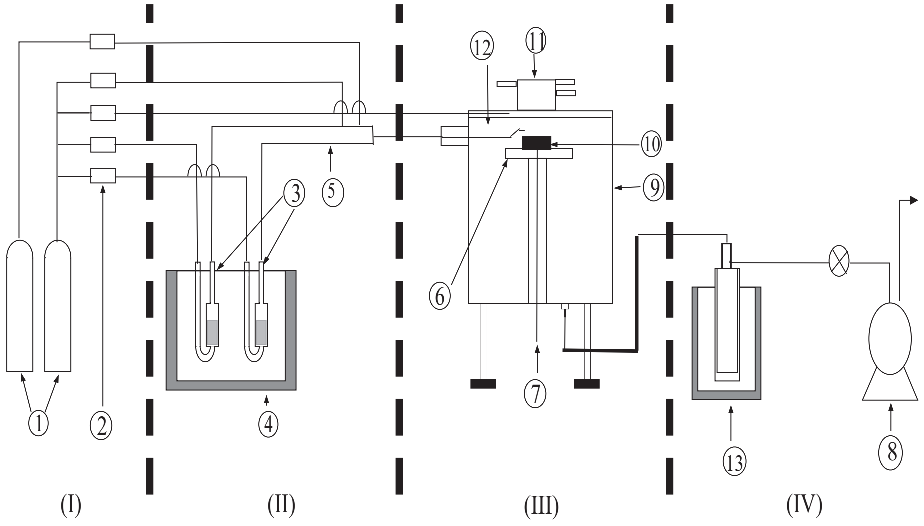

Figure 3.1: Schematic diagram of the CVD – halogen lamp reactor (HLR): (1) gas cylinders, (2) mass flow controllers, (3) fluidized bed evaporators, (4) thermo bath, (5) gas pipes, (6) substrate holder, (7) thermocouple, (8) vacuum pump, (9) reaction chamber, (10) substrate, (11) halogen lamp heater, (12) nozzle.(13) Liquid nitrogen (LN_2) Trap

The deposition reactor system, which is the main part of the set-up, is shown in more detail in Figure3.3. It is composed of a stainless steel cylindrical chamber of 200 mm height with two nozzles. The deposition nozzle has a 4 mm diameter hole and is positioned at an angle of $\sim$30° from the horizontal surface of the substrate holder. It's function is to introduce the reactants. The second nozzle is used to protect the window. A flow of inert gas (N_2) is introduced through this nozzle in order to avoid the deposition on the window during the deposition process. The temperature of the substrate was monitored and controlled by using a K-type thermocouple inserted in the substrate holder and attached to the backside of the substrate. The substrate was heated with 10 halogen lamps and maintained at the desired temperature using a controller. The reactor was optimized for two substrate to heater distance: 50 mm and 60 mm. The maximum substrate temperature atteined was 700 °C at 60 nm and 830 °C at 50 nm [113]. A single halogen lamp is shown schematically in Figure 3.4. It is the type of double ended linear sources (R7S), 118mm in length, 500 watt rated power, ultraviolet free, 9500 Lumen, 230Volt and radiation output $\sim$20% [113]. Finally, the sockets of the lamps are cooled by a flow of N_2.

Figure 3.2: Fotos of (a) fluidized bed evaporator and (b) thermo (oil) bath

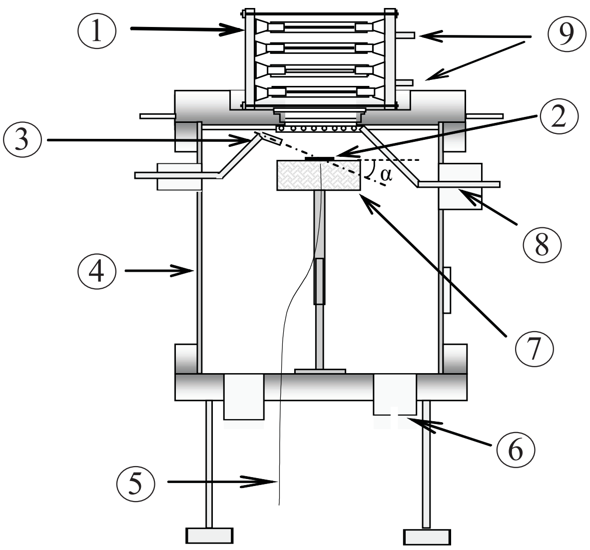

Figure 3.3: A schematic of deposition reactor system. (1) lamps, (2) substrate, (3)deposition nozzle, (4) CVD chamber, (5) themocouple, (6) exhaust, (7) substrate holder, (8) window protection nozzle, (9) N_2 flow entrance for cooling the lamps.

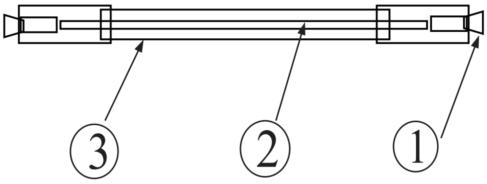

Figure 3.4: Schematic diagram of single halogen Lamp (1) isolated conductor, (2) Lamp filament,(3) vacuum glass

As mentioned above, the fourth part of the set-up is the pumping system, which consists of a vacuum pump (Pfeiffer Vacuum, model DBP 050-4/PK T 11808). The pressure of the reactor was measured with a baratron capacitance manometer. Furthermore, the total pressure in the reactor was controlled by a dosing valve in the exhaust line between reactor and pump. Finally, the pump was protected from contamination by a liquid nitrogen trap

3.1.2 Hot wall reactor (HWR)

Al doped ZnO and un-doped ZnO films were deposited by metalorganic chemical vapour deposition (MOCVD) in a horizontal hot wall reactor (HWR). Figure 3.5 shows a schematic of the HWR set-up, which is divided into three units: the gas delivery unit (I), the precursor delivery unit (II) and the deposition reactor system (III). The gas delivery unit consists of one gas cylinder of synthetic air. The precursor delivery unit consists of a temperature-controlled oil bath to hold the temperature of sublimation and two fluidized bed evaporators filled with the solid precursors; one filled with $Zn(acac)_2$ and the other with $Al(acac)_3$, as described in the HLR set-up. The deposition reactor system consists of a 1 m long ceramic tube with an inner diameter of 28 mm, which is surrounded by the heated tube furnace (Heraeus type RE 1.1, 230V, 14.2A, 3.3kW). The gas flow enters the reactor through a nozzle, which is a tube with an inner diameter of 10 mm. The other end of the reactor is connected to an exhaust gas line. The three units of the HWR set-up are connected by stainless steel tubes with an inner diameter 4 mm.

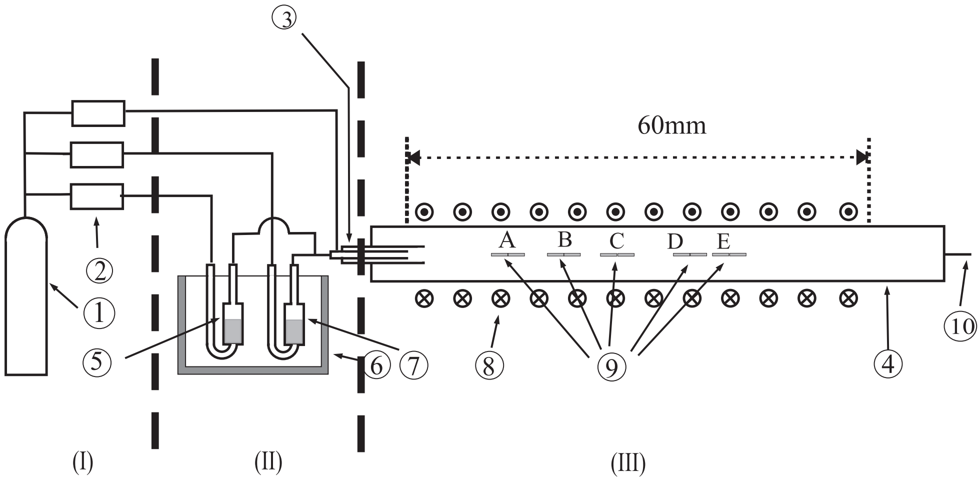

Figure 3.5: A schematic diagram of CVD – hot wall reactor (HWR): (1) gas cylinder (synthetic air), (2) mass flow controllers, (3) nozzle, (4) ceramic tube, (5) $Zn(acac)_2$, (6) fluidized bed evaporators, (7) $Al(acac)_3$, (8) heating coils, (9) substrate, (10) exhaust gas line.

3.1.3 Cathodic vacuum arc deposition (CVA)

The depositions of titanium films is done using the cathodic vacuum arc (CVA) technique. The experimental set-up (shown in figure 3.6) is located in the physics department, thin film technology group, University of Duisburg-Essen.

A basic cathodic vacuum arc system, as shown in Figure 3.6, consists of a vacuum chamber (95 by 115 cm), a conductive cathode (know as source) from which the plasma is derived, an anode, and an arc igniter to initiate the discharge by briefly touching the cathode. The choice of a cathode material is limited only by its ability to conduct a current. In this experiment a titanium cathode was used.

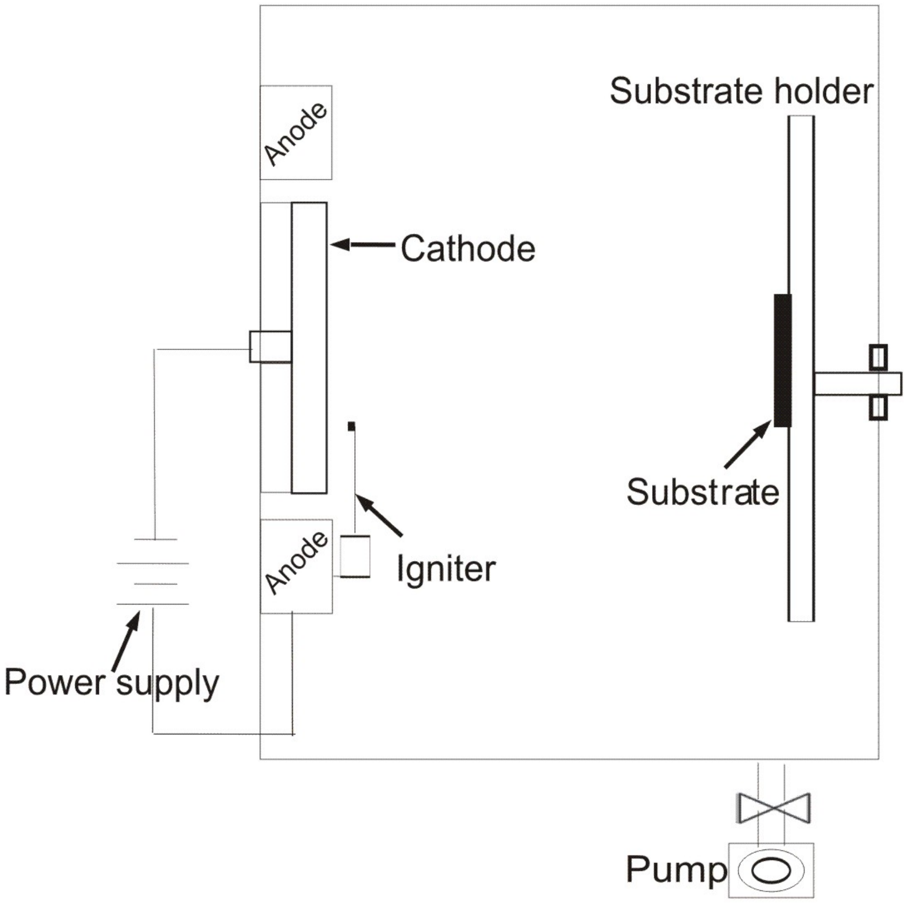

Figure 3.6: Schematic showing the essential components of a cathodic vacuum arc (CVA)

3.1.4 Sol gel

Sol gel technique was used for the deposition of un-doped and europium-doped TiO_2 films. The experimental set-up for this technique was built in house. The sol gel set-up consists of a magnetic stirrer with a hot plate used for mixing the sol. A schematic diagram for the sol preparation is shown in Figure 3.7a. The temperature of the plate was monitored by a contact thermometer with a resolution of 1°C and is controlled by a temperature controller. The prepared sol was used for dip coating. Basic tools like beaker, tweezers, etc. were used for dipping. Figure 3.7b shows the schematic representation of dip coating.

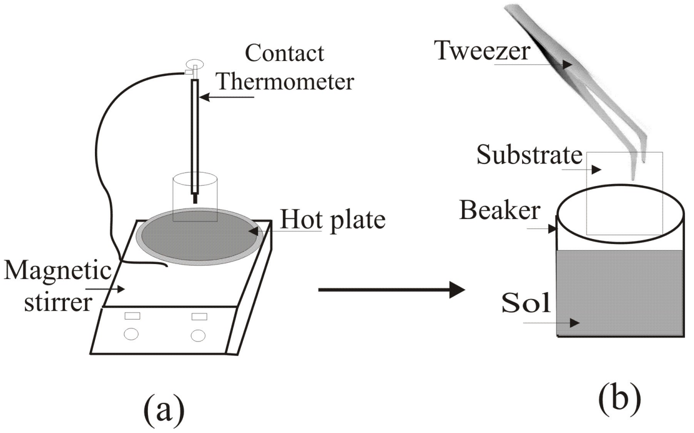

Figure 3.7: Schematic representation of (a) sol preparation and (b) dip coating.

3.2 Characterisation tools

Film properties play a major role in designing the functional behaviour of metal oxide films. Thus, it is necessary to investigate the films quality. The following characterisation tools are used for analysing various parameters of the deposited films:

3.2.1 Structural and chemical analysis

3.2.1.1 X-ray diffraction (XRD)

The structural and phase analyses of the films were done using Brucker model D8 Advance X-ray the diffractmeter working with Cu radiation (λ= 1.5406 °A, (CuKα) XRD measurements were done in two geometries: grazing incidence and Bragg scan. In the present work. The working conditions were typically: 2θ scanning between 20° and 80°, with 0.07° steps. The current and voltage settings were 40 mA and 40 kV respectively. In case of grazing incidence the angle incidence angle of X-ray was set at θ= 2° in order to be sensitive to the sample. In Bragg scan geometry, both the X-ray source and detector moves to give information deeper into films. The obtained X-ray patterns were compared with joint committee on powder diffraction standards (JCPDS) file.

3.2.1.2 Scanning electron microscope equipped with EDX system

The surface morphology of the films was examined with a scanning electron microscope (SEM), ESEM, Quanta 400. This machine a continuous magnification range of 7.10^6 and can achieve a resolution of 2 nm at 30 kV in high vacuum and 3.5 nm at 3 kV in low vacuum. The applied acceleration in the experiments was 20 kV. The chemical compositions of the films were determined using energy dispersive X-ray (EDX) detector fitted with SEM. This detector consists of the silicon with an S-UTW^2 window so that elements with an atomic number greater than 5 (Boron) can be detected. The energy of the radiation of elements with a smaller atomic number is so low that it is absorbed by the window in front of the detector and detection is therefore not possible [114, 115]. The active area of the detection was 10 mm^2. However, measurements of pure ZnO powder samples showed that the measured signal is erroneous for carbon and thus a quantitative statement about the proportion of carbon was not possible.

3.2.2 Electrical analysis

3.2.2.1 Four point probe set-up

Electrical analysis of the un-doped and Al doped ZnO films were done by measuring the resistivity of the samples. Linear four point probe (Microworld, France) with a probe spacing of 1 mm was used for the resistivity measurement. Figure 3.8 shows the experimental set-up for the measurement of the electrical resistivity of thin films. KEITHLEY 220 programmable current source was employed for sourcing current within a range of 10-300 µA and with a sourcing accuracy of 0.05 %. The potential drop across the two inner probes was measured using KEITHLEY 195A digital multimeter with a measurement accuracy of 0.01 %. All the resistivity measurements have been carried out at room temperature

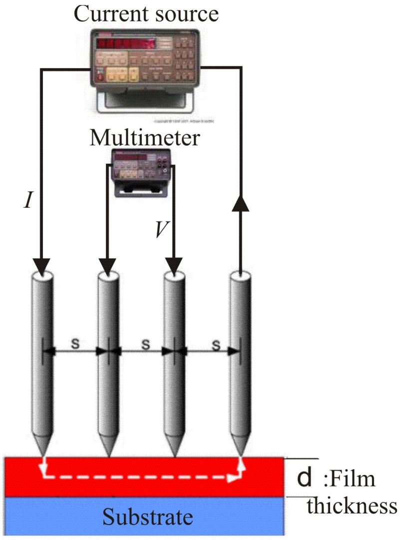

Figure 3.8: Schematic representation of the experimental set-up for the measurement of electrical resistivity

3.2.3 Optical Analysis

3.2.3.1 Phosphorescence set-up

The general set-up for the phosphorescence measurements can be divided into two parts, one for the spectral analysis and one for the time –resolved phosphorescence analysis.

Spectral analysis

The set-up for spectral analysis is shown in Figure 3.9.

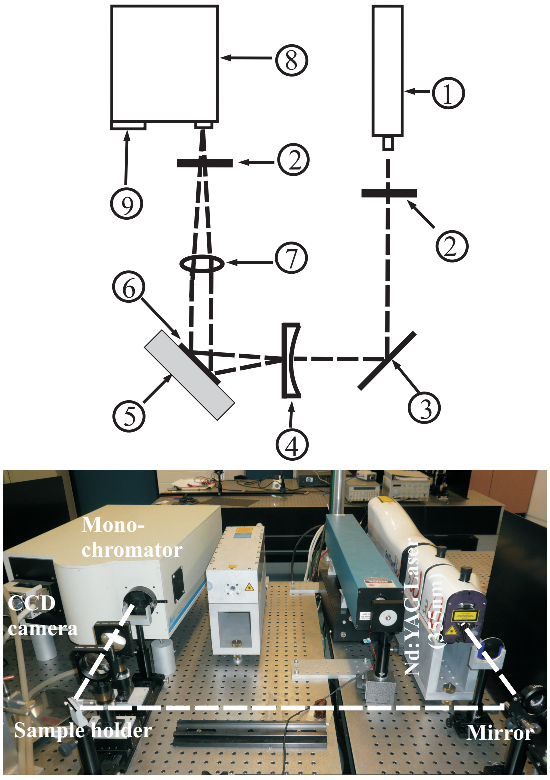

Figure 3.9: Schematic diagram of the spectral analysis setup. (1) Nd:YAG Laser (355 nm), (2) shortpass filters, (3) mirrors, (4) planconcave lens, (5) sample holder, (6) sample, (7) biconvex lens, (8) monochromator, (9) CCD camera

A monochromatic light source is used for the excitation of the fluorescence; in this case the third harmonic of a Nd: YAG laser (Quantel, Model Brilliant) with a pulse duration of 5 ns and a repetition frequency of 10 Hz, emitting at wavelength of 355 nm. A short-pass filter is used to remove the remainder of the 2nd harmonic radiation, before the laser beam is widened by a plan concave lense in order to illuminate a large portion of the sample. The resulting phosphorescence is focussed by a biconvex lens and passed through a long- pass filter with a cut off wavelength of 355 nm in order to block the laser beam. The filtered signal was collected by a spectrometer (Horiba Jobin, Model Triax 500) equipped with a CCD camera (Hamamatsu Photonics, Model C5967-03).

Time–resolved phosphorescence analysis

The set-up for the time-resolved phosphorescence analysis is shown in Figure 3.10.

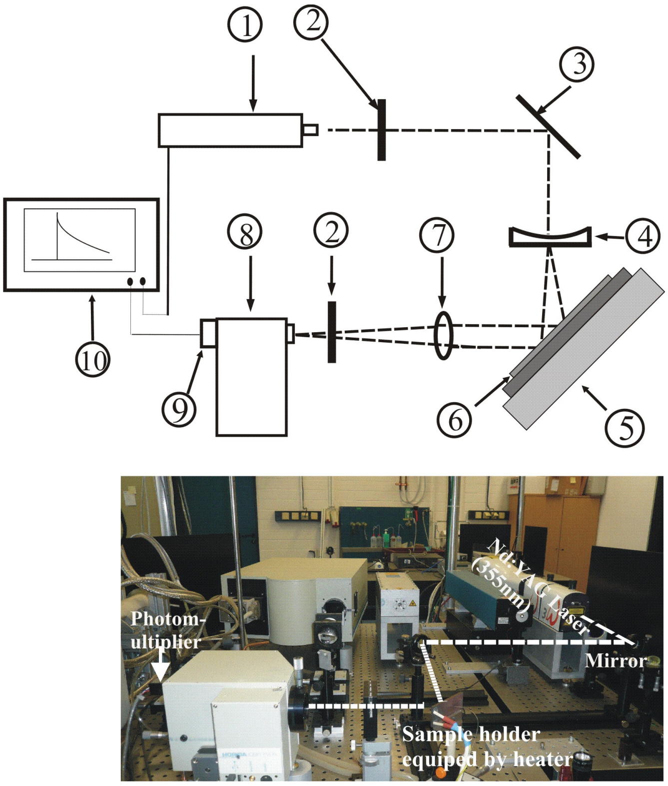

Figure 3.10: Schematic diagram of the time-resolved phosphorescence analysis setup. (1) Nd:YAG Laser (355nm), (2) shortpass filters, (3) mirrors, (4) planconcave lens, (5) sample holder with heater, (6) sample, (7) biconvex lens, (8) monochromator, (9) photomultiplier (PM), (10) oscilloscope

It is essentially the same as the set-up for the spectral analysis, except that the CCD camera is replaced by a photomultiplier (PM) and the sample holder is equipped with a heater in order to control the sample temperature. The light emitted from the sample was focussed onto the PM through a low resolution spectrometer (30 nm resolution) in order to resolve just a single phosphorescence transition for time resolved. The time-resolved PM-signal was detected by a high speed-oscilloscope (Tektronix, model: TDS 5104).

3.2.3.2 UV-Visible spectrophotometer

A UV-VIS scanning spectrophotometer model Shimadzu UV-2102 was used to measure the optical characteristics of un-doped and Al-doped ZnO films deposited by MOCVD on glasses substrate. This spectrophometer possess a double beam configuration. A schematic of this configuration is shown in Figure 3.11. In a double beam configuration, the monochromatic light is divided into two beams using mirrors such as a rotating mirror and a semi-transparent mirror so as to make two beams, the sample beam and the reference beam. The sample beam passes through the sample while the reference beam passes through the reference sample (which is uncoated glass for the present case). Both the transmitted signal from the sample and the reference are detected simultaneously. The transmission measurements for the samples were done at room temperature with a scan range between 300-800 nm (visible range).

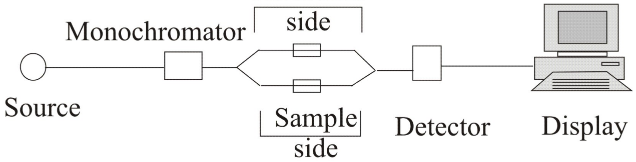

Figure 3.11: Schematic diagram of the UV-Vis 2102Pc spectrophotometer

3.2.4 Film adhesion analysis

3.2.4.1 Cavitation erosion set-up

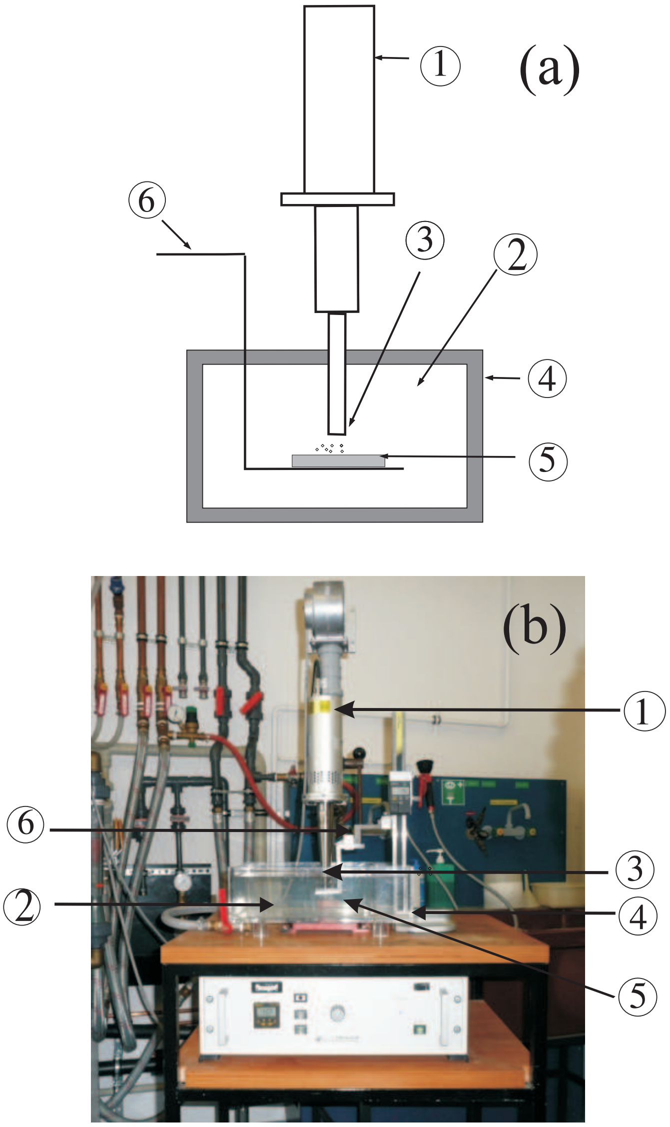

Figure 3.12: (a) Schematic representation of the cavitation erosion set-up. (1) ultrasound generator 20 kHz and 25 µm, (2) de-ionized water, (3) sonotrode, (4) tank, (5) sample, (6) sample holder. (b) Photo of the cavitation erosion experiment.

Testing the adhesion of thin films is an important and difficult tasks of surface engineering. Several methods are used, such as the scratch test, bending test, impact test, Rockwell imprint test, and cavitation test. The cavitation test, as it was used in this work, has been used to test the adhesion of thin films [116, 117]. In order to test the adhesion of the thin films, cavitation tests were carried out. The set-up for the cavitation test ASTM G32-92 [American society for testing and materials:ASTM G32-98] [118] is shown in Figure 3.12 and consists of water tank in which the sample surface is exposed to high- power ultrasound, an ultrasound generator, and a sonotrode. The lower end of the sonotrode consists of a titanium tip with 10 mm diameter and is arranged about 0.2 mm above the sample.

3.2.5 Thermal analysis

A commercial TGA/DTA (Bähr STA 503) was used to perform the thermogravimetric experiments for thermal stability measurements of $Zn(acac)_2$. The atmosphere was nitrogen or helium and air. The flow rate of 100 cm^3/min (for nitrogen) was controlled by a calibrated mass flow controller. Open alumina crucibles were used in all experiments; the inner diameter being 5.35 mm, the inner height is 7.2 mm. The temperature sensor was calibrated by measuring the melting points of reference substances (4-nitrotoluene, naphthalene, indium and potassium perchlorate) which cover the whole temperature range for the measurements. For thermal stability measurements the experiments were performed using non isothermal temperature programme in which the temperature was raised linearly with a heating rate of 2 K/ minute up to 500°C, and the mass loss of the substance with time and temperature was observed along with the DTA signal. This temperature programme provides the information regarding the sublimation temperature (defining the lower limit for its CVD application), melting point.

3.3 Summary

The experimental set-ups used for the deposition of un-doped and Al-doped ZnO films and titanium dioxide (TiO_2) films have been outlined in this chapter. Also the instrumentation involved in the investigation of various properties of the resulting films are presented. However, the experimental procedures and parameters involved in film deposition and their characterisation are described in the subsequent chapters in order to relate them with the experimental results. In the next chapter, the two CVD set-up halogen lamp reactor and hot wall reactor (see Figure 3.1 and 3.5) were employed for depositing un-doped and Al- doped ZnO film. The experimental results and detailed explanation of these results are also presented accordingly.

4 Deposition of un-doped and aluminium doped ZnO film

4.1 Introduction

Zinc oxide (ZnO) is a transparent low-cost and non-toxic material with various interesting properties. Due to the similarity of its optical and electronic properties to those of gallium nitride it is discussed as a possible alternative to GaN-based applications, including the use in blue or UV-LED devices. In contrast to the preparation of GaN, the precursors for the preparation of ZnO are easy to handle and less toxic. Doping the ZnO with group III elements such as gallium [119], boron [120] and aluminium [121] results in an improved electrical conductivity without degrading the optical transmission in the visible spectral range. Therefore, M-doped ZnO (M=Ga, B, Al) is discussed as a transparent conducting oxide (TCO) with potential applications as e.g. front electrodes in solar cells devices [122, 123], or electrical gas sensors [124]. Due to its potentially cheaper production, ZnO:M (M=Al, Ga, B) are possible alternative materials for indium-tin-oxide (ITO) which is usually used in such devices. MOCVD has been used in the present study for film deposition.

It is obvious that for the development of a low-cost deposition process, the choice of the precursor is most important. For the MOCVD growth of zinc oxide, different precursors have been reported in the literature: often diethyl zinc (DEZ) [125, 126] and dimethyl zinc (DMZ) [127] are used, resulting in the growth of highly pure *ZnO* films. Less attention has been paid to the growth of *ZnO*-films from zinc acetate [128] and zinc acetylacetonate (Zn(acac)$_2$) [129, 130, 131] because it is reported that these precursors tend to produce carbon contaminations. It is suspected that these contaminations influence the electric and optical properties of the grown films negatively. However, zinc acetate and Zn(acac)$_2$ have the advantage of being commercially available and cheap. Further, they are chemically stable in atmospheric air, non-toxic and easy to handle. This favors their use in an industrial coating process. Because of these reasons, we have studied the growth of zinc oxide films from zinc acetylacetonate in more detail. Aluminium acetylacetonate (Al(acac)$_3$) was used as an aluminium source for the preparation of Al-doped *ZnO* films. Un-doped *ZnO* and Al-doped *ZnO* films were deposited on silicon and borosilicate glass substrates by metal organic chemical vapour deposition (MOCVD) technique using two different reactors: (halogen lamp reactor (HLR) and hot wall reactor (HWR)). In HLR, the deposition process is activated by the radiation of halogen lamps while in HWR, it is activated by electric heating. It should be mentioned that to the best of our knowledge, no previous work has been done on the deposition of doped zinc oxide from acetylacetonates of zinc and aluminium using HLR and hence it was chosen for investigation. The HWR was used in order to compare with films deposited using HLR. The HWR is capable of depositing more than one samples simultaneously and also the production cost is less.

The goal of this chapter is to investigate the deposition of un-doped and Al-doped *ZnO* film on silicon and borosilicate glass substrates using the above mentioned reactotrs and also to identify factors leading to get films with desired properties, such as, crystalline structure, low resistivity, high transparency, etc., without ignoring the production cost and the reproducibility of the films. This chapter has been splitted into two sections. First section deals with film properties deposited using halogen lamp reactor while the second section discusses that using hot wall reactor.

4.2 Halogen lamp reactor deposition

4.2.1 Experimental procedure

The experimental set-up used for film deposition is shown in Figure 3.1. For further details (see chapter 3 section 1.1). The set-up basically consists of a vacuum chamber which can be evacuated to 1 mbar minimal pressure. The substrates were either pieces of silicon wafers (Si(100)-orientation) or borosilicate glasses, both sized 2cm x 2cm. Before each deposition they were carefully cleaned in ethanol by using ultrasonic bath for 10 minutes and subsequently weighed before and after deposition with a high precision balance. From the change in mass the thickness of the films were calculated, the latter by using the density of bulk Zinc oxide 5,6 g/cm^3 [132]. Finally, the substrate was loaded into the reactor chamber. The feed pipes and nozzle were heated to 148 °C by resistive wire heaters wrapped around the tube at 148°C in order to avoid the condensation. During deposition of the un-doped zinc oxide films, a fluidized bed evaporator filled with zinc acetylacetonate (Zn(acac)$_2$) has been used as a precursor delivery system and connected to the reactor. The substrate is placed near the nozzle orifice. As a result, the chemical reactions are localized near the substrate. Thus, a small amount of precursor is sufficient to get the desired film thickness. After filling the fluidized bed evaporator with precursor the deposition reactor system was evacuated to 200 mbar by a vacuum pump. Within the chamber, the substrate was mounted on a thermally well isolated holder. Through an optical window in the top of the chamber, they were heated by the thermal radiation of an array of 10 tungsten halogen lamps, activating the chemical reaction of the precursors as shown in Figure3.3. These lamps with a variable electrical power up to a maximum of 5 kW are controlled electronically until a steady temperature of the substrate (in the following called the "deposition temperature") is reached. The temperature is measured with a K-type thermocouple which is mounted at the backside of the substrate; well defined substrate. Substrate temperatures were limited within 600°C to avoid the glass substrates from damage. The fluidized bed evaporator has been placed in an oil thermo bath to control its temperature at 110°C. The vapor was transported to the chamber with a flow Φ_{Zn,N_2} of 500 standard cubic centimeter (sccm) nitrogen as carrier gas, entering through a cylindrical nozzle of 4 mm diameter. Before reaching the orifice, 100 sccm oxygen was added for supporting the oxidation. Additional 200 sccm $N_2(\Phi_{N_2})$ was added in order to increase the gas velocity. Finally, the gas mixture at the orifice consists of nitrogen, $\mathrm{Zn(acac)_2}$, and oxygen in excess. This gas mixture was then blown onto the substrate under an angle of $\alpha = 30°$ relative to the surface, as shown in Figure 3.1. The distance between the orifice and the substrate was approximately 70 mm. At the end of the deposition process, the precursor supply has been first stopped, than the substrate was cooled down slowly to room temperature. Finally, the pressure in the reaction chamber was increased to atmospheric pressure. For the deposition of the Al-doped ZnO films, $\mathrm{Al(acac)_3}$ was evaporated by using the same fluidized bed evaporator for controlling both precursors and transported to the chamber with a carrier gas flow of nitrogenΦ_{Al,N_2} which was varying for different Al-concentrations between 0 and 80 sccm. Before reaching the orifice, it was added to the above mentioned $\mathrm{Zn(acac)_2}$-vapor/N_2/O_2-mixture while the additional nitrogen flow Φ_{N_2} was decreased by the amount of Φ_{Al,N_2}. Thus, the total flow of the gas mixture was constant for all experiments. It should be noted that all depositions of un-doped ZnO were carried out at different deposition temperature 400, 450, 500, 550 and 600°C for 90 minutes, while for Al-doped ZnO 550°C was selected as deposition temperature because above

550°C the glass was broken easily. The preparation conditions of the un-doped and Al-doped *ZnO* films are summrized in the table 4.1

Table 4.1: Preparation conditions of undoped and Al-doped *ZnO* thin films by HLR

	Substrate	Substrate temperature (°C)	Pressure (mbar)	Temperature of thermo bath (°C)	Gas supply pipe (N_2, O_2)[sccm]	Carrier gas(N_2)[sccm]
Un-doped ZnO film	Silicon Glass	400-600 450-600	200	110	(200,100)	500
Al: ZnO film	Silicon Glass	500 500	200	110	(200-x,100)	x=(10-100)

4.2.2 Thermal analysis of Zn(acac)$_2$in N$_2$

Both acetylacetonate precursors used are solid powder at room temperature. In order to study their sublimation, DTA/TG measurements were performed under conditions similar to those in the fluidized bed evaporator during the deposition experiments. The evaporation of the Al(acac)$_3$ is discussed elsewhere[56], and the DTA/TG measurements of the Zn(acac)$_2$ are shown in Figure 4.1. Zn(acac)$_2$ was continuously heated in these experiments in a nitrogen gas atmosphere while the TG/DTA signals were recorded Figure 4.1. The heating rate was 1°C / min. The TG experiment for Zn(acac)2 (left ordinate in Figure 4.1) shows a two-step evaporation process with two rapid mass losses at around 63°C-75°C and at 85°C-140°C. Simultaneously, two endothermic peaks appear in the DTA-signal (right ordinate in Figure 4.1), one between 63°C-75°C and another one rather sharp peak at around 124°C. The mass loss between 63°C-75°C is presumably due to the evaporation of chemically combined water which typically evaporates at such low temperatures. At about 85°C, observable evaporation of $Zn(acac)_2$ starts, indicating the lowest possible evaporation temperature of the precursor. Therefore, the evaporation temperatures of the precursor should be more than 85 °C in the deposition experiments. It is also expected that the deposition rate increases with increasing evaporation temperature.

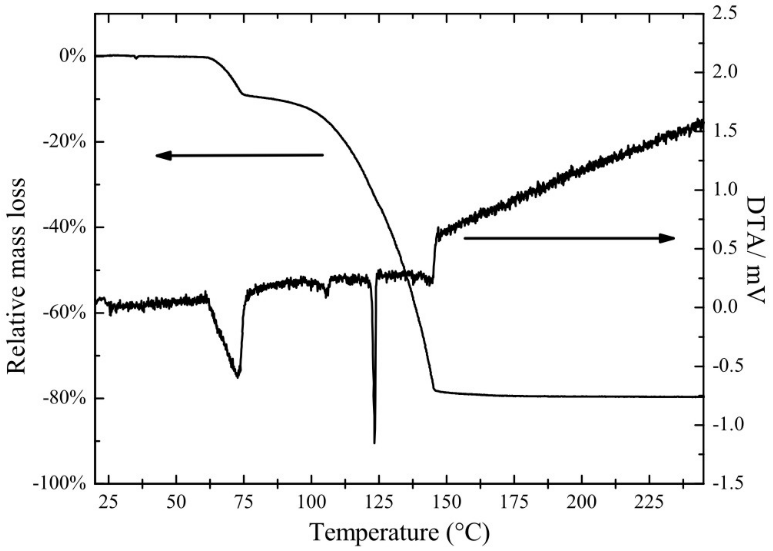

Figure 4.1: TGA/DTA analysis of the zinc acetylacetonate precursor: $Zn(acac)_2$ was heated in nitrogen atmosphere of 1000 mbar at a constant heating rate of 1°C/min.

However, the sharp endothermic peak which is observed in the DTA-signal at 124°C Figure 4.1 indicates the melting of the substance. Therefore, the temperature should not exceed 124°C if a fluidized bed evaporator is used as in the present study, because this type of evaporator needs powder as precursor source. As a consequence, we used 110 °C for the evaporation of the $Zn(acac)_2$ in order to get high deposition rates and to beware of the problem of melting the precursor. The $Al(acac)_3$ was evaporated at the same temperature, because 110 °C is also a useful evaporation temperature for aluminium acetylacetonate in CVD-experiments [56, 133]. Using the same temperatures for both precursors has the advantage to need only one thermobath for controlling both precursor temperatures. This reduces the costs of the experiments.

It can be seen from Figure 4.1 that a residue mass of ∼22 % was left after evaporation. This is because the water in the precursor reacts with $Zn(acac)_2$ to ZnO. T.Arii et al [134]analyse water free $Zn(acac)_2$, by evaporating dry $Zn(aca)_2$ in dry N_2 atmosphere. He observed that $Zn(acac)_2$ evaporates nearly completely and only a residue of 5 % was found after evaporation. He also studied that on adding water vapor to the N_2 transport gas, $Zn(acac)_2$ does not evaporate completely leaving behind a residue of ∼30 % of ZnO after evaporation. This results because $Zn(acac)_2$ partly reacts to ZnO with water vapor [134].

4.2.3 Result and Discussions

4.2.3.1 Temperature dependence of the film growth

As mentioned previously, thin ZnO films were deposited at 200 mbar for 90 min at temperature between 450 and 600°C. The growth rate was calculated from density of bulk ZnO[132]. In general CVD reactions, the growth-rate dependency on substrate temperature follows Arrhenius behaviour and thus usually shows an exponential increase of the growth rate with increasing temperature. In the present case, the Arrhenius plot was drawn by graphing the logarithmic value of the growth rate as function of the inverse of substrate temperature (Figure 4.2).

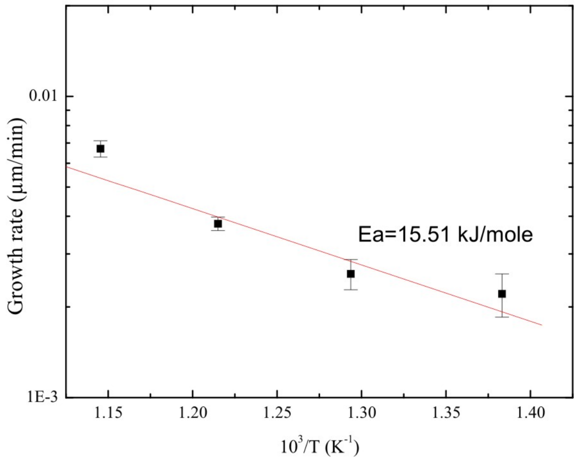

Figure 4.2: Arrhenius diagramm: growth rate of thin zinc oxide on silicon substate grwoth at 200 mbar total pressure.

Each experimental data shown in the Figure 4.2 is an average of two consecutive depositions. It can be seen that the experimental results are close to the linear fit showing an ideal Arrhenius behaviour. However, at a substrate temperature of 600°C, the linear plot lies below the growth rates obtained during successive depositions. In order to have a better representation, the growth rate was plotted as a function of substrate temperature (Figure 4.3). This Figure shows the deviation of the growth rate at 600°C from the ideal exponential behaviour which is theoretically expected. This deviation results may be either due to an abrupt increase in growth rate by a vigorous oxidation reaction on the substrate or due to the transition from surface to the gas phase reaction or both [3]. Kamata et al [131] reported a similar behaviour in the growth rate at higher temperatures. They observed that the growth rate of ZnO films deposited using Zn $(acac)_2$ as precursor. (same as in the present case) remain constant within the temperature range 400-500 °C, then increases rapidly and again becomes constant above 600°C.

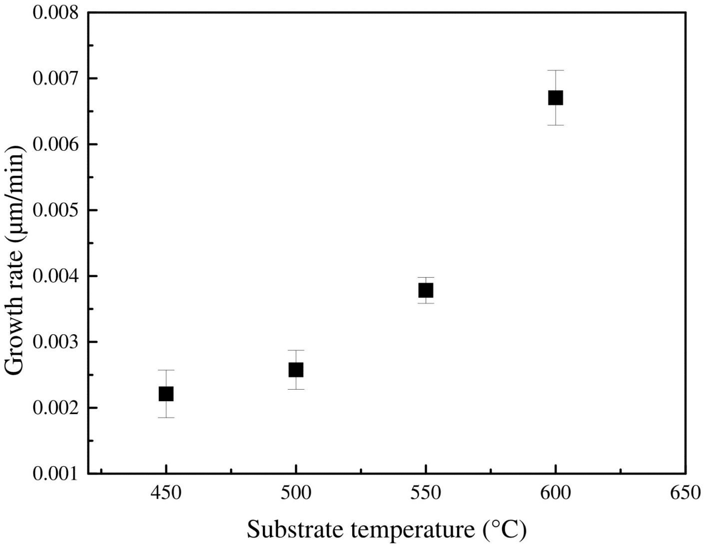

Figure 4.3: Relationship between the growth rate of ZnO films and substrate temperature.

Figure 4.2 is used to determine the activation energy (E_a) which is the minimum energy required to initiate a chemical reaction. In the present case, the value of E_a obtained is 15.51 kJ/ mole. This value is comparable with that obtained by Maruyama et at [135],[136](13-15 kJ/ mole, 20.6 kJ/ mole). The growth rates of ZnO films are less than those reported by kamata et al [131] and Maruyama et al [136]. This is because the sublimation temperature of the precursor was kept lower in the present work (110°C) than that in case of kamata et al [131] (125°C) and Maruyama et al [136](180-200 °C). It has been observed by TGA/DTA analysis (Figure 4.1) that the precursor used for the present work melts at around 125°C. That's why the sublimation temperature has been restricted to 110°C.

4.2.3.2 Film structure

The XRD patterns are shown in Figure 4.4. Thereby these patterns were measured with a constant angle of incidence, 88° relative to the surface normal, while the detector angle was varied, named a θ-2θ scan (detector scan or grazing incidence) see section 5.1. Therefore these measurements are sensitive to the near surface region. Figures 4.4(a and b) show the typical XRD patterns of the undoped ZnO thin films on Si (100) and borosilicate glass substrates grown at different substrate temperatures between 400°C to 600°C (Si (100)-substrate), and between 450°C to 600°C (glass-substrate). Already at deposition temperatures of 400 °C diffraction peaks are observed, indicating that crystalline films are grown. Nevertheless, the diffraction peaks are stronger and sharper for deposition temperature above 450°C due to a better crystallinity, indicating that higher deposition temperatures should be used for high quality films. As presented in Figures 4.4(a and b), two reflexes are observed for the un-doped ZnO-films on both samples, a strong reflex at $2\theta = 34.46°$ for plane (002) and a less strong one at $2\theta = 62.90°$ for plane (103). Both indicate the presence of the hexagonal structure of ZnO and all the diffraction peaks are in complete agreement with those of the JCPDS Card 03-0888. Several of the ZnO-reflections are missing, indicating a preferred orientation of the films on the substrates. Similar diffraction patterns were observed by Khandelwal et al [137] and Prepelita et al [138]irrespective of the deposition technique. Khandelwal et al. [137]deposited ZnO films on Si (100) substrates using pulsed laser deposition while Prepelita et al.[138] deposited ZnO films on glass substrates using radio frequency magnetron sputtering. The presented measurements which were performed under a fixed angle of incidence (θ=2°) are sensitive to the near surface region but not useful for the detailed study of the preferred orientation. Thus, we also performed X-ray diffraction measurement under (θ-2θ) scan, where both the X-ray source and the detector were varied. (often called Bragg condition- more details are presented in chapter 2 section 5.1).

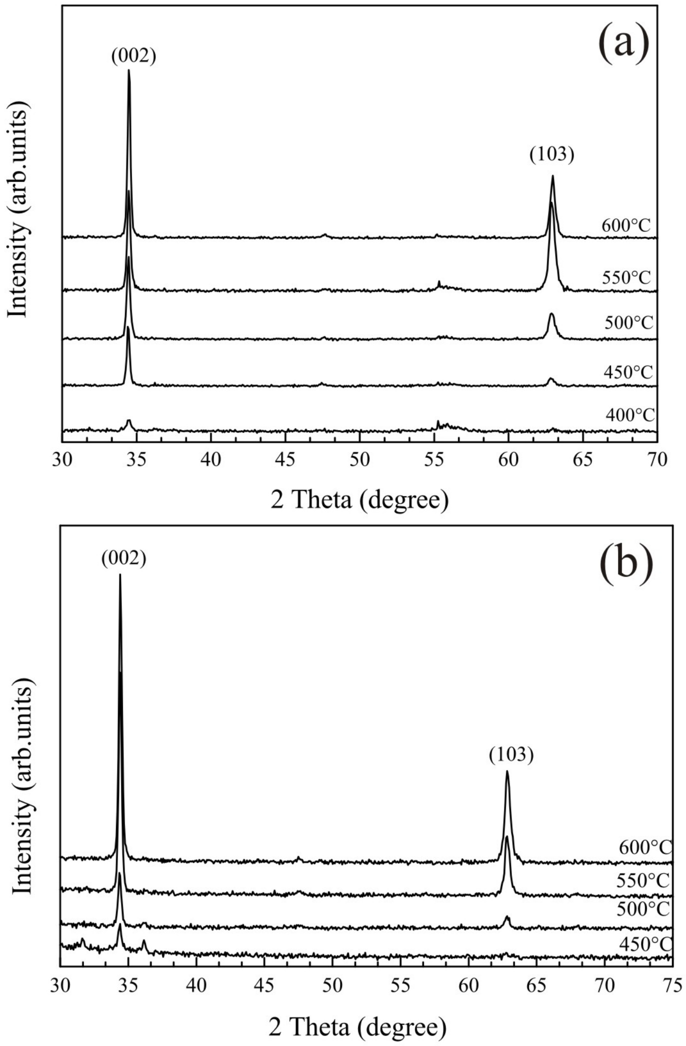

Figure 4.4: XRD patterns of undoped ZnO deposited by (HLR) reactor at different temperature(a) on silicon substrate ,(b) borosilicate glass substrate. The XRD patterns are shifted for better comparison.

Figure 4.5 shows the results XRD diffraction using Bragg condition of undoped ZnO film on both substrates. As indexed in the Figure 4.5, two diffraction peaks are observed a strong intensity peak at $2\theta = 34.46°$ for the (002) plane and a less intensity peak at $2\theta = 72.53°$ for the (004) plane , these results indicate also that the ZnO film have a preferred orientation (c-axis oriented crystallites). The c-axis orientation in ZnO films can be understood by the ' grain boundary movement' model proposed by Lodder et al [139]. According to this model, at the very first stage of film growth, certain grains with particular orientation starts to grow. By thermodynamical coalescence of crystallites during film growth, orientational growth (c-axis orientation for ZnO film) is achieved. In contrast to the un-doped ZnO films, the XRD-patterns of Al-doped ZnO films (Al-concentration: 1.7 %) Figure 4.6 show most of the reflections which are expected for hexagonal ZnO. Obviously, those films have a polycrystalline structure. However, the (002) and (103) reflections still dominate the patterns. Thus, the c-axis (002) orientation of the crystallites is still present, but less distinctive.

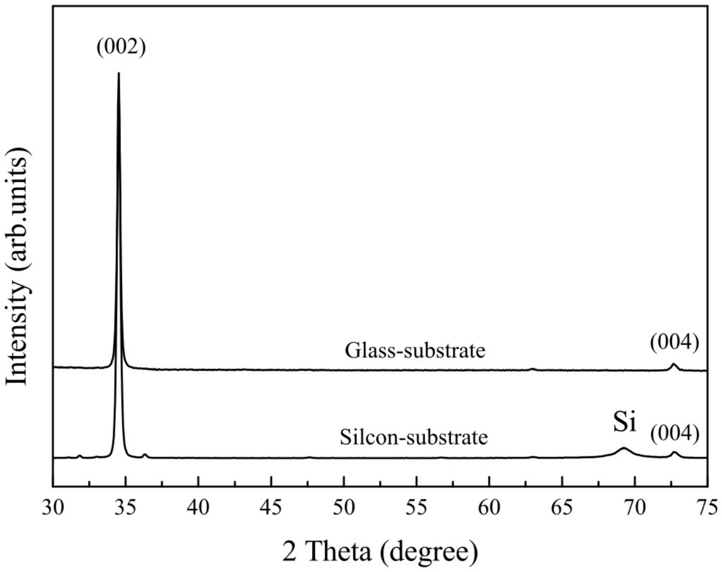

Figure 4.5: XRD patterns of undoped ZnO deposited by (HLR) reactor at 550°C on borosilicate glass substrate. Measured under Bragg condition. The XRD patterns are shifted for better comparison.

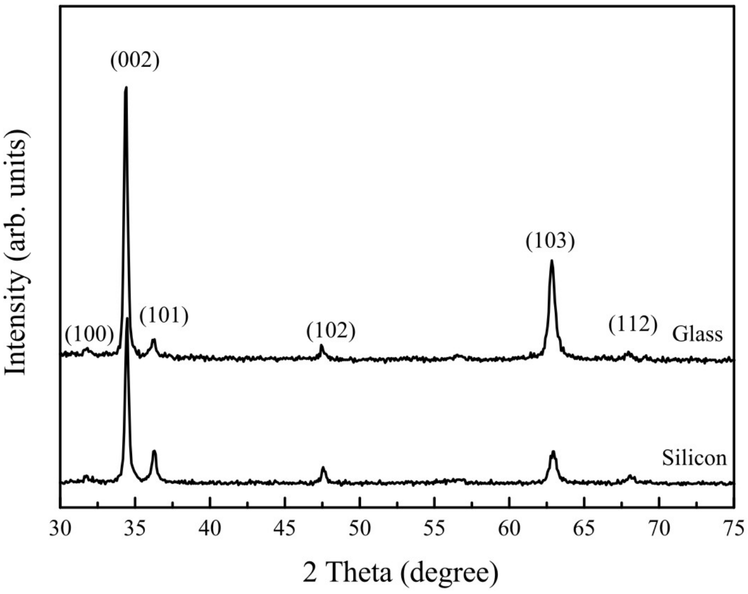

Figure 4.6: XRD patterns of Al-doped ZnO deposited by (HLR) reactor at 550°C on glass and silicon. The XRD patterns are shifted for better comparison..

4.2.3.3 Surface morphology

Next, to obtain additional information about the crystallinity of the film and to confirm that the films have some preferred orientation, the morphology of the films was analysed. The SEM-image of the un-doped film (Figure4.7) supports this observation as most of the observed ZnO-grains show a hexagonal surface in the top view of the sample (Figure 4.7 (d)). The preferred orientation is seen even better in the cross section of the sample Figures 4.7 (4b and 4c).

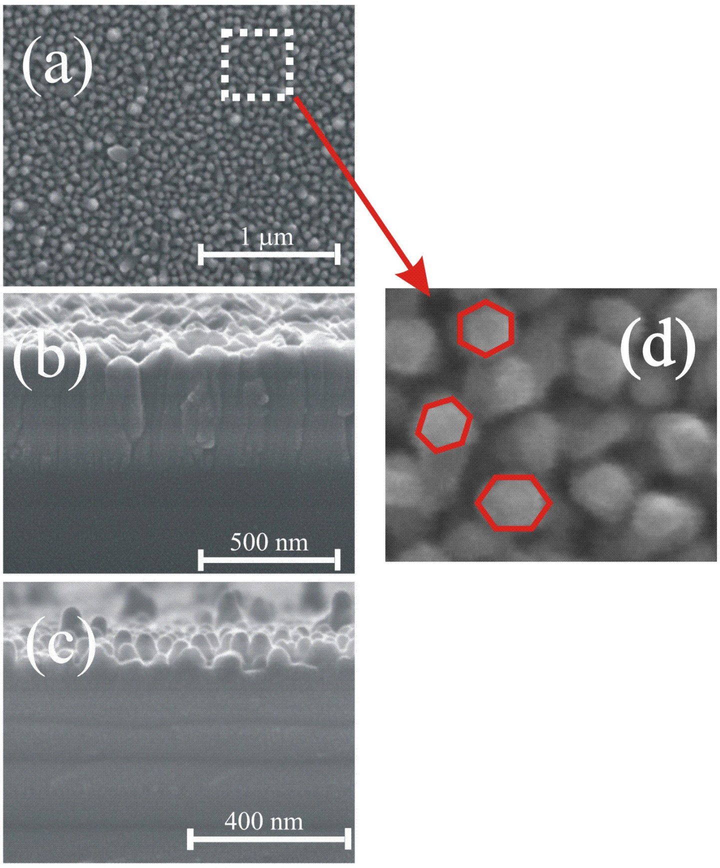

Figure 4.7: SEM images :(a) top view, (b, c) cross section of a 0.5 µm thick ZnO film grown on Si(100) using HLR at 550°C, (d) magnified image of the rectangular section marked in image (a).

4.2.3.4 Chemical composition

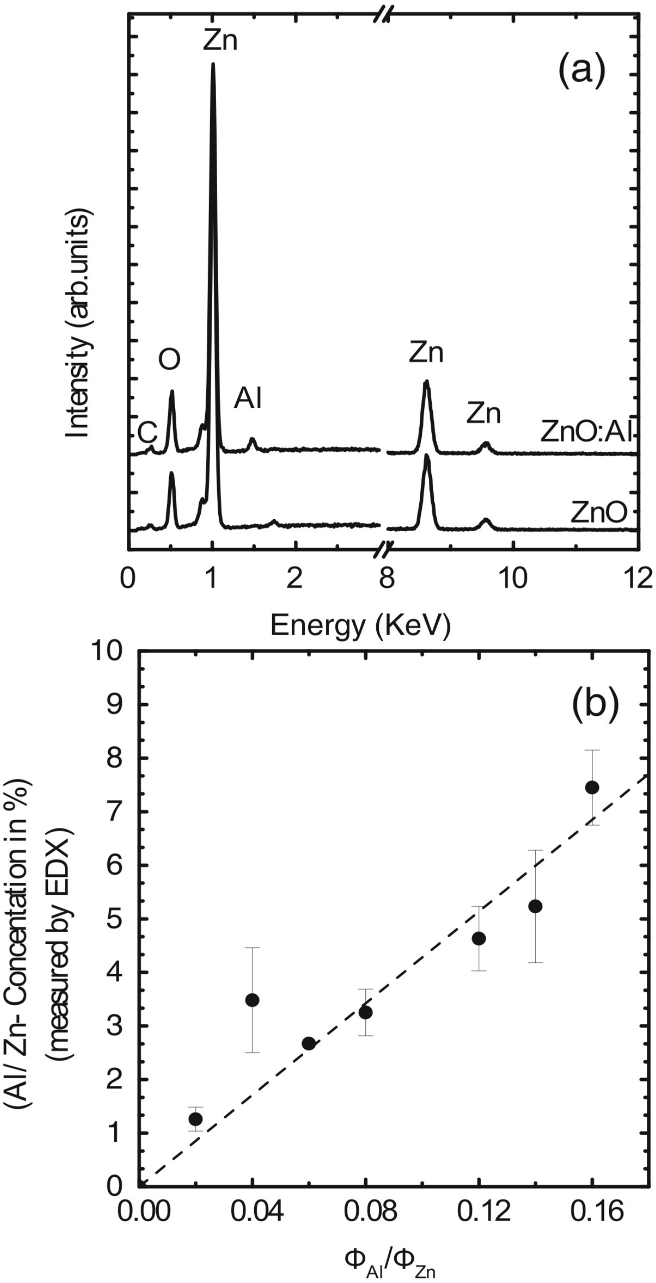

Figure 4.8: EDX-analysis of the grown films: Figure (a) shows the typical EDX spectra of one un-doped and one Al-doped ZnO-film which was prepared by using a flows of Φ_{Al,N_2} = 70 sccm and Φ_{Zn,N_2}= 500 sccm N_2 carrier gas through the acetylacetonate evaporator. Figure (b) shows the Al/Zn-concentration within the films as function of the flow rates Φ_{Al,N_2} and Φ_{Zn,N_2} of the carrier gases through the evaporators. Each data point is the average of three EDX measurements. The error is the standard deviation

The chemical compositions of the films on studied by energy dispersive x-ray fluorescence spectroscopy, EDX Figures 4.8(a and b). The presented measurements were performed on 3 µm thick films which were grown in 6 hours deposition, because only such thick films can reliably be analysed by quantitative EDX. Two EDX-spectra typical for the grown films are given in Figure 4.8a: one of an un-doped ZnO on Si(100) and another one of an Al-doped film. They clearly show the presence of zinc, oxygen, and (the upper spectrum only) aluminium. Also some amount of carbon was detected for both samples. As Si (from the substrate) is not present in the spectra, the sample acts like a semi-infinite half-space, which enables the quantitative analysis of the chemical compositions of the films. For this analysis, the EDX-setup was calibrated with a commercially available ZnO-powder (Sigma Aldrige, purity $>$ 99%): it turned out that EDX always reveals carbon contaminations around 5-10 %, even for the pure ZnO-powder. Obviously, the carbon content can not be analysed quantitatively by EDX and was therefore neglected in the following. For the un-doped ZnO-film (lower spectrum in Figure 4.8a), the software of the calibrated EDX- setup reveals the presence of $\sim$47% Zn, $\sim$53% O, as expected for ZnO within the precision of the measurement. For the Al-doped film (upper spectrum in Figure 4.8a), the EDX-measurements reveal the presence of $\sim$46% Zn, $\sim$52% O, and $\sim$2% Al, clearly confirming the doping of the sample. The Al/Zn concentration within the films was analyzed as a function of the gas flow Φ_{Al,N_2} of nitrogen carrier gas through the aluminium acetylacetonate evaporator, while the nitrogen carrier gas flow through the zinc acetylacetonate evaporator (Φ_{Zn,N_2}) was kept constant at 500 sccm. Figure 7b shows the molar ratio$\frac{n[Al]}{n[Zn]}$ of the Al and Zn-atoms within the films (calculated from the EDX spectra) as a function of the ratio of the gas flows used $(\frac{\Phi_{Al,N_2}}{\Phi_{Zn,N_2}})$. Each data point is the average of three EDX measurements and the error bars are the standard deviation. It is easily seen from Figure 4.8 b, that the aluminium concentration within the films increases linearly with the carrier gas flowΦ_{Al,N_2} through the aluminium acetylacetonate evaporator. However, this result is not surprising as the amount of precursor vapour leaving the evaporator is proportional to the used carrier gas flow as long as the gas mixture within the evaporator is saturated. As the evaporation temperature of the aluminium acetylacetonate is high, 110°C, and the carrier gas flow Φ_{Al,N_2} are rather low ($<$ 80 sccm) it is expected that the mixture is saturated.

The ratio $\frac{n[Al]}{n[Zn]}$ as a function of the ratio of the used carrier gas flows $(\frac{\Phi_{Al,N_2}}{\Phi_{Zn,N_2}})$ was fitted by a line (dasched line in Figure 4.8 b). Al content can be well controlled.

$$\frac{n\left[Al\right]}{n\left[Zn\right]} = 0.42.\frac{\Phi_{Al,N_2}}{\Phi_{Zn,N_2}} \tag{4.1}$$

4.2.3.5 Electrical properties

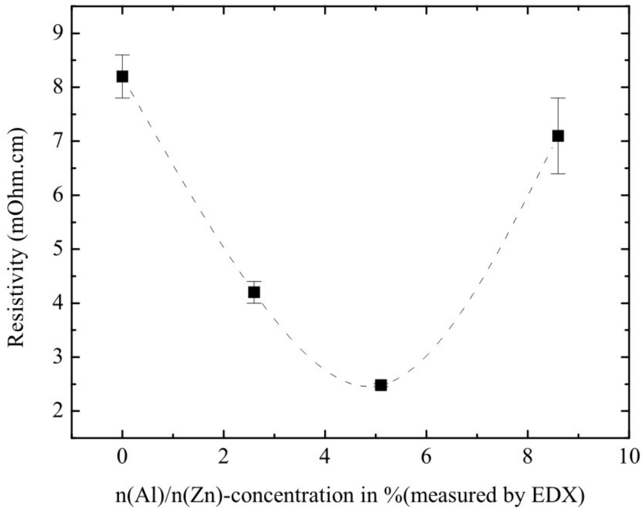

Figure 4.9: Electrical resistivity of the 0.5 µm thick films on the borosilicate glass as a function of the dopant (aluminium) content. The data are the averages of each 5 measurement on two different samples for each Al-concentration. The errors are the standard deviation.

The electric resistivity of several $ZnO : Al$ films of about 0.35 to 0.5 µm thickness were measured as a function of the dopant concentration by the four point method. Figure shows the results for four different aluminium concentrations $\frac{n[Al]}{n[Zn]}$ between 0 and 8.6 %, which were deposited for 90 min at 550°C on borosilicate glasses by varying the carrier gas flows. The resistivity was calculated from the measured arial resistance where the thicknesses was obtained by the weighing the sample with a high precision balance befor and after deposition.

The results are listed in Table 4.2. The presented data are the averages of five measurements each on two different samples, which were prepared for each dopant concentration. All measurements were performed by using a current of 100 mA. The error bars represent the standard deviation. For all Al-concentrations, one observes a relatively low resistivity between 2.4 and 8 $m\Omega\ cm$(Figure 4.9 and Table 4.2), confirming the usefulness of the developed films as transparent conducting oxides (TCOs). It is remarkable that as the Al concentration in ZnO films increased, the electrical resistivity decreases and reaches a Al value of 2.48 $m\Omega\ cm$ for a 5.1 % Al concentration. Qiao et al [140] and Aktaruzzaman et al [141] have reported similar resistivity value for Al-doped ZnO containing 1-2 %. A brief review of the electric properties of such films is given in reference [142]. Their, the lowest values of the resistivity for such films are reported to be in the range of 1400 to 0.2 $m\Omega cm$. The electrical properties of ZnO are primarily dominated by electrons generated from O^{2-} vacancy and Zn interstitial atoms [143]. The decrease in resistivity with Al doping is due to the contribution from Al^{3+} ions on substitutional sites of Zn^{2+} ions and Al interstitial atoms, as well as from oxygen vacancies and Zn interstitial atoms [144]. But such Al atoms in the films do not always contribute as dopant. When the Al content in ZnO films increases above a certain critical concentration, it segregates into the grain boundaries. These segregates Al atoms do not activate as dopant and hence do not contribute in increasing the electron concentration. They rather create defects which, in turn, enhance the resistivity. This is the reason for the observed increase in the resistivity of Al-doped ZnO films beyond an Al concentration of 5.2 %. Minami et al reported that when ZnO film is doped with Al by sputtering method using $ZnO + Al_2O_3$ target, electron concentration increases with increasing amount of Al_2O_3 , and decreases when the amount of Al_2O_3 in the target is over $\sim$ 4 %. Park et al [144]and Oh et al [145] and Tang et al [146] observed a similar behavior of the resistivity versus Al concentration in ZnO film (as is observed in the present case (see figure 4.9).

4.2.3.6 Optical properties

Optical and further electrical properties such as band gap were calculated from the optical transmittance spectra of the films on borosilicate glass substrates. For all samples, the optical transmittance spectra were measured at room temperature between 300 nm and 800 nm with a commercial UV-Vis-spectrometer (see Figure 4.10). It is seen that the transmittance of the films improves with an increase of the aluminium concentration. The oscillations in the spectra are caused by optical interferences on the smooth surface. A sharp absorption edge is also observed in the spectra, this confirms again the crystal quality because in amorphous films no sharp absorption edges are observed [147, 148].

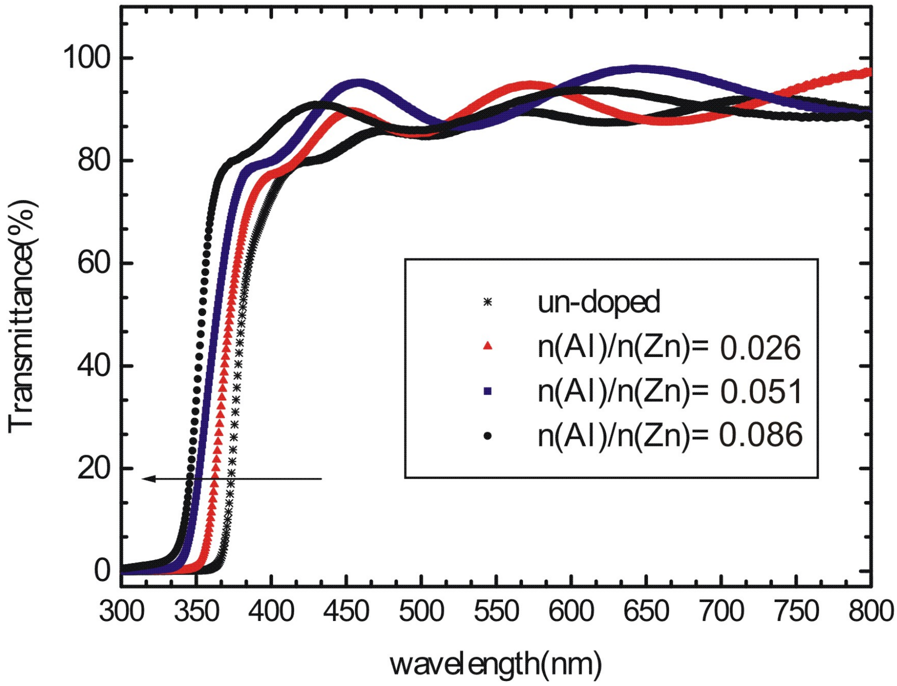

Figure 4.10: Optical transmittance spectra of ~0.5µm thick ZnO:Al films on borosilicate glass for different dopant concentration

In Figure 4.10, it is seen that the coated samples still have a high transmittance in the visible range, which is more than 80 %. As noted above the transmittance spectra within the UV-Vis region ($<$ 550 nm, Figure 4.10) can be used to calculate the band gap of the grown films. It is seen that the band edge of the un-doped ZnO film is around 380 nm. With increasing aluminium content the band gap increases due to the doping which is known as Burstein-Moss shift resulting from an increase of the carrier concentration. Thus, the band edge shifts to lower wavelength [$\sim$355 nm for n(Al)/n(Zn)=0.086], which is in good agreement with the literature.

To further study the optical properties of the films, the optical band gap were calculated by using the Tauc model [149], and the Mott model [150]. The optical absorption coefficient α can be expressed as [151]

$$I = I_0 exp\left(-\alpha d\right) \tag{4.2}$$

where I is the intensity of transmitted light, I_0 is the intensity of incident light, and d is the film thickness. As the transmittance (T) is defined as $\frac{I}{I_0}$, the above equation 4.2 can be used to determine the value of α. In direct transition semiconductor, α and $E_g$are related by [152],

$$\alpha = \left(h\nu - E_g\right)^{1/2} \tag{4.3}$$

where h is Planck's constant, ν is the frequency of the incident photon energy and E_g is the optical band gap. The Figure4.11 is the plot of α^2 versus $h\nu$ for doped ZnO films with different Al concentration. The linear dependence of α^2 to $h\nu$ indicates that Al-doped ZnO films are direct transition type semicondoctor. The photon energy at the point where α^2=0 is $E_g$and is obtained by the extrapolation method. .

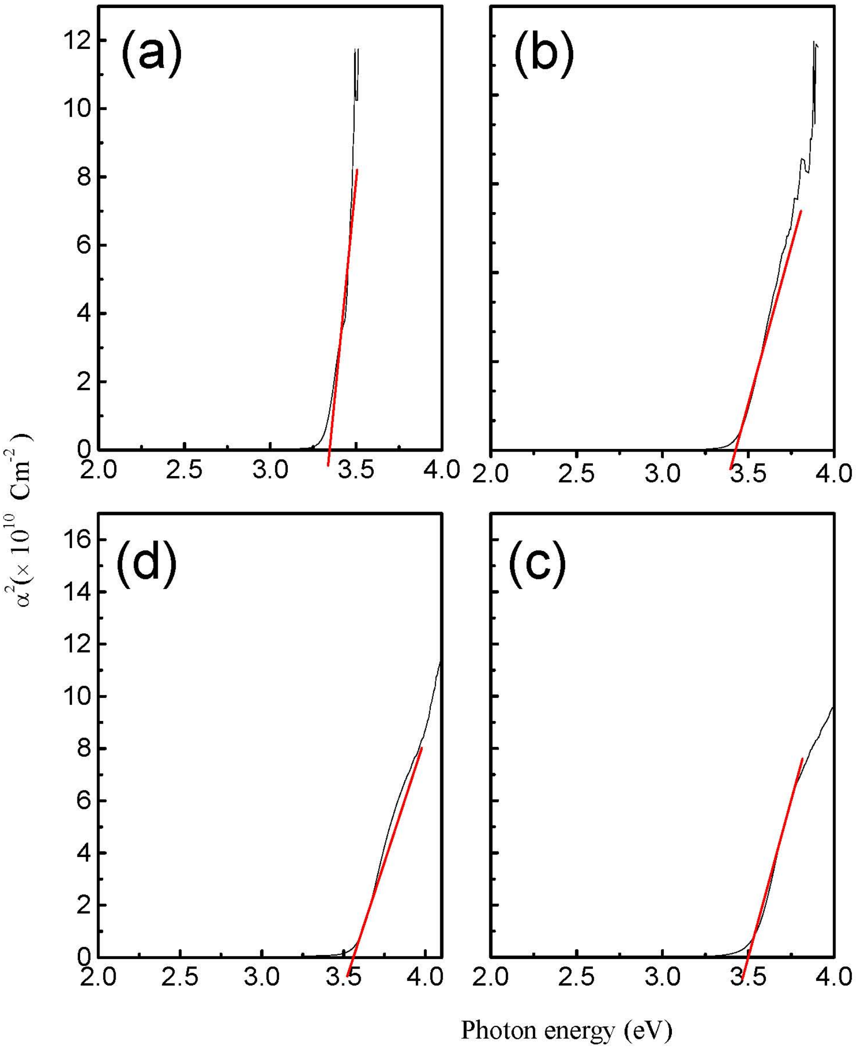

Figure 4.11: plot of α^2(absorption) versus photon energy $h\nu$ for (a) undoped, (b) $\frac{n[Al]}{n[zn]}$=0.026, (c)= $\frac{n[Al]}{n[zn]}$=0.051,(d) $\frac{n[Al]}{n[zn]}$=0.086

The optical band gap values obtained are summarized in table 4.2. It was reported that the optical band gap of zinc oxide thin films devolped using MOCVD lies between 3.25 and 4.06 eV depending on the various parameters, such as deposition temperature, doping, etc [153, 154]. Tang et al [155] and Fragal et al [156] reported the relationship between optical band gap and Al doping concentration of the ZnO thin films. They observed that in un-doped ZnO films, the optical band gap appeared at 3.25 eV while it increased to 3.47eV with Al doping. A similar behaviour was observed in our films, where the E_g value increase from 3.34 eV (for un-doped film) to 3.57 eV (for high Al-doping concentrations) (see 4.2). Figure 4.12) shows the dependence of band gap of Al doped ZnO films of similar thickness (432 nm ± 60 nm) as a function of Al concentration. it can be seen that the band gap with increases linearly with Al content. They were fitted using a linear function, which is

$$E_g\left(eV\right) = 3.34 + 2.6\frac{n\left[Al\right]}{n\left[Zn\right]} \tag{4.4}$$

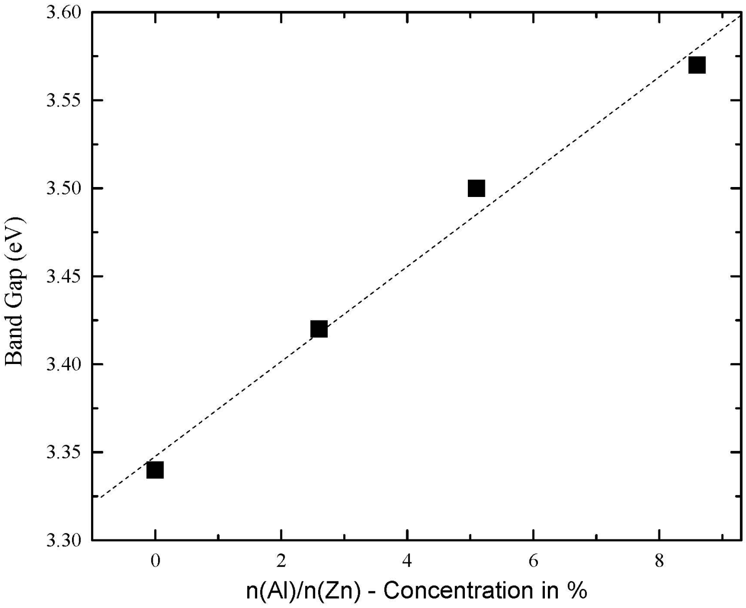

Figure 4.12: Band gap as function of different dopant concentration.

Table 4.2: Electrical and optical properties of the grown films. Legend: n(Al)/n(Zn)=molar ratio of Al- to Zn-atoms within the films, d= thickness, ρ =resistivity, E_g = band gap

Al-Flux (sscm)	0	30	60	90
$\frac{n(Al)}{n(Zn)}$ (%)[1]	0	2.6	5.1	8.6
$\rho\,(m\Omega cm)^2$	8.2 ± 0.4	4.2±0.4	2.48±0.40	7.1±0.7
$Eg(eV)^3$	3.34	3.42	3.50	3.57

[1] Calculated from the carrier gas flows and equation 4.1

[2] Measured by four point method

[3] Calculated from the band edges (Figure 4.11.) by following the procedure of [157]

4.2.3.7 Photoluminescence (PL) Properties

Photoluminescence (PL) is one of the most important properties of ZnO thin film since it represents the optical quality of the materials and it closely correlated with defect densities in the films. In general, PL emission for ZnO could be divided into two categories: near band edge (NBE) excitonic UV emission and defect related deep level emission (DLE) in the visible range. The origin of the (NBE) was reported to be determined by free excitonic recombination, while the origin of the (DLE) was not well understood although it had ascribed to the oxygen vacancies, oxygen interstitials or other impurities [158]. The PL spectra of the deposited films were determined using the set-up show in Figure 3.9. Figure 4.13 shows the PL spectra of un-doped and Al doped ZnO films prepared at 550°C and annealed at 900°C with various aluminium concentrations. As mentioned , the films were exited with 355 nm wavelength from

YAG:Nd laser PL spectra were acquired at room temperature. The emission peaks are observed in the un-doped and Al doped films deposited at 550°C and annealed at 900°C for 2 h. No emission can be observed from the films with out annealing. As ca be seen from Figure 4.13 no spectra are recored between range 525 and 535 nm, due to the use of a filter which blocked the laser signal at 532 and protected the CCD camera, the spectra are composed of two parts (see Figure 4.13), an excitonic related near band edge (NBE) emission peak in the ultraviolet region around 380 nm and a deep level emission band(DLE) around 500 nm. For all spectra, the (NBE) is dominated and the highest intensity of this band was obtained at n(Al)/n(Zn) = 0.051 and the further addition of aluminium concentration lowered the PL intensity. The spectrum for un-doped ZnO film shows only one peak at around 383 nm and for Al doped film we observed peak at 383 nm as well as at around 500 nm. The highest intensity was obtained at n(Al)/n(Zn)= 0.051 and further addition of Al lowered the total PL intensity.

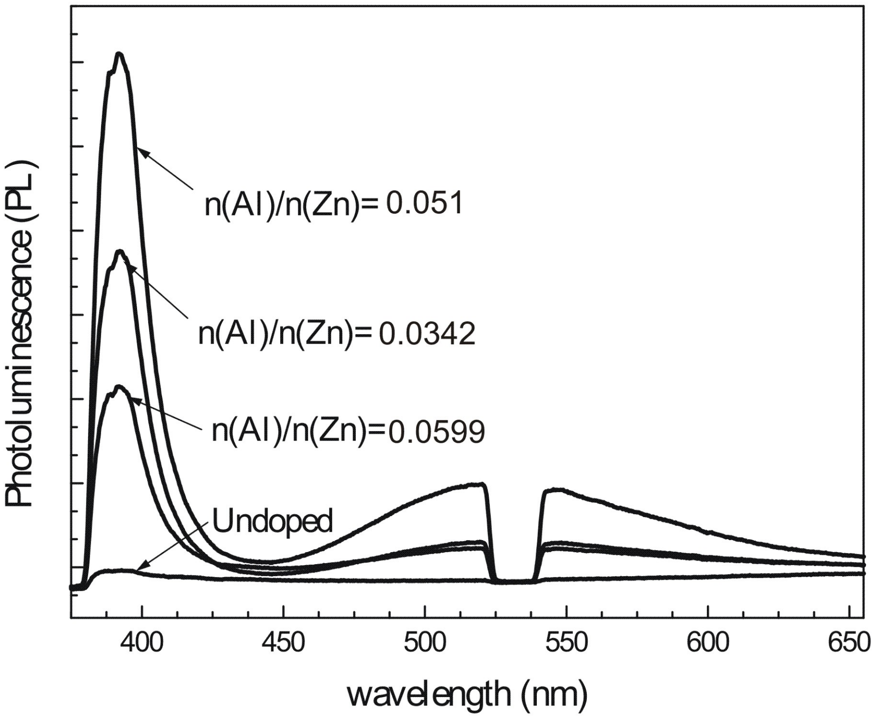

Figure 4.13: Phosphorescence spectra measured at room temperature as a function of different dopant concentration

4.2.3.8 Temperature dependent

In order to investigate Al-doped ZnO films as thermographic phosphor, the PL spectra of the film which has the highest intensity was selected from the Figure 4.13 and was investigated at different temperatures. These temperature-dependent measurements were performed between room temperature and 400°C using the set-up described in the experimental section 3.3. Figure 4.14a, show the PL spectrum for different temperatures up to 400°C, while at higher temperature no signal was observable. The phosphorescence process may be used to measure the temperature by measuring properties such as, phosphorescence decay time, shift in intensity and spectral distribution. The phosphorescence decay time for Al doped ZnO film (n(Al)/n(Zn) = 0.051) is very short around, of picoseconds, for this reason the decay time property can not be used easily for temperature measurements. Furthermore, the shift in PL peaks due to temperature change is not resolved with the present setup. However, with increasing temperature, the PL intensity is quenched. As a result, the area under the spectrum is changing significantly with temperature. This quenching of intensity is due to the thermal ionization of exciton and thermally activated nonradiative recombination mechanisms[159]. This variation in the spectral distribution can be used to evaluate the temperature. This is done by integrating the peaks at different wavelength ranges e.g. Full range (from 375 nm to 672 nm), first emission peak (from 375nm to 440nm), and second emission peak (from 440 nm to 672 nm). The relation between the integrated intensities and the temperature is illustrated in Figure 4.14b. The Figure indicates that the integral intensity decreases with increasing the temperature until 300°C then the integral intensities become constant. Moreover, for each wavelength range, the data points follow the same exponential function shown below:

$$I = I_0 \exp - \left(\frac{T}{T_0} \right),$$

where I_0 is the maximum intensity, T_0 is the temperature at which this maximum intensity can be achieved, and C is a constant. The fittted values of these parameters are: $I_0 = 1.53 \pm 0.12$, $T_0 = 43.43 \pm 4.45$, and $C = 0.01$

The exponential fit is shown by line curve in the figure 4.14b. This exponential decay of integral intensity with temperature can be employed to use Al-doped ZnO films as temperature sensor within the range of room temperature to 300°C. Beyond this range the spectrum is no longer sensitive to temperature change.

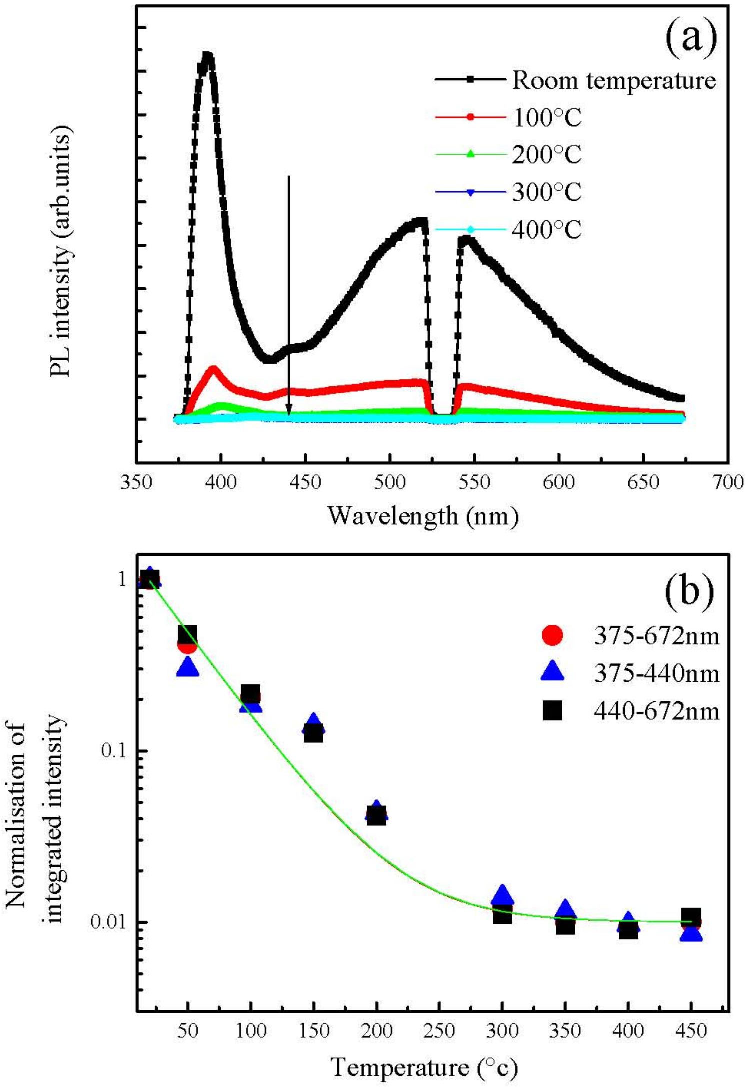

Figure 4.14: (a) Temperature- dependent PL spectra of the Al doped Zone film annealed at 900°C (b) Temperature-dependent of the integrated PL intensity for Al-doped ZnO (n(Al)/n(Zn) =0.051) annealed at 900°C. The green line is the exponential fit of the data points.

4.3 Hot-wall reactor deposition

4.3.1 Experimental procedure

Atmospheric pressure metaloraganic chemical vapor deposition (AP-MOCVD) of un-doped and-Al doped ZnO films were performed using a horizontal hot wall reactor (HWR).The set-up employed for this purpose was described in details previously (see chapter 3 section 2). It is interesting to note that in such kind of CVD-system, the temperature in the reactor is not constant over the whole heated length; as a consequence the substrate temperature depends on its position inside the reactor. In this context, C.Pflitsch and co-worker [5], who used this reactor to deposit aluminium oxide, observed the typically temperature profile of a single zone tube furnace. The profile along the flow direction was measured for different nominal furnace temperatures using a flow of 2000 standard cubic centimetre (sccm) synthetic air. The result are plotted in Figure 4.15. According to these results, five substrates were placed on a stainless steel bar holder and inserted inside the ceramic tube. The substrates used is this work were silicon wafers (Si (100) - orientation) and commercially available borosilicate glasses, both sized 20 mm×20 mm. Prior to each deposition experimental they were cleaned carefully with distilled water for few minute, after drying, all substrates were weighed. After deposition they were weighed again with a high-precision balance in order to calculate the growth rate and thickness of the obtained film. The substrates were positioned parallel to the gas flow in the radial centre of the chamber and were located at different positions as shown in Figure 3.5. The distances between the nozzle and the substrates, were 125 mm, 205 mm, 280 mm, 360 mm, and 425 mm for position A, B, C, D, and E, respectively. The supply pipe and the nozzle were heated at ~148°C to assure the transportation of the gas and to avoid precursor condensation. The $Zn(acac)_2$ and $Al(acac)_3$ were used as metalorganic precursors.

Both acetylacetonates are promissing candidates as precursors for the deposition of the ZnO:Al-films. They are commercially available, quite cheap, non-toxic and easy to handle, supporting the development of a low-cost industrial deposition process. Details of the thermal analysis of Zn(acac)$_2$ is given in the next section, while of Al(acac)$_3$ are reported in literatures [5, 133, 160]. During deposition of un-doped ZnO films, zinc acetylacetonate was sublimated at 118°C in a fluidized bed evaporator. The vapour was transported to the nozzle with a gas flow rate Φ_{air} of 600 (sccm) synthetic air. Before reaching the orifice, 1400 sccm synthetic air was added, in order to increase the gas velocity. In HWR, it is desired that the chemical reactions should occur along the entire tube in order to coat all the substrates. For this reason more quantity of precursor was used. This is almost thrice the amount used in case of HLR. The un-doped ZnO films were deposited at atmospheric pressure and at different furnace control temperature of 400, 450, 475, 500 and 550°C. Experiments deposition time were performed 1, 2, and 3 h. For the deposition of the Al-doped ZnO films, Al(acac)$_3$ was evaporated by using the same fluidized bed evaporator for controlling both precursors and transported to the chamber with a carrier gas flow of air$\Phi_{Al,air}$ which was varying for different Al-concentrations between 0 and 192 sccm. Before reaching the orifice, it was added to the above mentioned Zn(acac)2-vapor/air-mixture while the additional air flow Φ_{air} was decreased by the amount of $\Phi_{Al,air}$. Thus, the total flow of the gas mixture was constant for all experiments. Finally, the samples were allowed to cool down then take it out for the characterization.

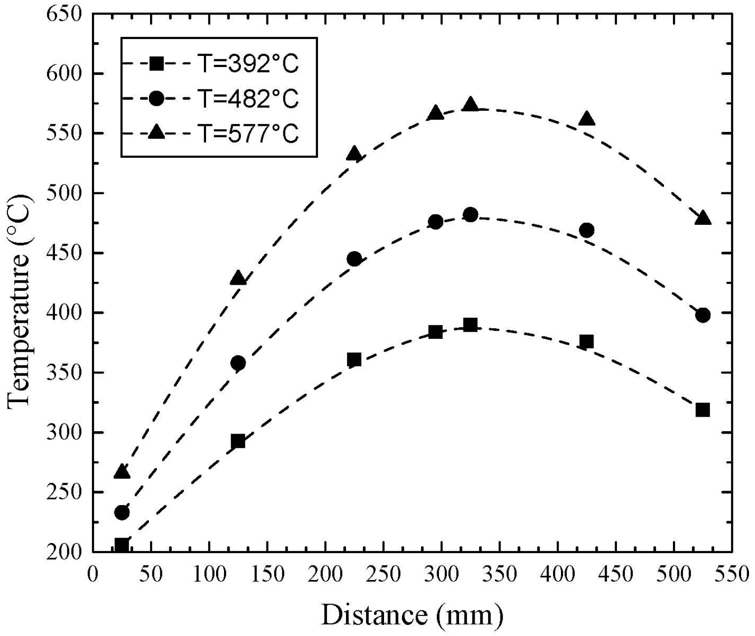

Figure 4.15: The temperature distribution in the furnace for three different furnace temperature (392,482 and 577°C)[5]

4.3.2 Thermal analysis of $Zn(acac)_2$in air

As mentioned above, the MOCVD-technique was used to deposit undoped and Al-doped ZnO films, using zinc and aluminium acetylacetonates as metal organic precursors. Here, the synthetic air was used as a carrier gas in stead of N_2 used in HLR reactor. Therefore, the thermal stability of zinc acetylacetonate precursor again were studied under synthetic air atmosphere. The precursor thermal stability was studied by meaning of thermal gravimetric analysis (TGA) and differential thermal analysis (DTA). The $Zn(acac)_2$ was heated in the temperature rage of 25-180°C with a 1 °C/min heating rate under synthetic air atmosphere. The Figure 4.16 shows the TGA and DTA results for the Zn(acac)$_2$ precursor under the mentioned conditions.

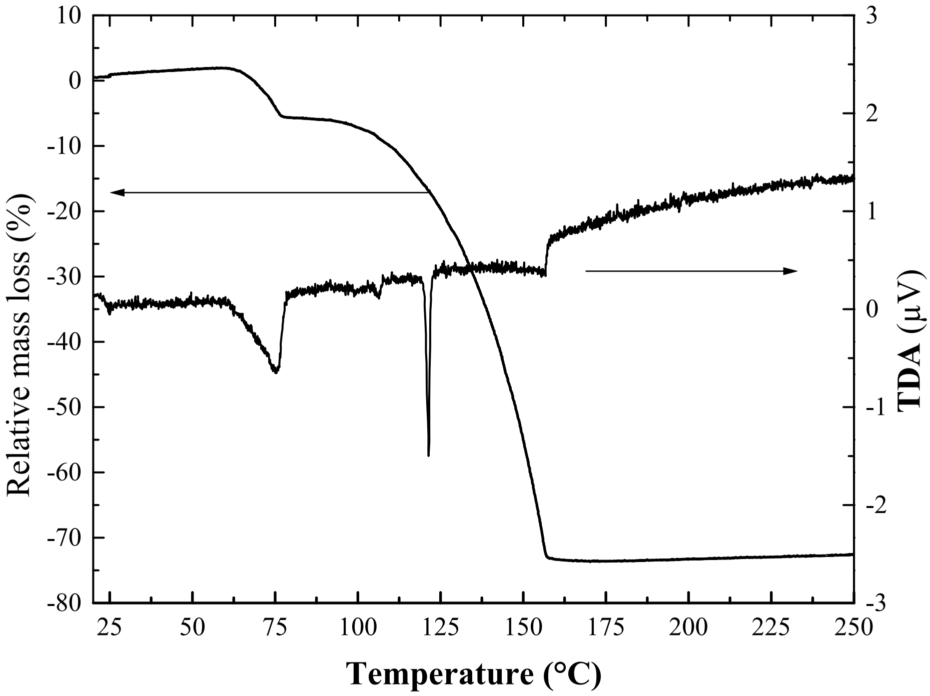

Figure 4.16: TGA/DTA analysis of the zinc acetylacetonate precursor: Zn(acac)$_2$ was heated in air atmosphere of 1000 mbar at a constant heating rate of 1°C/min.

The Figure shows that the weight loss of the precursor starts at about 85°C of the heating process. A similar result was found in N_2 atmospheric (see section 4.2.2). As a result, 85°C was considered as the lowest possible evaporation temperature for the precursor. The DTA curve shows two endothermic peaks. The first one at around 85°C is due to the vaporisation of water. While, the second one at around 123°C is corresponding to Zn(acac)$_2$ melting. According to this analysis a precursor temperature of 90-120°C in air atmospheric is recommended to transport the precursor

$Zn(acac)_2$ by evaporation. With this temperature range the weight loss is enough and no decomposition takes place. The temperature of 118°C was used to evaporate the precursor in order to conduct enough material to the reactor and to keep away from the precursor melting point. It can be seen in Figure 4.16 that the residual mass is slightly more (∼26 %) in air that in nitrogen atmosphere which is ∼22 % (as discussed in section 4.2.2). This suggests that along the water vapor as shown by T. Arri et al. [134], the oxygen present in air atmosphere may be also reacting with precursor to form ZnO.

4.3.3 Results and discussion

In the CVD process, the substrate temperature is a key parameter: by heating the substarte, one supplies, directly to the to the growing surface, additional energy that favorably influences the specific chemical reactions that lead to ZnO Growth.

4.3.3.1 Effect of substrate position and temperature

The position of the substrate in the hot-wall rector is an important parameter that strongly affects the film growth rate. This effect was reported previously by some authors [5, 161]. In order to analyse the effect of the substrate position on zinc oxide film growth rate, a set of deposition experiments were carried out onto silicon and glass substrates which were placed at five different positions. These positions were denoted as A=125 mm, B=205 mm, C=280 mm, D=360 mm, and E=425 mm away from the nozzle orifice. Here it is noteworthy that as the substrates are placed at different distance from the nozzle orifice more material is required for coating them. Hence, the quantity of the precursor used in HWR is 3 times more than that in HLR. As mentioned in section 3.1, the deposition experiments were conducted at a total flow rate of 2.0 slm for all experiments under atmospheric pressure and at five furnace control temperatures of 400, 450, 475, 500, and 550°C. At temperatures below 400°C no deposition was possible, similar to the film deposition in the HLR- CVD reactor (see section 4.2.3.1). Figure 4.17 shows the growth rate as a function of the substrate position and its temperature.

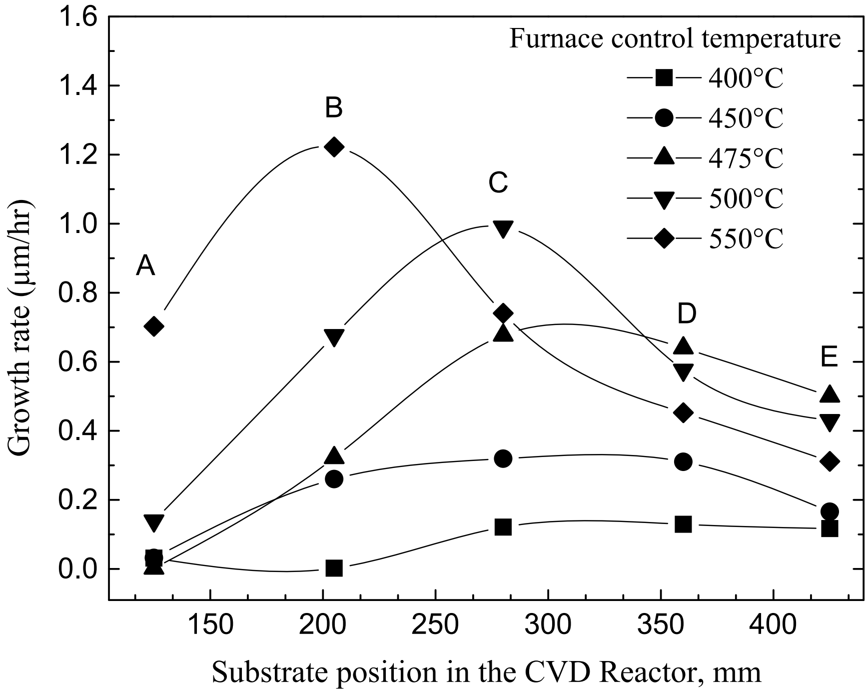

Figure 4.17: Growth rate of zinc oxide films deposited on glass substrate in HWR at atmospheric pressure as a function of furnace control temperatures

Initially, the effect of the substrate position on the growth rate was studied. At a given temperature, the growth rate increased with increasing distance between the substrate and nozzle orifice until position C was reached. A further increase in the distance resulted in a decrease of the growth rate. Meanwhile, the position B showed the highest growth rate at 550°C. These results may be attributed to the temperature profile in the reactor where the temperature increases inside the reactor until position C (isothermal zone) and then decreases. The decay of the growth rate at position beyond the position of the highest growth rate is due to the precursor depletion. The substrate temperature is another factor affecting the film growth rate. From Figure 4.17, it can be seen that at a given substrate position, the growth rate increases quite strongly with increasing furnace temperature, hence with increasing substrate temperature. This suggests a kinetically controlled surface domain. At the high furnace control temperature of 550°C, the maximum growth rate of around 1.2 µm/hour is shifted to position B due to the rise in the substrate temperature, which is enough for complete precursor decomposition. The growth rate at the lower position (i.e. position A) is lower because it is a colder zone so that the precursor reacts slower. However, even in this case, the growth rate at position A cannot be negligible in comparison to the rates measured at locations within the isothermal zone. Additionally, an interesting result that can be obtained from Figure 4.17 is that the deposition at 450°C (furnace control temperature) is quite homogeneous over the complete distance between positions B and D. Thus, the furnace control temperature of 450°C was used for the following investigations. Experimentally the measured furnace temperature was not the actual substrate temperature due to the heat loss between the reactor and the substrate. The substrate temperature was determined by using the temperature distribution curve (see Figure 4.15). The results for the growth rate considering the furnace and the substrate temperature were then compared and plotted in Figures 4.18(a, b). In the figure it is seen that the substrate temperature is slightly lower then furnace control temperature For example at furnace the controle temperature of 400°C , the substrate temperature was 375°C, 380°C and 388°C at B,C,and D positions respectively. This results, can be attributed to the distribution of temperature within the reactor.

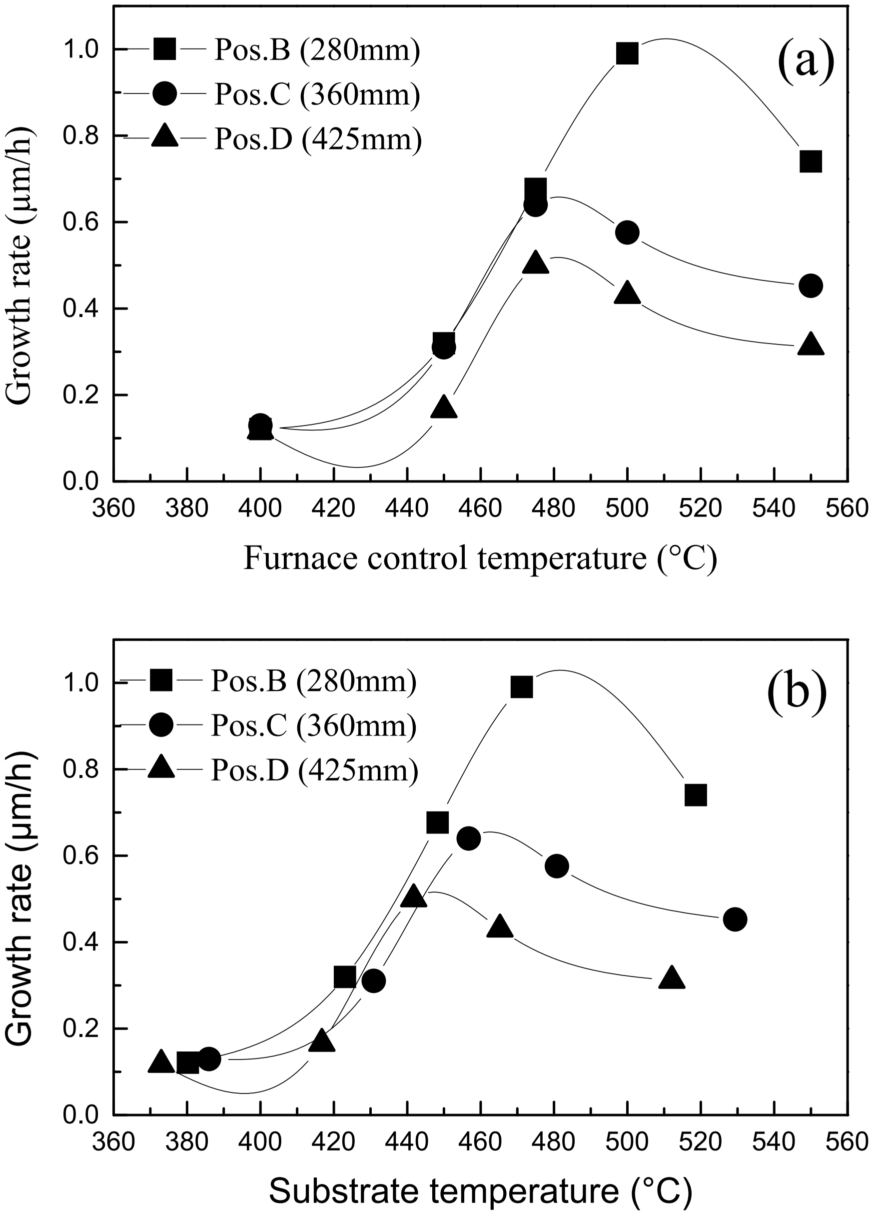

Figure 4.18: Growth rate of zinc oxide films deposited on glass substrate in HWR at atmospheric pressure; (a) as a function of furnace control temperatures, (b) as a function of substrate temperatures.

Table 4.4: Growth rates of ZnO films at different temperatures deposited using HLR and HWR

	Growth rate (µm/h) @			
	Deposition technique	450 °C	500 °C	550 °C
HLR	MOCVD	0.14	0.16	**0.23**
HWR*	MOCVD	**0.30**	0.98	0.73
Kamata et al. [131]	MOCVD	7.2	7.2	7.2
Maruyama et al. [136]	MOCVD	--	1.8	--
Tan et al. [151]	MOCVD	2.5	3.3	--
Natsume et al. [162]	MOCVD	--	--	**0.22**

*The growth rates are determined with respect to the sample in position C

It can be seen from table 4.4 that the growth rate of ZnO films in HWR is nearly an order of magnitude less than those reported by Kamata et al [131], Maruyama et al [136], and Tan et al[151] This is due to the low sublimation temperature of the precursor (as discussed in section 4.2.3.1). The growth rate in HWR at 450°C is nearly equal to that in HLR at 550°C and is also in agreement with that reported by Natsume et al [162] (see table 4.4). It has been discussed earlier that at 550°C, the films deposited using HLR shows best results. Growth rate has a profound effect on film properties [77, 28]. As such, it is desired to maintain similar growth rate in HWR for comparing the films with HLR. At 450°C, not only the films obtained are more homogeneous but also the growth rate is similar to that of HLR at 550°C.

4.3.3.2 Effect of deposition time

The deposition was performed under ambient pressure on both substrates (silicon and glass). As analysed by XRD, the deposited films were crystalline above furnace the controle temperature of 400°C. In the following experiments the deposition temperature of 450°C was chosen to study the effect of substrate position and deposition time on thickness of the films. Again, the thickness of the films were calculated from the change in mass (formula as given in section 2.3.6). The results are presented in Figure 4.20 (a, b). The effects of film thickness on substrate position and deposition time (1, 2, and 3h). As expected, these results show that the film thickness increases with increasing deposition time at all positions within the furnace. However, the growth rate is inhomogeneous as the local deposition temperature is inhomogeneous. This inhomogenity can be better seen in Figures 4.20 (c,d) where the film thicknesses are plotted as a function of the deposition time for each substrate position. It is seen that the film thickness increases nearly linearly with time, indicating that no depletion of the precursor occurs within the evaporator. This also indicates that the film thickness can be controlled by varying the deposition time. However, the derivations of the curves vary between 0.48 µm/h in the middle of the furnace and 0.15 µm/h at the outer position. This is expected as the local deposition temperature has a parabolic profile and the growth strongly depends on the deposition temperature (see section. 4.2.3.1). This inhomogenity must be considered for the prediction of the film thickness.

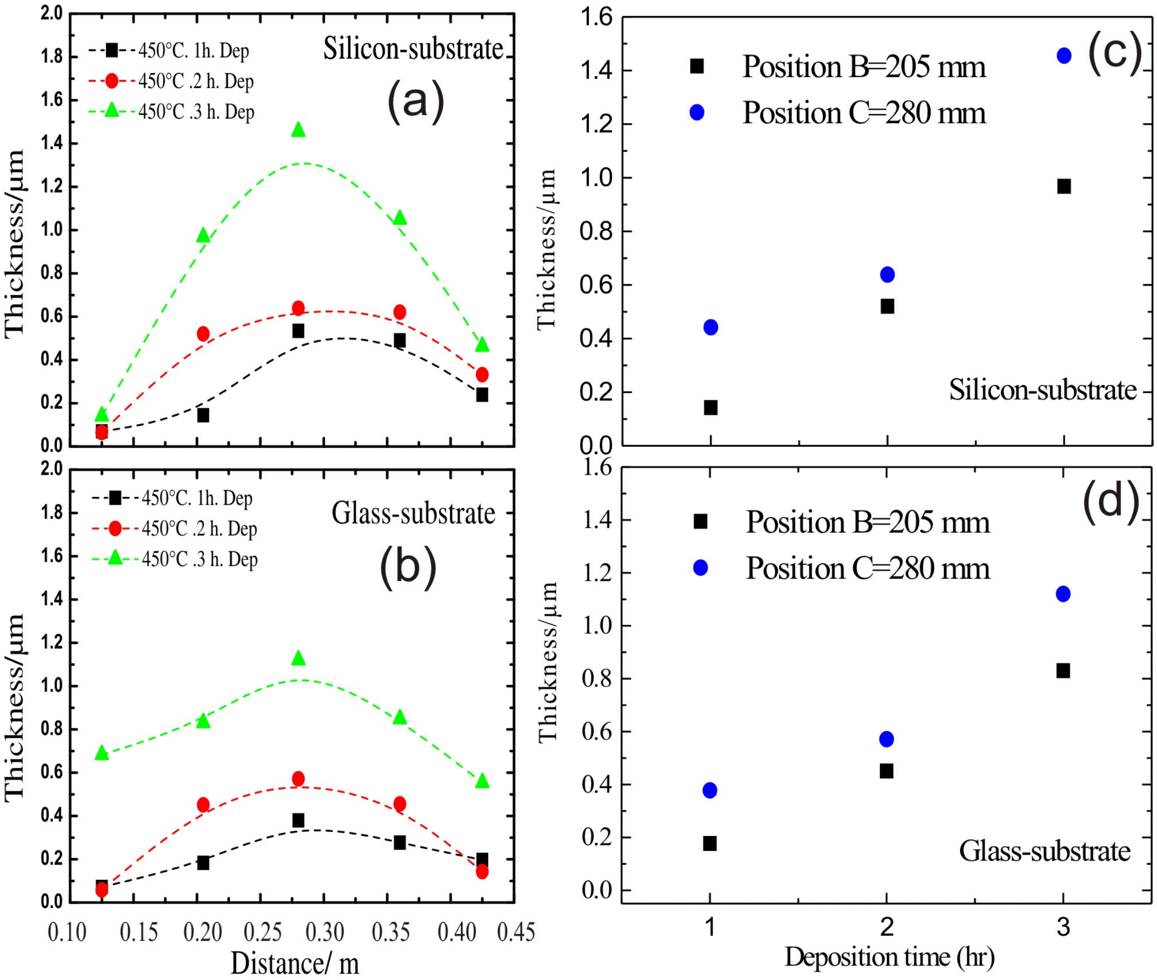

Figure 4.19: Thickness of thin zinc oxide films deposited on silicon and and glass at 450°C (furnace control temperature) plotted as a function of deposition time.

4.3.3.3 Chemical composition

In order to further confirm the deposition of ZnO and the aluminum incorporation into the films, The films prepared of a thickness of ∼2 µm , which was deposited within 3 h at 450°C at position C ∼300 nm in the HWR were analyzed by EDX, which gives information about the chemical composition. Typical EDX spectra of undoped and Al doped films are given in Figure 4.20a , the spectra of one un-doped ZnO film, and one Al doped film which were prepared by using a flows of $\Phi_{Al,N_2} = 120$ sccm and $\Phi_{Zn,N_2} = 600$ sccm air carrier gas through the acetylacetonates evaporators. This analysis shows the sharp peaks of zinc and oxygen, which conforms the presence of ZnO in the film. The EDX spectrum of the Al doped ZnO films also shows the peaks of zinc and oxygen in addition the peak of the aluminium, confirming the presence of the aluminium dopant in the film. For the un-doped ZnO-film (lower spectrum in Figure 4.20a), the software of the calibrated EDX- setup reveals the presence of $\sim$44,7% Zn, $\sim$55,3% O . For the Al-doped film (upper spectrum in Figure 4.20a), the EDX-measurements reveal the presence of ˜43,9 % Zn, ˜55 % O, and ˜2 % Al. It should be noted that each data is the average of three EDX measurements The Al/Zn concentration in percent (%) within the films, which was calculated from the peak intensities of the EDX -patterns is plotted in the left part of Figure 4.20as function of the ratio flows rates $\Phi_{Al,air}$, and $\Phi_{Zn,air}$ of the carrier gases through the evaporators. Also each data point is the average of three EDX measurements and the errors are the standard deviations. Clearly from Figure 4.8b the amount of aluminium correlates with the flow of carrier gas through the aluminium evaporators. Assuming the Al and Zn evaporators to be saturated, the Al flow Φ_{Al} is proportional to the concentration of Al in the reactor and the Zn flow Φ_{Zn} is proportional to the Zn concentration. The ratio $\frac{n[Al]}{n[Zn]}$ as a function of the ratio of the used carrier gas flows $\frac{\Phi_{Al,N_2}}{\Phi_{Zn,N_2}}$was fitted by a line (dashe line in Figure4.20b). Al content can be well controlled.

$$\frac{n\left[Al\right]}{n\left[Zn\right]} = 0.22.\frac{\Phi_{Al,air}}{\Phi_{Zn,air}} \tag{4.5}$$

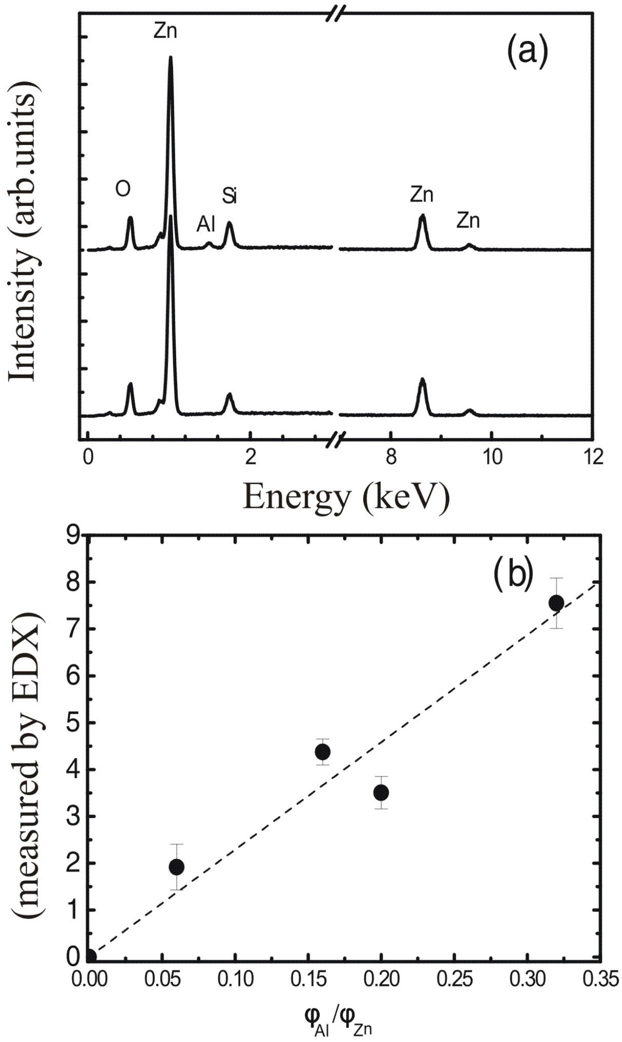

Figure 4.20: EDX-analysis of the grown films: (a) shows the typical EDX spectra of one un- doped and one Al-doped ZnO-film which was prepared by using a flows of $\Phi_{Al,air}$= 96 sccm and $\Phi_{Zn,air}$= 600 sccm air carrier gas through the acetylacetonate evaporators. (b) shows the Al/Zn-concentration within the films as function of the flow rates $\Phi_{Al,air}$, and $\Phi_{Zn,air}$of the carrier gases through the evaporators. Each data point is the average of three EDX measurements. The error is the standard deviation.

4.3.3.4 Film structure

Film growth could be easily detected, not only by measuring the change in weight of the sample after deposition but also by analysing the change in the structural properties. Various films of un-doped and aluminium doped zinc oxide (ZnO) were prepared by following the procedure described in the section 4.3.1: the films were deposited at furnace control temperature between 400 and 550°C at position C, which is the centre of the reactor. Silicon and borosilicate glass were used as substrates. Most of these films were analyzed by XRD using two different geometries: grazing incidence X-ray diffraction and Bragg scan; these two geometries are explained in details else where (chapter 2 section 5.1). In Figure 4.21 , the XRD spectra of undoped ZnO films are shown. The films were deposited on glass and silicon substrates respectively, at different substrate temperatures (400, 450, 500, 550°C). Figure 4.21 (a) shows films deposited on glass substrates. Even at a substrate temperature of 400°C, most of the diffraction peaks of ZnO,(100), (002), (101) and (110) are observed. This indicates that the films start growing at the mentioned temperature 400°C. At low temperature (<500°C) the films show a predominantly (100) and (101) orientation. Whereas, at high temperature 550°C show higher intensity of the (002) peak compared to the other ZnO diffraction peaks. The Figure 4.21(b) shows the XRD patterns of the films deposited on silicon substrate. The same diffraction peaks are observed (< 500°C) as Figure 4.21 (a). At 550°C the dominant peak was (103) orientation, which presumably is a result of the glass substrate. In the following study a deposition temperature of 450°C was chosen for the deposition of aluminium doped ZnO films. Because of the previously reason, quite homogenous film, low temperature, crystalline films was observed.

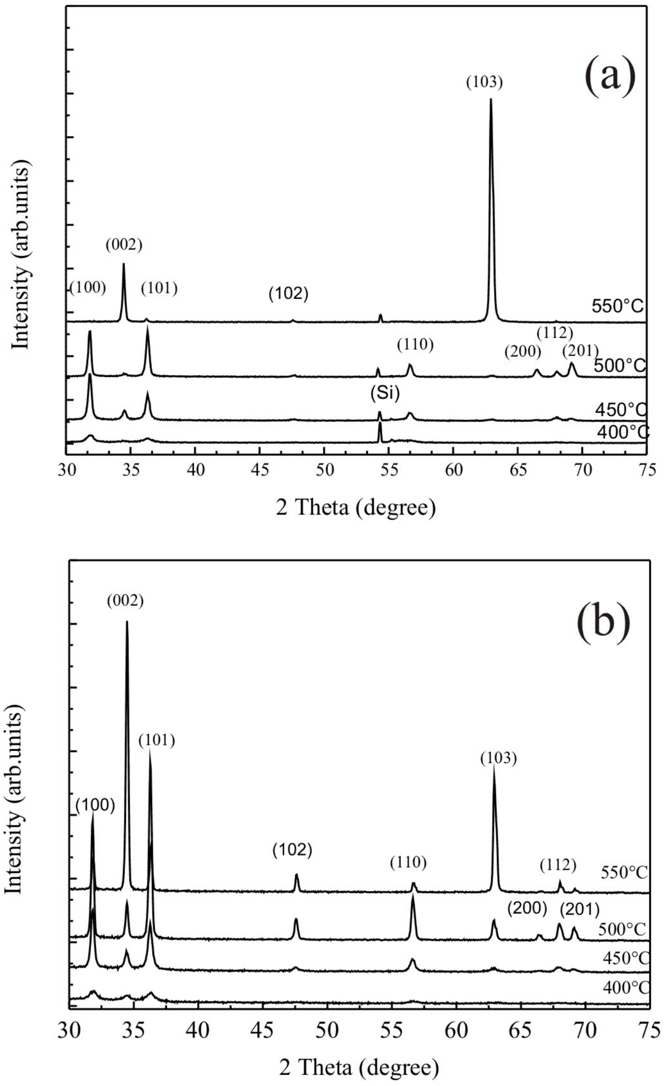

Figure 4.21: XRD patterns of Al doped ZnO deposited on silicon and borosilicate glass substrates by (HWR) reactor at 450°C at position C (detector scan).The XRD patterns are shifted for better comparison.

In contrast to the undoped ZnO films, the typical XRD of Al doped ZnO films (Al-4.4 %) on both substrates Figure 4.21 show most of the expected reflections. It can be seen that Al-doped ZnO films show dominat (100) reflection both in glass as well as silicon. The XRD results shown in Figure 4.21 were performed with detector scan with a fixed angle of incidence ($\theta = 2°$). Detector scan is normally performed for phase identification and is surface sensitive. As such, in order to get more information about the preferred orientation of the sample, it is necessary to probe deeper into the sample. This geometry is termed as Bragg scan. The features of both Bragg scan as well as detector scan are presented in detail in chapter 2 (section 2.2.1). XRD measurement with Bragg scan was also performed to get more information about the structure and a possible preferred orientation.

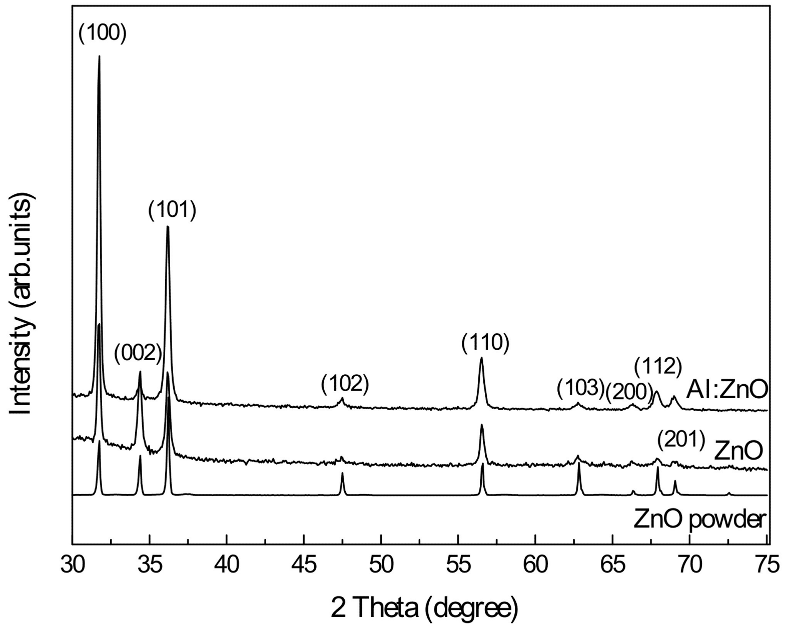

Figure 4.22: XRD patterns of ZnO powder, undoped and Al doped ZnO deposited on borosilicate glass substrates by (HWR) reactor at 450°C at position C (Bragg scan). The XRD patterns are shifted for better comparison.

Figure 4.22 shows the X-ray diffraction (XRD) patterns of un-doped and Al-doped ZnO films deposited using HWR on glass substrate measured with Bragg scan. The XRD patterns of ZnO powder (>99 %, Sigma-Aldrich) measured with the same geometry is included in Figure 4.22 for comparison. It can be seen that both un-doped and Al-doped ZnO films show all reflections as is observed in case of ZnO powder. Similar to ZnO powder, un-doped ZnO film show no preferred orientation. However, for Al doped sample, the relative intensity of (100) peak at $2\theta = 31.7°$ was observed to be highest compared to the other diffraction peaks. While comparing the XRD patterns of ZnO powder and un-doped ZnO film, it can be said that the crystallites of Al-doped ZnO films developed using HWR are preferentially orientated along the (100) axis (a-axis). These results indicates that Al-doping gives rise to highly a-axis oriented crystallites. It should also be noted that a set of doped samples were analyzed with Bragg scan to check the reliability of the measurement and obtained similar results in each case. In case of Al-doped ZnO films developed using HLR, preferred orientation along the c-axis ((002) reflection) was observed instead of a-axis ((100) reflection). This maybe due to the difference in the growth process involved in these two deposition techniques. Al-doped ZnO films are commonly orientated along (002) due to its low surface free energy [163, 164, 165, 166]. But, studies show that the surface free energy of the (002) plane is not necessarily always smaller than those of other planes [167]. Another orientation can be achieved if either a large density of defects in the form of vacancies, interstitials and impurities exist in the films or the deposition is performed at non-equilibrium state such as, low temperature, high deposition rate, etc., [168]. This may be the reason for the a-axis orientation of the HWR deposited Al-doped films.

4.3.3.5 Film morphology

To complete the study of the structure features of ZnO films as function of the deposition temperature, some films were analysed by scanning electron microscopy (SEM). Figure 4.23 shows typical surfaces of un-doped ZnO films on silicon substrate which were depositive 2 h deposition time. The films were deposited at position C using different furnace control temperatures of 450°C, 500°C, and 550°C. On the SEM images of the films Figure 4.23 (a, b, and c), it is clearly observed that the surface morphology changes significantly with increasing deposition furnace control temperature from 450°C to 550°C, which is in good agreement with the XRD results. Indicate again that the increase of the deposition temperature emphases the crystallite of the ZnO films. The Films grown at high temperature 550°C Figure 4.23(d) shown clearly a hexagonal surface in the top view of the sample, where the ZnO –grains are well orientated.

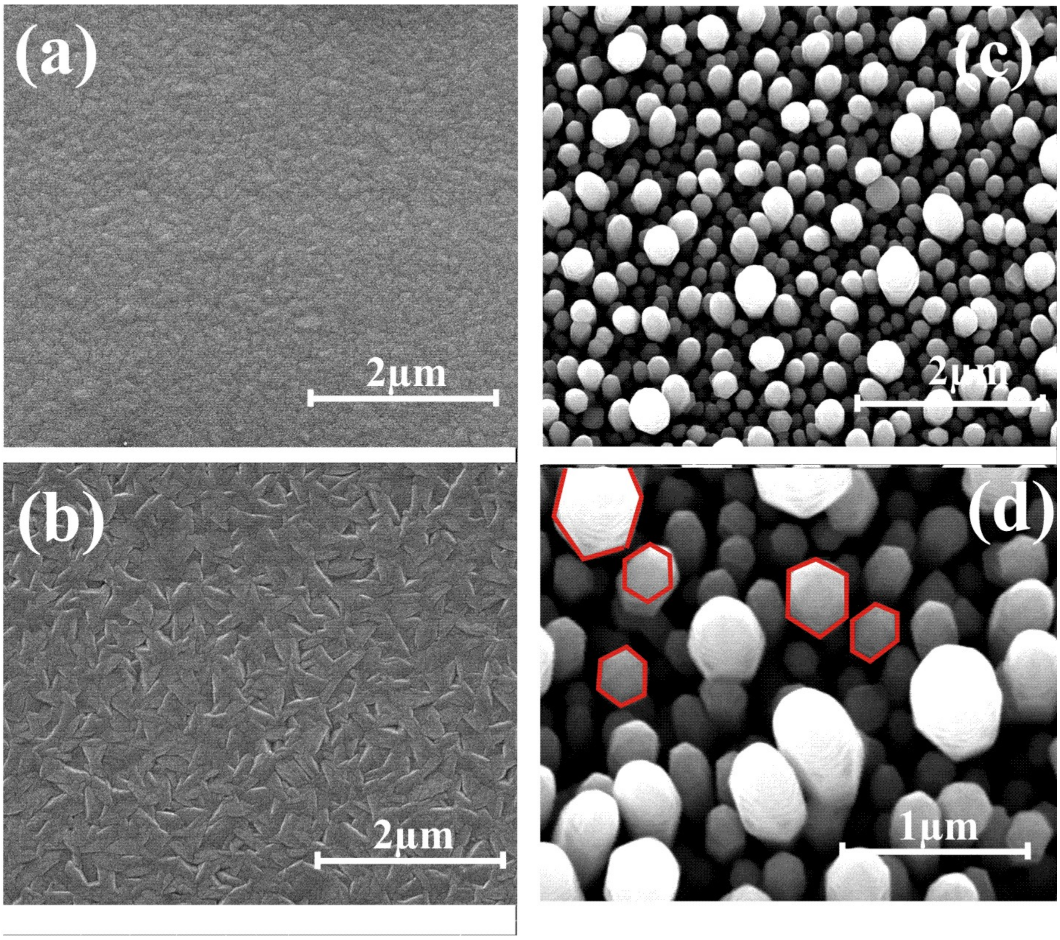

Figure 4.23: SEM images: (a, b, c, and d) are top views of ZnO films growth on silicon substrate at ambient pressure and by using a hot-wall CVD set-up.(a) 450°C, (b) 500°C, and (c,d) 550°C. (d) high magnification (all at position C after 2h deposition).

4.3.3.6 Optical properties

As transparency is the most important property in the application of Al doped zinc oxide films as transparent conducting oxide (TCO), the transmittance of un-doped and Al-doped ZnO films was measured at room temperature. The Figure 4.24 shows the transmittance spectra in the wavelength range of 300-800 nm for the samples of a ∼0.4 µm, which was deposited within 1 h at 450°C at position (C ∼300 nm) in the HWR.

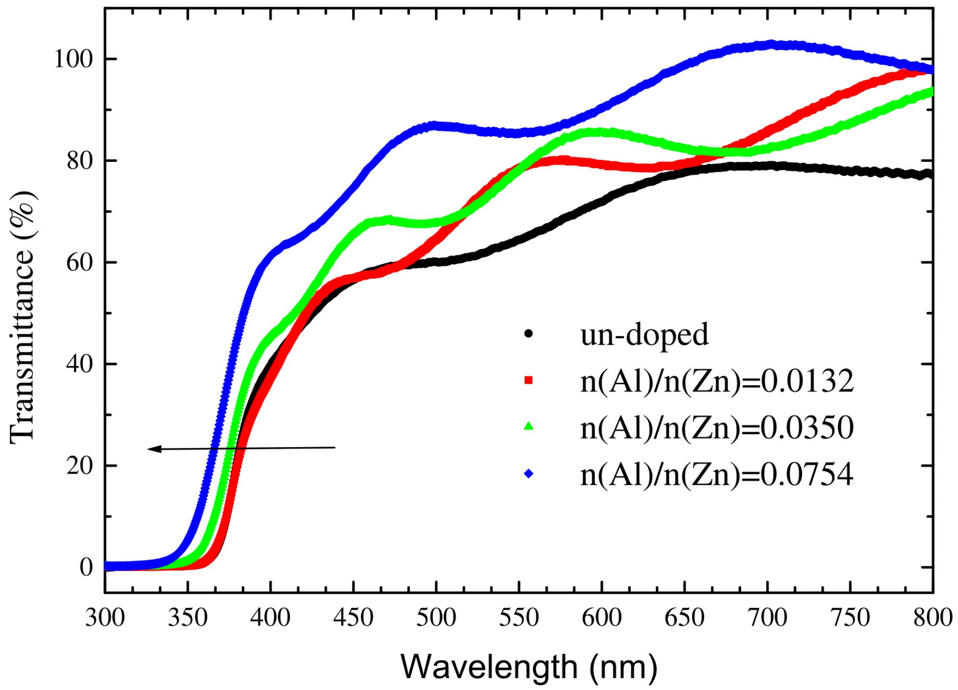

Figure 4.24: Optical transmittance spectra of un-doped and Al doped ZnO films on borosilicate glass for different dopant concentration at 450°C at position C.

For undoped ZnO film have a transmittance of about 65% in the visible range (400-800 nm) having the band edge at around 387 nm, as seen from Figure 4.24. The un-doped films deposited using HWR are less transparent than that deposited using HLR which posses a transmittance value of about 80 % in the visible range. In case of HLR, films are deposited at higher substrate temperature (550°C) than in HWR (450°C). As a result HLR deposited films posses a well oriented films structure (see section 4.2.3.2) while HWR films are polycrystalline in nature (see section 4.3.3.4) [169]. As can been seen from Figure 4.10, the transparency of the films improved with increasing the aluminium concentration in the films. Similar behaviour was observed in case of films deposited using HLR. After Al-doping treatment, the optical transmittance increases up to 80 % in the visible range, and the transmission edge is blue shifted also termed as Burstein-Moss shift [170, 150, 171]. This result depicts that the optical band gap (E_g) of the films was influenced by introducing aluminium dopant. Smilar phenomena was observed in case of HLR.

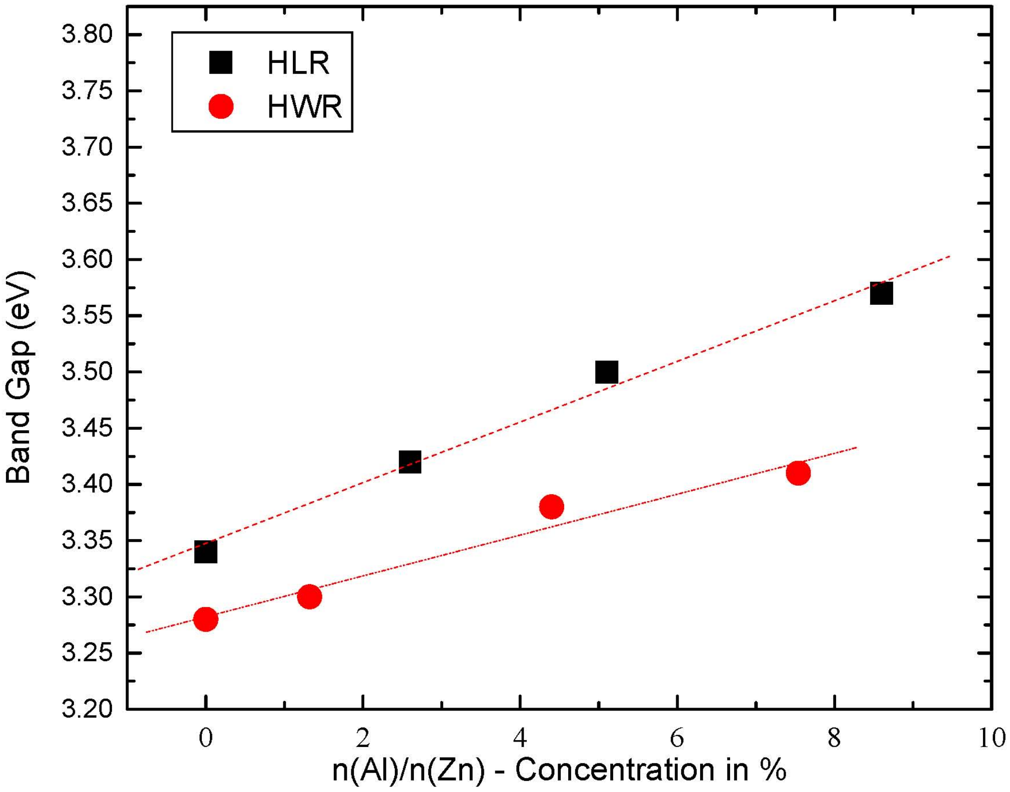

Figure 4.25: Variation of the energy gap,E_g as a function of the doping content of the ZnO films deposited using HLR and HWR..

Figure 4.25 shows the variation of the band gap of Al-doped ZnO films deposited using HWR as a function the Al concentration. The band gap of these films varies linearly according to the following relation

$$E_g\left(eV\right) = 3.28 + 1.8\frac{n\left[Al\right]}{n\left[Zn\right]} \tag{4.6}$$

For comparison, the E_g values of HLR were also included in the Figure 4.25. As in HLR, the Eg values of the films deposited using HWR also increases with Al concentration. However, the values are lower than the films deposited using HLR. Also the rate of change of band gap in HWR is less compared to HLR (see 4.4). This variation in the behavior of the band gap can be attributed to the film structure. Being polycristalline, these films posses higher density of grain boundaries. Thus, the electrostatic potential that exist along the grain boundaries has a pronounced effect on the band gap of HWR deposited films [172].

Table 4.5: Electrical and optical properties of the grown films. Legend: n(Al)/n(Zn)= molar ratio of Al- to Zn-atoms within the films, *d*= thickness, ρ =resistivity, E_g = band gap

Al-Flux (sccm)	0	36	120	192
$\frac{n[Al]}{n[Zn]}(\%)$		1.32	4.4	7.54
d(µm)	323±0.13	470±0.42	460±0.6	415±0.47
$\rho(\Omega.cm)$	2.5±0.1	30±0.4	5.5±0.6	1.4±0.5
E_g	3.28	3.34	3.49	3.76

4.3.3.7 Electrical properties

As mentioned previously, in the application of ZnO: Al films as a transparent conductors, also the electrical properties of the films are an important . Therefore, the electrical resistivity of some ZnO: Al films of about 0.323 to 0.447 µm thickness were measured by the four point probe method. More details for this method are given in the section 2.2.4. To study the effect of Al concentration on the electrical properties, a series of Al-doped ZnO films with different Al/Zn ratio were deposited. The results show that the films posses high resistivity of 2.5 Ωcm and 1.4 Ωcm for un-doped and Al doped films respectively. These resistivity values are much higher than those deposited using HLR. The reason for the difference in the resistivity of un-doped and Al-doped films deposited using these two systems could be due to the difference in their structure. The XRD patterns of these films (Figure4.6 and 4.21) show that the films are more oriented in HLR deposited samples than in HWR ones. At 450°C, the HWR deposited samples are polycrystalline resulting in higher density of crystallite boundaries while, the HLR deposited ones at 550°C show preferred orientation along (002) peak. As such, the electrons are more scattered in HWR deposited samples. This leads to higher resistivity in such samples.

4.4 Summary

For the deposition of undoped and Al-doped zinc oxide films, two systems were used: HLR and HWR reactors. The HLR experimental set-up is more complicated due to use of different devices such as, vacuum pump, halogen lamps, and cooling system, etc. This required more effort and time in order to produce coatings. In contrast, the HWR is characterized by simple set-up construction and required less time for deposition. In the HLR, the quantity of the precursor used was less compared to HWR. The number of the coated substrates which can be produced using the HLR is limited to one, whereas in HWR several substrates can be coated simutaneously. In the first system, only the substrate was heated using halogen lamps while in the second system, the entire tube furnace along with the substrates were heated by electric source due to which, the film material also get deposited at the reactor walls. As a result of comprehensive study, two deposition temperatures of 550°C and 450°C were used for HLR and HWR respectively. High quality ZnO films were obtained by using the above mentioned temperatures. At a partcular temperature, the growth rate of ZnO films deposited using HWR is more than that using HLR. However, the growth rate of the films deposited using HLR at 550 °C is nearly equal to that of HWR at 450 °C. This value is similar to that reported by Natsume et al [162]. Although the growth rates were kept similar, the film properties such as, structure, resistivity, and transparency were found to be different for both systems. In HLR, ZnO films are oriented along (002) plane and no significant change in orientation due to doping has been observed. However, in HWR, the un-doped ZnO films are polycrystalline in nature. But with doping the intensity of (100) peaks enhance significantly. The resistivity measurements reveal that aluminum doping has significant influence on its electrical properties of Al-doped ZnO film. The films deposited using HLR show higher resistivity values than HWR. The films are highly transparent in the visible range in both deposition systems. The transparency value of the un-doped ZnO films deposited using HLR and HWR were about 80% and 65% at 500 nm respectively. The films deposited using HLR is more transparent. In addition, Al -doped films deposited using both systems show a high band gap energy.

In the next chapter will explore the possibilies of another widely used functional metal oxide films- TiO_2 for totally new area as temperature sensor and also a protective coating.

5 Deposition of un-doped and doped TiO_2 films

5.1 Introduction

Titanium dioxide TiO_2 is a multifunctional metal oxide which have attracted much interest due to their interesting chemical and physical properties and possible applications[34]. A brief overview about the structure and applications of TiO_2 was mentioned previously (see chapter 2). In the present chapter, the preparation methods used for developing un-doped and doped titanium dioxide TiO_2 films were discussed. Two deposition techniques were involved; one using chemical route, called sol gel and other one a physical vapor deposition, cathodic vacuum arc. Sol gel method with dip coating technique was used to prepare undoped and europium doped TiO_2 films onto silicon substrates while cathodic vacuum arc followed with thermal oxidation thechnique was used to develop highly adhesive pure rutile phase TiO_2 films onto stainless steel substrates. A brief overview of these methods is given in chapter 2. This chapter can be divided into two sections: (i) sol-gel deposition of undoped and europium doped TiO_2 films- (ii) thermal oxidation of titanium deposited by the cathodic vacuum arc method. The goal of $TiO_2 : Eu^{3+}$ film is to use the as surface temperature sensors. To our knowledge, doped titanium dioxide has not been investigated yet for this application. The results of europium doped anataseTiO_2 films are shown in the first section. In the second section, the protective behaviour of titanium dioxide films developed using cathodic vacuum arc onto stainless steel substrates has been investigated. Usually, most studies on titanium dioxide films are focused on film deposition and film composition. Less attention has often been paid on film adhesion. In the case of hard coatings on steel, a comparative study of previously mentioned methods was reported [117] to evaluate the adhesion behaviour of TiN coating on steel. The report suggest that the cavitation erosion can successfully be used for the study of the adhesion behaviour. Thus cavitation erosion has been used for testing the adhesion of titanium dioxide (TiO_2) rutile phase / Stainless steel (AISI 304).

5.2 Sol-gel deposition of undoped and europium doped TiO_2 films

For temperature measurements, thermocouples, thermistors, or pyrometers are usually used. However, temperature measurement under challenging conditions, such as measuring the temperature of vibrating, or moving surfaces with non-optical methods is problematic. In such cases, and also if the temperature of transparent surfaces shall be evaluated, the optical method using thermographic phosphor thermometry is preferable, which has the advantages of being non-intrusive, being independent from the emissivity of the surface, and does not require a physical contact between the sample and the electronics. The development in the field of thermographic phosphors used for temperature measurement was recently reviewed by S.W.Allison et al [81]. The thermographic phosphors (TPs) utilize the concept of doping generally ceramic materials with rare earth or transition metal ions, whose properties, such as phosphorescence decay time, intensity and spectral distribution, following an excitation with a light source are temperature dependent. For this purpose, a surface is coated with such a phosphorescing material. The measured phosphorescence decay lifetime following irradiation by laser light or a flash lamp is a function of the temperature and can thus be used to determine the surface temperature of the coated surface. Usually, transition metal and rare earth doped ceramics are used as surface-temperature sensors [81, 173, 174], since these materials have a relatively long phosphorescence decay time, which is therefore easy to measure. However, if host materials like alumina are used, the crystallization temperatures may get very high, being a problem for several substrates. In the present study TiO_2 doped with europium (III) was studied as an alternative which crystallizes at moderate temperatures and could be used to measure surface temperatures.

5.2.1 Experimental

5.2.1.1 Experimental materials

The chemicals used for film deposition were: Ethanol CH_5OH (analytical grade,VWR Prolabor), tetra-isopropyl orthotitanate $Ti\,(C_3H_3O)\,4$(Merck), nitric acid HNO_3 (purity, company) and europium (III) acetylacetonate hydrate ($(C_5H_7O_2)_3$ Eu. 2 H_2O) ($>$ 98%, Aldrich)

5.2.1.2 Synthesis of the $TiO_2 : Eu^{3+}$ films

The sol-gel dip coating technique was used to prepare Eu^{3+}doped TiO_2 films. The preparation relies on a method of Samuneva et al [52], which was developed for the preparation of un-doped TiO_2 films. The method is based on the use reported by tetra-isopropyl orthotitanate as the titanium source, ethanol as solvent, and HNO_3 as catalyst. In the present case, a small amount of $Eu(acac)_3$ was added as europium source. For the preparation of 4.42 ml sol, 0.0148 mol tetra-isopropyl orthotitanate was dissolved in 25 ml ethanol, and then 5.4 µl HNO_3 were added to the solution. The concentration of Eu^{3+}in TiO_2 was obtained by the relation $(X_{Eu(acac)_3}/X_{Ti})$, where X is the molar ratio . The Eu^{3+} concentration was varied over a range of 0.26-1.14 mol percent by adding weighed amounts of Eu(acac)$_3$ to the sol (0.019-0.082 gm). The resultant solution was stirred at 60 °C for 30 min until a transparent sol was obtained. Silicon substrates were coated then by using a dip coating method. Figure 5.1 shows a flowchart of the procedure that was used for synthesising the un-doped and europium doped TiO_2 films using dip coating technique. In additional, Figure 5.2 shows in details the photographs of the preparation sequences of the dip-coating technique.

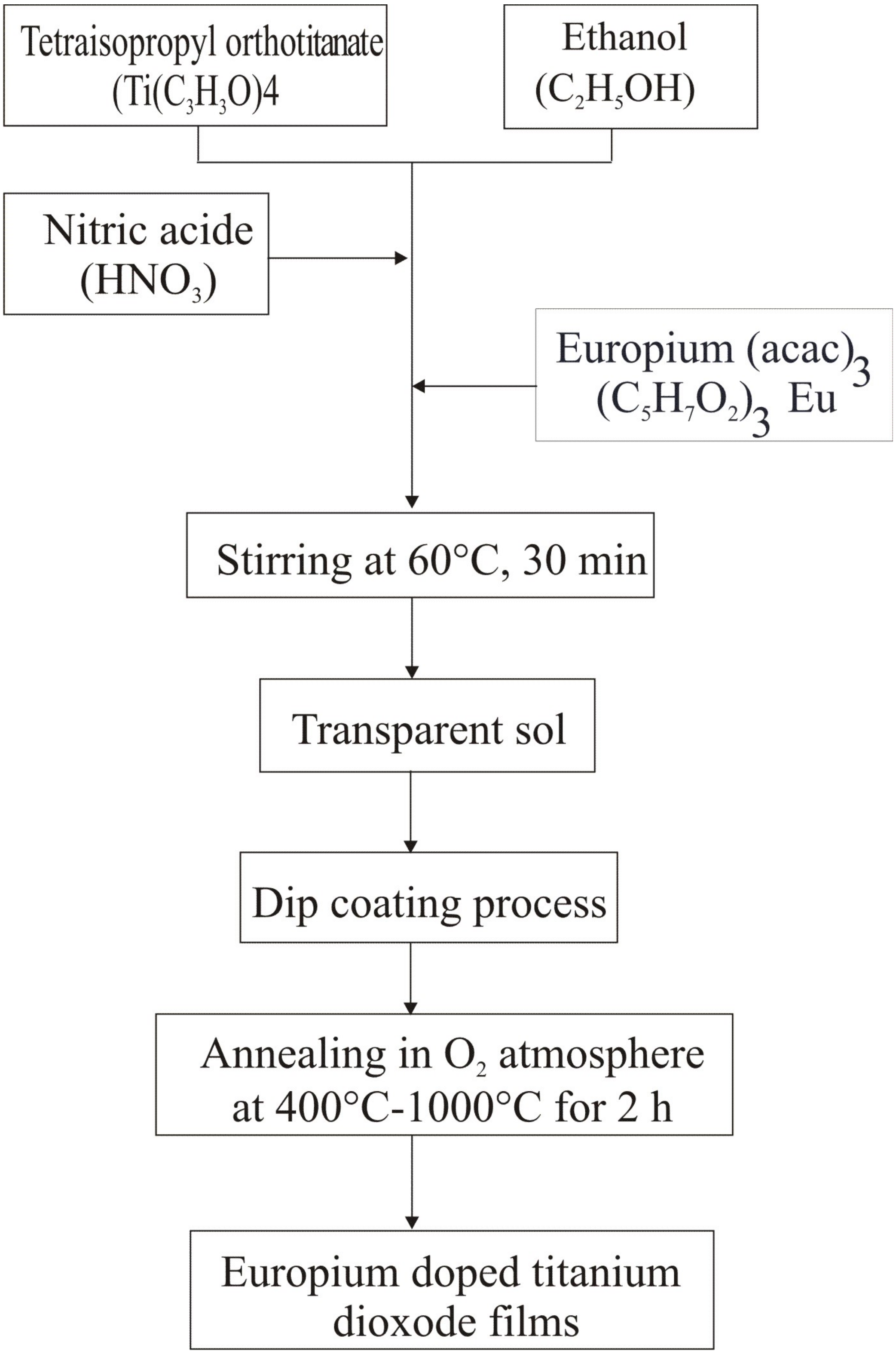

Figure 5.1: Flowchart showing the sol-gel procedure for preparing the un-doped TiO_2 and europium-doped TiO_2 films

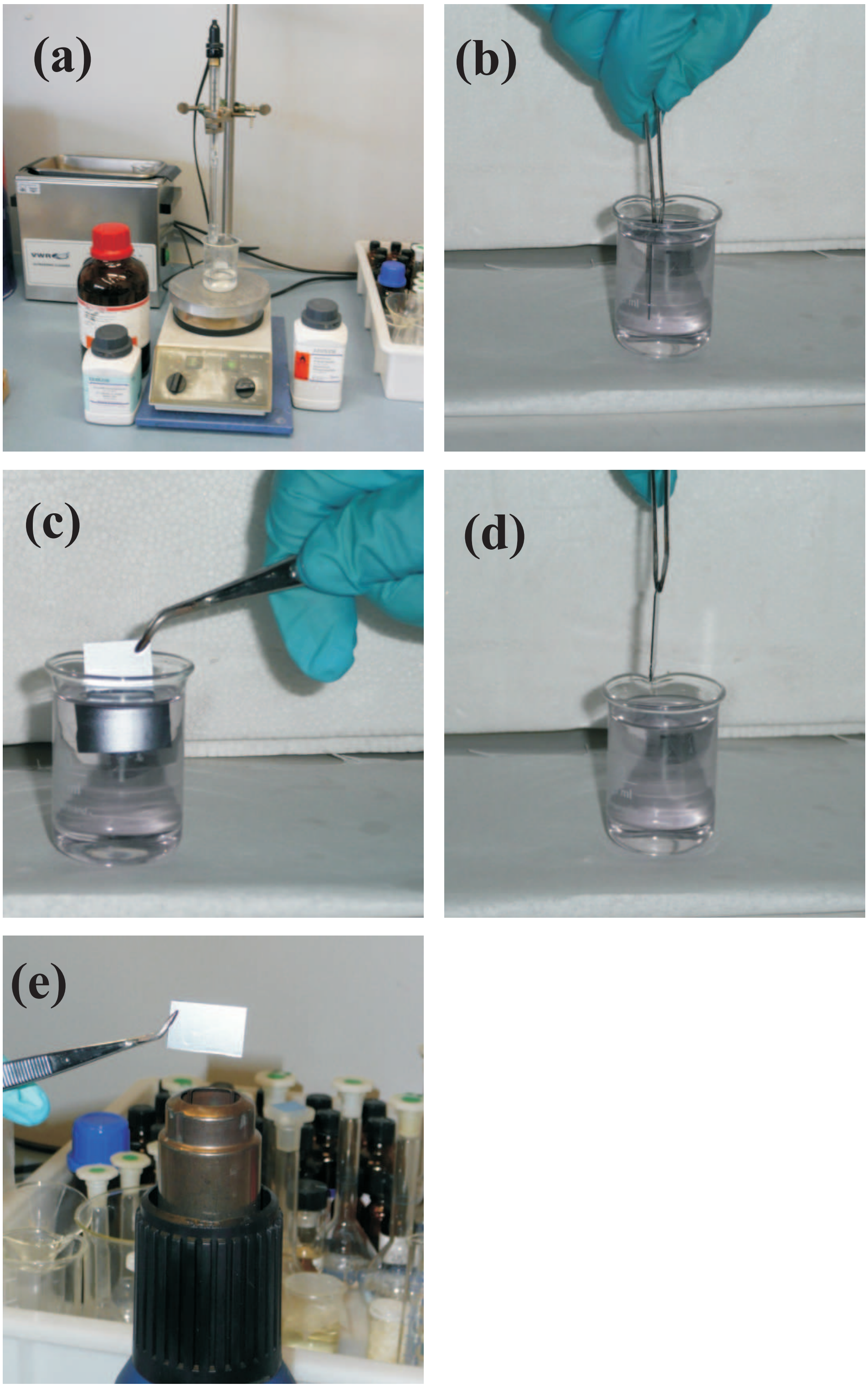

Figure 5.2: Dip coating technique (a) Sol-preparation; (b)-(d) Dip- coating process; (e) Drying the coated substrate

5.2.2 Film Characterization and phosphorescence

It should be mentioned that the experimental study of the phosphorescence consists of two parts (Figure 3.9 and 3.10, which are the measurements of the spectra as a function of the Eu^{3+} concentration and temperature, and the measurements of the decay time of selected transitions as a function of temperature and Eu^{3+} concentratio. For the measurements of the phosphorescence spectra, which were analysed using set-up shown in Figure 3.9, the samples were excited by a pulsed Nd:YAG laser emitting at 355 nm, with a pulse duration of about 5 ns and a repetition rate of 10 Hz. The emitted light was expanded by a planconcave lens to a sufficiently large sample area, and then collected behind the sample by a microscopic lens. The subsequent light was focussed into the entrance of a spectrometer equipped with a CCD camera for signal collection. The set-up used for the decay-time measurements is nearly identical to the equipment described before (see also Figure 3.10). The only difference between the two set-ups is the samples was mounted on an electrical heater so that its temperature could be controlled between 25°C and more than 400°C and the signal detection unit. The light emitted and the light scattered from the sample were focused onto a photomultiplier (PM). A long-pass filter with a cut-off wavelength of 355 nm was placed in front of the PM to reduce the intensity of the excitation wavelength. The time–resolved PM signal was acquired with a high –speed oscilloscope, triggered by the laser. The time dependence of the phosphorescence was analyzed for sample temperature between 25°C and 400°C.

5.2.3 Results and discussion

5.2.3.1 Structural properties

The results of the XRD analyses are summarized in Figures. 5.3a and 5.3b.

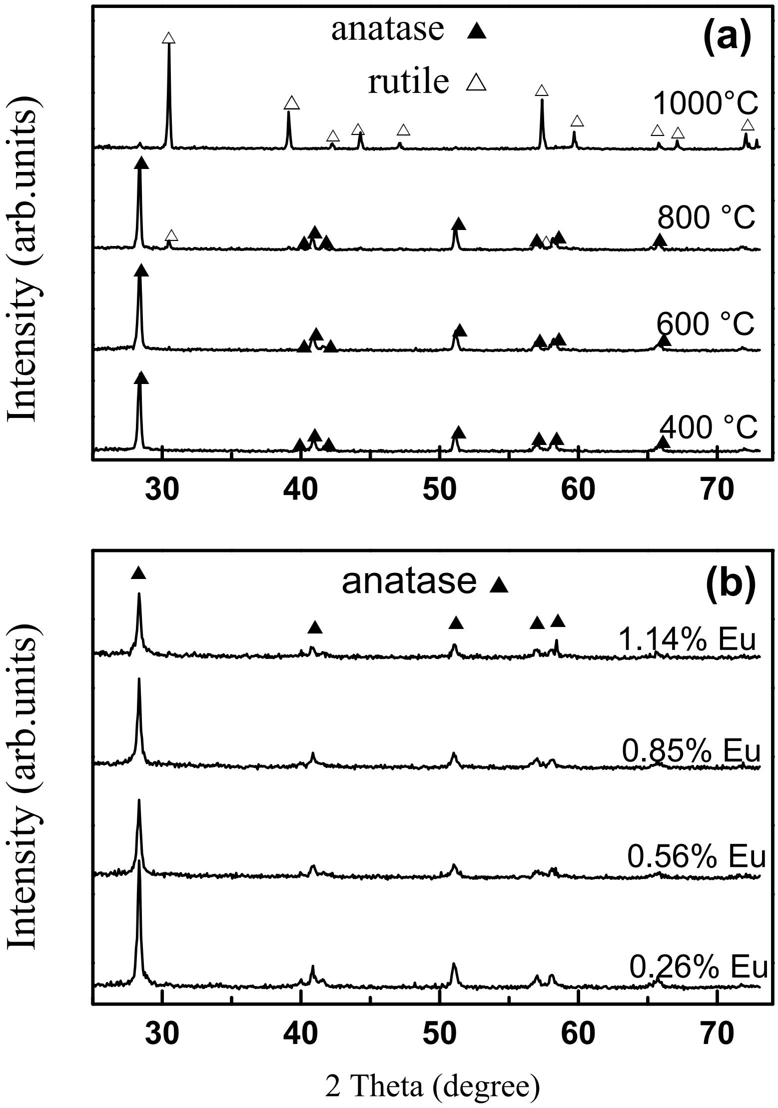

Figure 5.3: XRD patterns of (a) undoped TiO_2 annealed at different temperatures, and (b) europium (III) doped TiO_2films which were annealed to 500°C.

First, the crystallization behavior of undoped TiO_2 films was studied: Films were prepared by dip-coating the substrates at room temperature and using a $Eu(acac)_3$ free sol. Subsequently, the samples were dried and annealed in an oxygen atmosphere at various temperatures (400°C-1000°C) until crystallization occured (annealing time:

2 hours, heating-/cooling-rate 10°C/min). Typical XRD-patterns of the so prepared films are shown in Figure 5.3a as a function of the annealing temperature. Below 400°C (not shown in Figure 2a), no reflections are observed, indicating that these films are amorphous. The films become crystalline at 400°C; the XRD-patterns of such films show the reflections of anatase. Up to annealing temperatures of 600°C, the XRD patterns of the films contain only the reflections of anatase, while above 600°C also the reflections of rutile are observed; obviously a phase change occurs in the temperature range between 600 and 1000°C: The phase change is completed for samples annealed at 1000°C, while samples annealed for two hours at temperatures between 600°C and 1000°C consist of mixtures of the two phases. This result is in agreement with the results of Legrand-Buscema et al.[175]. In the following experiments an annealing temperature of 500°C was chosen for the preparation of europium doped anatase films. In order to study the influence of the Eu-doping on the crystal structure, differently doped $TiO_2 : Eu^{3+}$ films were prepared by dip-coating the samples at room temperature and subsequent annealing for 2 h in oxygen. Figure 5.3b illustrates the XRD patterns of these films. Throughout the anatase phase is formed independent of the doping concentration between 0.26 to 1.14 %.

5.2.3.2 Chemical composition

Figure 5.4 shows the EDX spectra of un-doped and Eu doped TiO_2 films. The spectrum contains major peaks of titanium (Ti) and oxygen (O) which suggest that the films are TiO_2 . The Eu peaks in the spectra of doped TiO_2 films confirming the presence of europium dopant in the film.

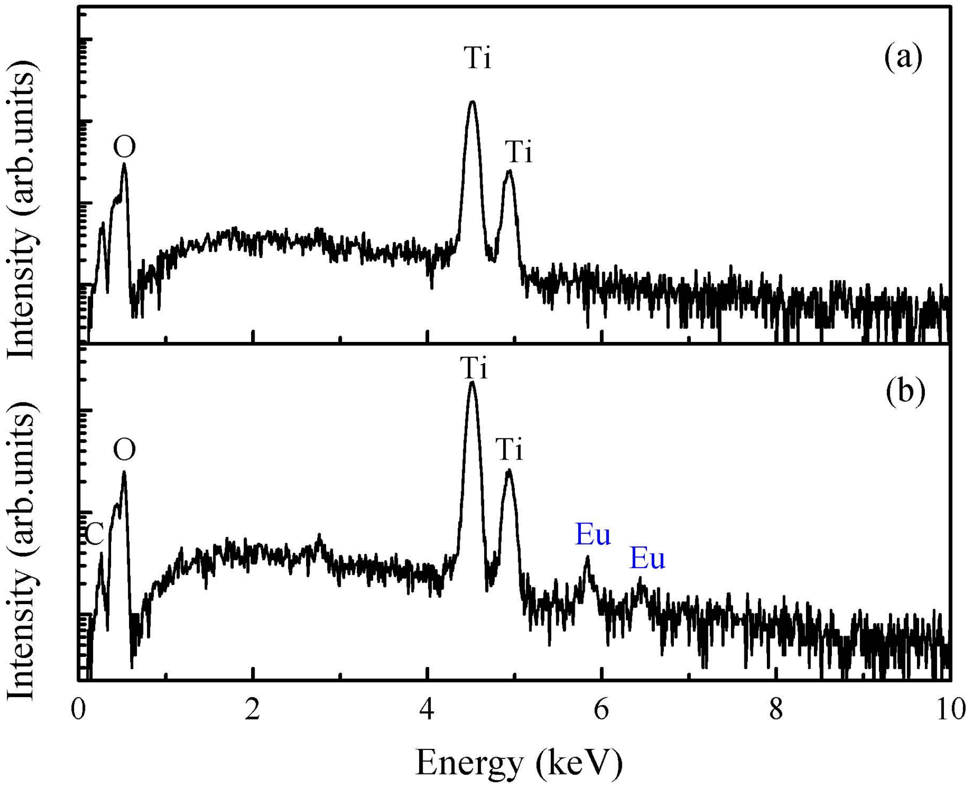

Figure 5.4: The typical EDX spectra of (a) un-doped and (b) Eu-doped TiO_2-film prepared using dip coating technique

5.2.3.3 Temperature- dependent luminescence

Spectral Phosphorescence analysis The phosphorescence emission spectra of thin TiO_2-films doped with different concentrations of $Eu^{3+}$are shown in Figure 5.5.The thicknesses of all samples were nearly equal, around 2 µm, which allows the comparison of the dopant concentration dependence of the phosphorescence intensity. It should be mentioned that attempts were made with europium doped rutile TiO_2-films but they showed no phosphorescence. Moreover, the brookite phase in TiO_2-films was not obtained experimentally. Therefore, only the phosphorescence data of $Eu-$doped anatase TiO_2-films were investigated. These spectra were recorded at room temperature by using unchanged parameters (amplification, laser intensity, etc.). The spectrum consists of emissions mainly located in the red spectral region (from 595 to 720 nm), corresponding to transitions from the excited state to (where J = 1, 2, 3, 4) to the level of $4f^6$ configuration of Eu^{3+}[176, 177]. The emission wavelengths are presented in the table 5.1. The dominant emission peak is situated at 617 nm. This red emission can be assigned to the $^5D_0 \longrightarrow ^7F_2$ transition, which is defined as electric dipole transition, and exhibits stronger intensity than the intensity of $^5D_0 \longrightarrow ^7F_1$ magnetic dipole transition.

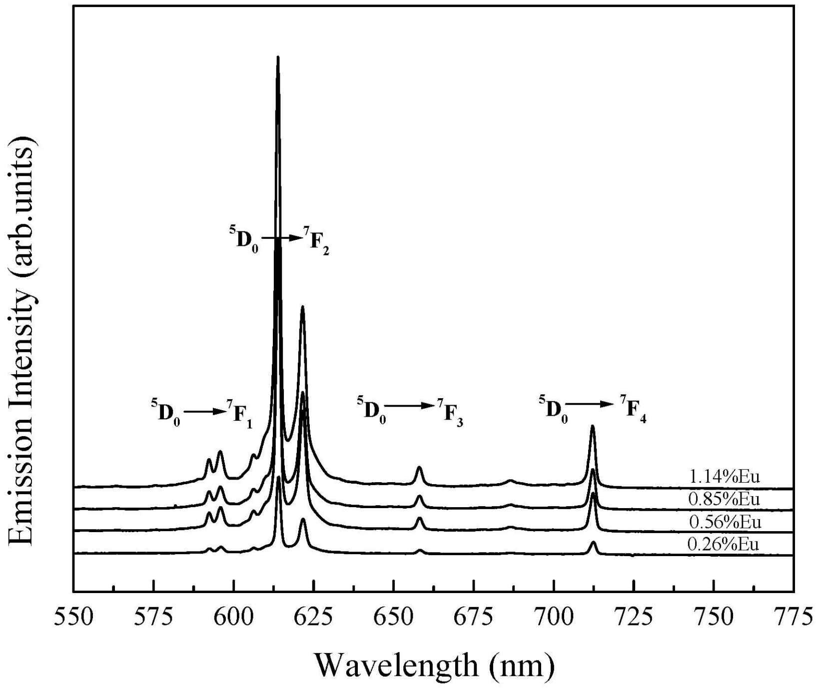

Figure 5.5: Emission spectra of differently doped TiO_2 : Eu^{3+}films at room temperature. The emission spectra were recorded following 355 nm excitation.

One can further observe that the phosphorescence intensity increases with europium concentration. The highest relative emission intensity from the transition (was obtained from the sample doped with 1.14 % of Eu^{3+}. This change in the intensity has been visualized by integrating the area under the curve from 601 nm to 651 nm. This variation in phosphorescence intensity has been studies up to a dopant concentration of 1. 14 %. It is normally believed that more concentration of doping can change the structure of the host material [89]. Hence, the value of concentration was limited within ~1 %.

The relative intensities of the $^5D_0 \longrightarrow ^7 F_2$ transition for all samples with different Eu^{3+}content are displayed in the Figure 5.6. Each data point is the average of three equally doped samples; the error bars display the standard deviation. The error bar for the film with europium concentration 0.56 % is relatively larger than others. This maybe due to enhanced defects in the films or due to non-uniformity in the films thickness. It can be seen that the intensity is steadily increasing with increasing europium concentration. The most promising candidate for surface temperature measurement are the highest doped anatase films due to the high phosphorescence intensity.

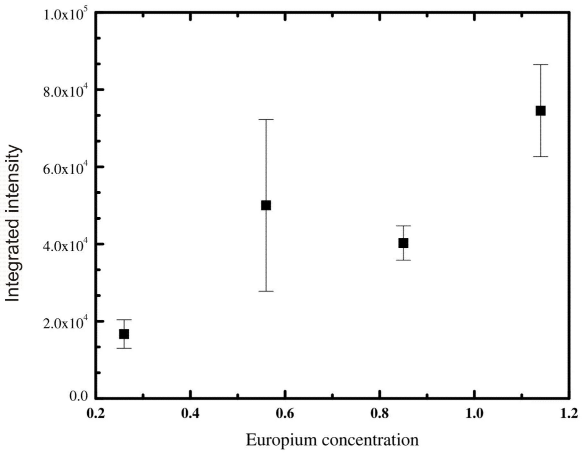

Figure 5.6: The integrated intensity of the$^5D_0 \longrightarrow ^7 F_2$ transition, which was calculated by integrating the spectra from 601 nm to 651 nm.

Table 5.1: Observated emission wavelengths (nm) for (J=1, 2, 3, 4) transition TiO_2 : Eu^{3+}(0.26-1.14 %) at room temperature.

Observed wavelength $[nm]$	wave number $[cm^{-1}]$	Transitions	References
596,599	16778,16694	$^5D_0 \rightarrow ^7 F_1$	[176, 177]
609,617,624	16420,16207,16026	$^5D_0 \rightarrow ^7 F_2$	[176, 177]
660	15151	$^5D_0 \rightarrow ^7 F_3$	[176, 177]
712	14045	$^5D_0 \rightarrow ^7 F_4$	[176, 177]

Time-dependent measurement of the luminescence signal In the current studies the surface is coated with europium doped titanium dioxide as thermographic phosphor. This thermographic phosphor can be used to determine the surface temperature. By measuring and evaluating the luminescence signal. In the following, the temperature dependent decay lifetime of the phosphor and the total phosphorescence intensity are evaluated.

Decay time analysis The phosphorescence lifetime is relatively easy to measure and also independent from other parameters, except temperature. Thus, for many applications it is the most promising property for surface temperature measurements from thermographic phosphors. Figure 5.7 shows the typical results of the phosphorescence decay for a sample doped with 0.85 % Eu^{3+} at three different temperatures, 85°C, 260°C, and 335°C. The intensities are plotted on a linear scale (Figure 5.7a) and on a logarithmic scale (Figure 5.7b); the plotted curves are averages of 200 pulses. The offset of the phosphorescence intensity was eliminated by subtracting the averaged signal prior to the laser pulse and thus the baseline of the signal intensities is zero. At first sight, it seems that the phosphorescence intensities decrease exponentially with time (see Figures. 5.7a and 5.7b); thus, a single-exponential fit would be best for the evaluation decay time

$$I\left(t\right) = I_0 \exp\left(\frac{-t}{\tau}\right) \tag{5.1}$$

$I\left(t\right)$ is the intensity of the decaying phosphorescence signal at time$t$, I_0 the initial intensity at $t = 0$, and τ is the lifetime of the excited states. Nevertheless, having a closer look on Figure 5.7b one observes that the curves are not exactly straight on the logarithmic scale, but slightly curved. Although such phenomena were already observed in the literature for several thermographic phosphors (see e.g. reference [177], no simple theoretical explanation exists. Further, it makes it difficult to precisely fit the curves in Figure 5.7 by equation 5.1, because the resulting lifetimes τ also depend on the time interval used for the fitting process. This would lead to (slightly) different lifetimes for each measurement (temperature), which is not acceptable for a precise temperature evaluation. However, recently Brübach et al [83]. showed an empirical way how to proceed with such curves: they developed a fitting routine, which is baseed on the use of equation 5.1, but varies the time interval until a sufficiently wide range of the measured curve is described precisely by this equation (for details see Ref. [83]). Brübach algorithm is discussed chapter 2 (section 2.2.3.2). This algorithm was applied for fitting the temporal variation of Phosphorescence intensities of a $TiO_2 : Eu^{3+}$ film. The initial parameters for the routine were c1=0.2, and c2=1.75 [83]. According to these fits the lifetimes τ are 214 µs at 85 °C, 166 µs at 260°C, and 49 µs at 335 °C, showing a strong lifetime dependence with increasing temperature.

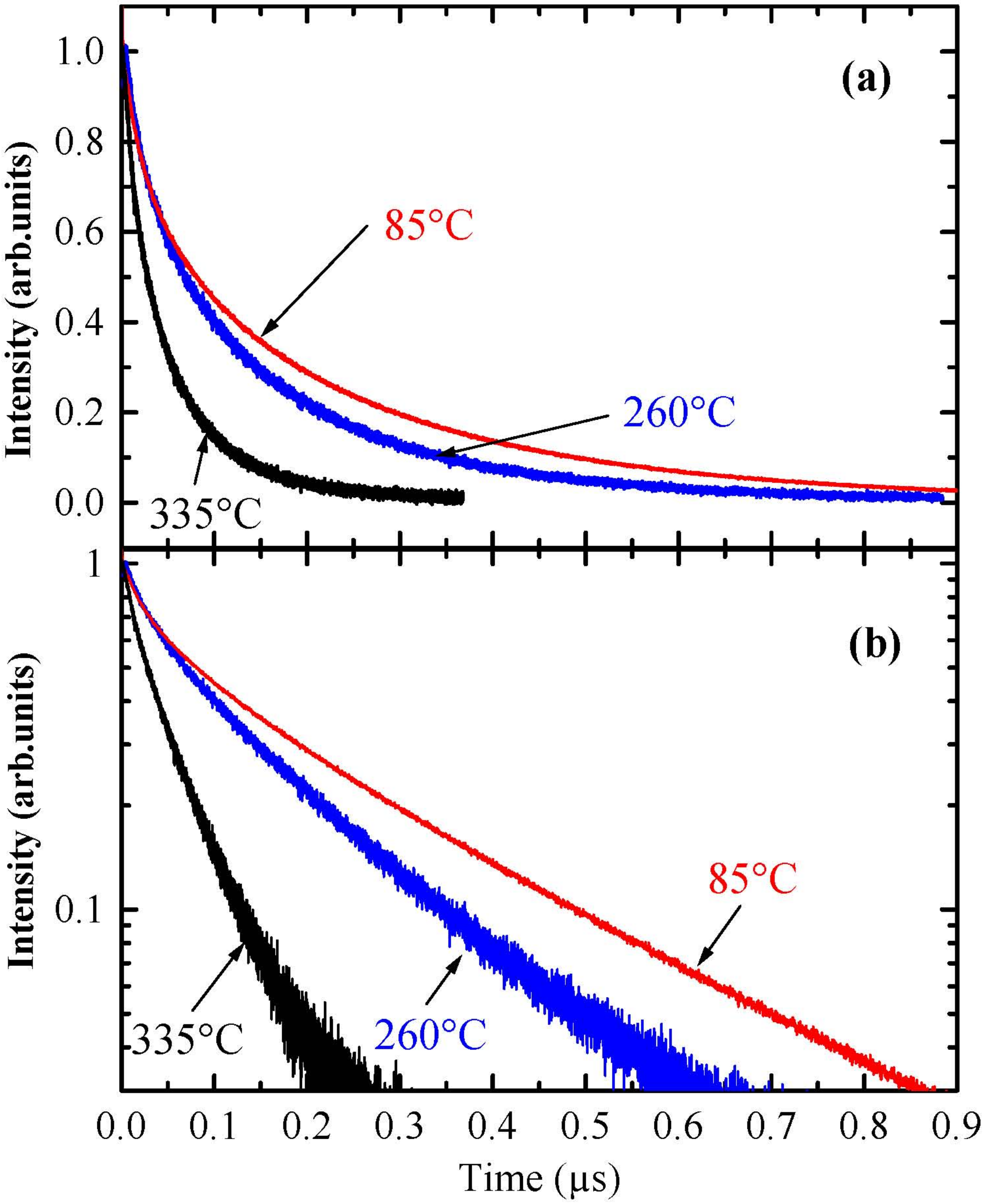

Figure 5.7: Phosphorescence intensities of a $TiO_2 : Eu^{3+}$ film (0.85% Eu^{3+}) following an excitation pulse of 355 nm wavelength and 5 ns duration. The phosphorescence intensities were recorded as a function of time at film temperatures of T=85°C, 260°C, and 335 °C,

For a more detailed luminescence analysis, TiO_2-films doped within 0.85 % europium were selected. This is because the integral intensity of phosphorescence signals is significant and are comparatively more repeatable than other concentrations (see Figure5.6). Several europium doped TiO_2-films (0.85 % Eu^{3+}) were slowly heated until a steady-state temperature was reached, then the decay time was measured, and subsequently the curves were fitted. The lifetimes values obtained from these fits are plotted in Figure 5.8 as a function of the sample temperature: it shows the results of the lifetime decay characteristics of a prominent emission line from $TiO_2 : Eu^{3+}$, at (617 ± 15) nm. The lifetime versus temperature is plotted on a semi-logarithmic scale for three identically doped samples (0.85 % Eu^{3+}). Thereby, each data point is the average lifetime of the three samples and the errors are the standard deviations. It is seen that the lifetime is nearly constant between room temperature and 200°C, around 220 µs, while above 200°C the lifetime decreases strongly with temperature, presumably due to quenching. At 350°C lifetime becomes 35 µs. Thus, temperatures between 200°C and 350°C may be evaluated from lifetime measurements, due to the sufficiently high slope of the curve. At lower temperatures the temperature cannot be well deduced from the obtained lifetime, the slope being quite small. The general function used for calculating temperature from lifetime measurements is [178, 173],

$$\mathrm{Ln}(\tau) = \mathrm{a}\text{-}\mathrm{bT}$$

where (a) is constant, and (b) is the first order coefficient, However, the fitting of our experimental lifetime data based on the above equation show larger deviation. As such, attempts were made to fit these data using higher order empirical function. It was observed that our experimental lifetime data fitted well with a fourth order empirical function, which is

$$ln\left((\tau)\right) = -5.0061 - 0.0732.T + 5.4573.10^{-4}.T^2 - 1.6385.10^{-6}.T^3 + 1.5840.10^{-9}.T^4 \tag{5.2}$$

where T is in °C. The empirical function was fitted to the curve for 200°C $<$ T $<$ 400°C. This function can be used for calculating the temperature from lifetime measurements.

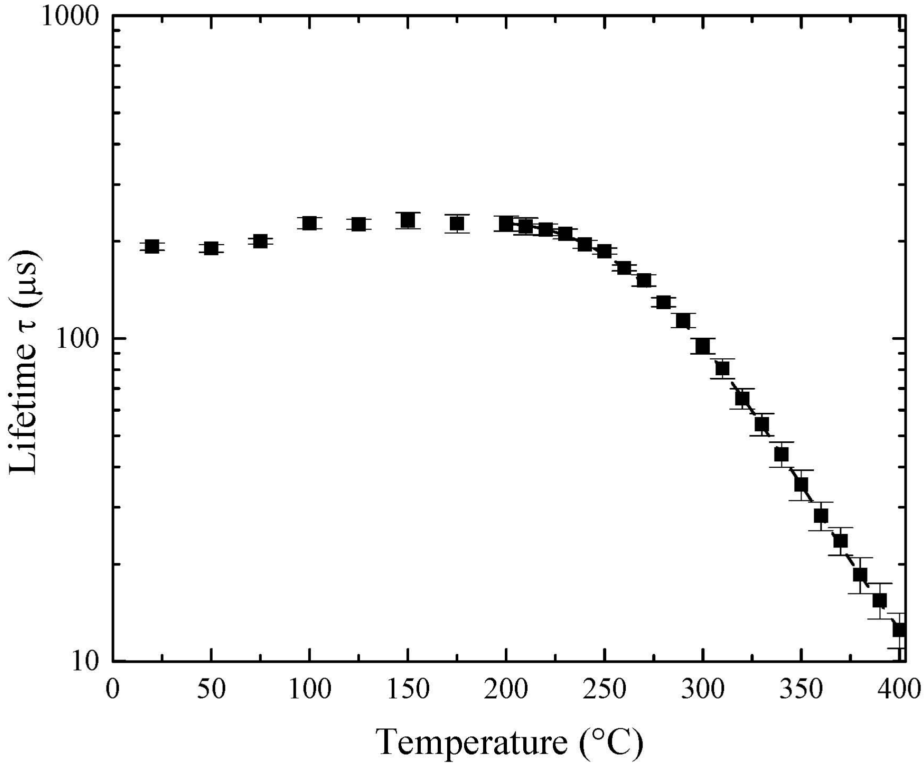

Figure 5.8: Decay lifetimes characteristics as a function of temperature of TiO_2 : Eu^{3+} (0.85 %) at 617 nm under 355 nm excitation. The plotted data are the averages of three different measurements, which were performed on three equally doped samples. The errors are the standard deviations. The dashed curve is an empirical fit to the data points between 200° and 400 ° (equation 2).

The phosphorescence lifetime was also studied as a function of the europium concentration: the lifetimes were measured at 20° for eight different dopant concentrations

Figure 5.9. Each data point plotted in Figure 5.9 is the average of two single measurements of two equally doped samples, respectively. The errors are the standard deviations. It is easily seen that the lifetimes are slightly depending on the europium concentration $C_{Eu^{3+}}$; the lifetime is decreasing rather linear with increasing europium content. A linear function was fitted to the curve for 0.26 % $< C_{Eu^{3+}} <$ 1.14 %, which is:

$$\tau\,(s) = 2.765.10^{-4} - 8.821710^{-5} C_{Eu^{3+}}\,(\%)$$

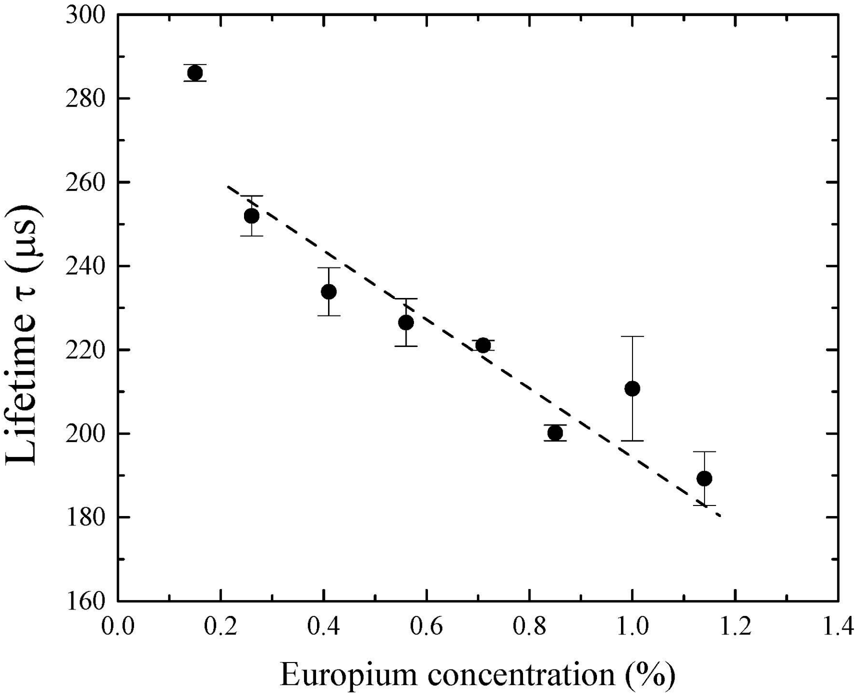

Figure 5.9: Decay lifetimes measured at 20°C as a function of the europium concentration within the films. Each data point is the average of two different measurements, which were performed on two equally doped samples. The errors are the standard deviations. The dashed curve is an empirical linear fit to the data points between 0.26 % and 1.14 % Eu^{3+}5.2.3.3

Phosphorescence intensity analysis. For several samples doped with 1.14 % Eu^{3+} the spectra were measured as a function of temperature Figure5.10. It was found that the phosphorescence intensity decreases with increasing temperature. At around 350 °C the phosphorescence signal drops below the noise of the used CCD-camera. Also the position of the $^5D_0 \longrightarrow ^7F_2$ transition was studied as a function of temperature. However, no significant change of the peak position was observed while heating the samples from room temperature up to 300 °C; the shift of the maximum is less than 1.0 nm as checked experimentally. Due to the small shift, the spectral analysis of the samples is not promising for temperature evaluation. Such studies would need a high precision spectrometer, which is not very economical.

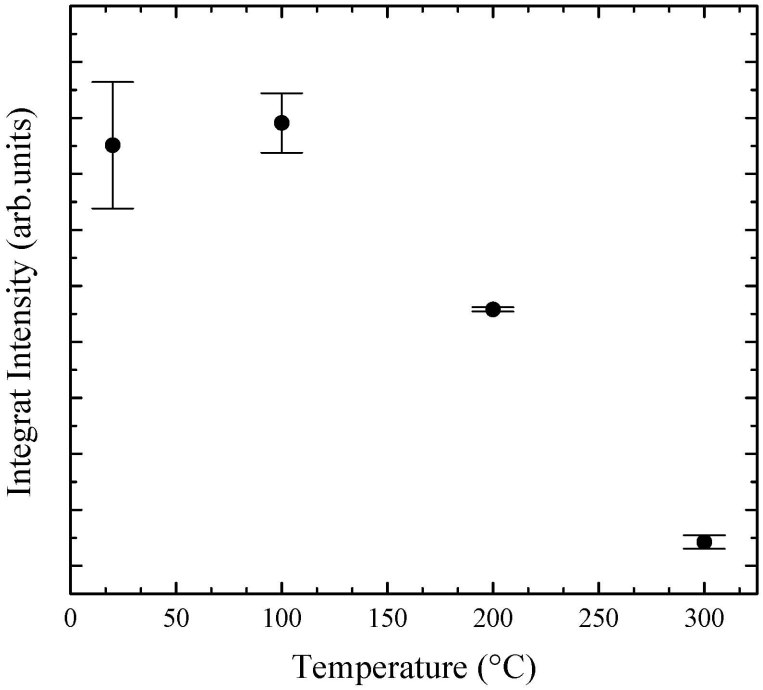

Figure 5.10: The highest relative emission integrate intensity from the transition $^5D_0 \rightarrow ^7F_2$ (was obtained from the sample doped with 1.14 % of Eu^{3+}) as function of temperature

5.2.4 Conclusion

Europium (III)-doped titanium dioxide thin films have been prepared by a dip-coating method to be used as a thermographic phosphors coating. Depending on the annealing temperature europium doped anatase and rutile films, as also mixtures of these two phases were obtained. The focus of the present study was the luminescence analyses of Eu^{3+} doped anatase because Eu^{3+} doped rutile shows no phosphorescence as checked experimentally. The important results of the present study are the following:

- Europium-doped anatase is a suitable phosphor for temperature measurements as reproducible phosphorescence is observed.

- Using 355-nm excitation, the $^5D_0 \rightarrow ^7F_2$ transition was much stronger than the $^5D_0 \rightarrow ^7F_1$ transition, which makes it preferable for the temperature dependent analysis.

- The phosphorescence intensity is already sufficiently high for low europium concentrations (typically 0.26-1.14%). This is important for the development of cheap coatings as the rare earth elements are usually relative expensive compounds.

- The temperature dependency of the phosphorescence lifetime is reproducible for different films and slightly dependent on the europium concentration within the analysed range (0.26-1.14 % Eu^{3+}). As shown for the concentration of 0.85 % Eu^{3+},the lifetime changes sufficiently in the range from 200°C up to 450 °C, presumably due to quenching. Thus, the temperature evaluation from lifetime is possible within this temperature range.

Finally it should be mentioned that the TiO_2 films were also doped with further elements, namely Cr, Dy, and Tm. No phosphorescence was observed for any of these dopants, indicating that these dopants in TiO_2 are not useful for thermographic phosphor application.

5.3 Thermal oxidation of titanium deposited by cathodic vacuum arc (CVA)

As seen in the previous section, the anatase phase of titanium dioxide can be used as a temperature sensor, whereas the rutile phase showed no phosphorescence. For that reason the rutile phase of titanium dioxide was investigated as a protective coating material. Rutile-TiO_2possesses low friction, good wear resistance, good corrosion resistance, and good biocompatibility [34, 35]. In order to deposit rutile phase using techniques like CVD, magnetron sputtering, sol gel, etc., high temperature is needed. But due to lattice mismatch and thermal expansion mismatch between rutile phase and stainless steel substrate, rutile films can not be deposited with good adhesion on stainless steel substrates [179]. However a layered film structure, comprising of rutile phase as top layer with a diffuse Ti layer at the bottom showed good adhesion with stainless steel substrate. This layered film structure can be obtained by thermal oxidation of titanium films to rutile phase [180]. Krishna et al [180] reported such layered films over stainless steel by magnetron sputtering. They found such films show good adhesion with stainless steel substrate, and enhance the surface hardness and triobolgical properties of stainless steel. In the present work, similar layered films were developed by thermal oxidation of titanium films deposited using CVA technique. Cathodic vacuum arc has been chosen for developing titanium films as the deposition rate is much high [66]. Hence, it is promising for mass production

5.3.1 Experimental procedures

The preparation of titanium films with rutile-TiO_2 layer at the top was carried out in two steps: the deposition of titanium by means of cathodic vacuum arc (CVA) followed by a thermal oxidation technique, as explained in the following.

5.3.1.1 Deposition of titanium on stainless steel substrate

Titanium coatings were deposited by a cathodic vacuum arc (CVA) method. All technical details are given in chapters 2 and 3 of this thesis. Technical details of the used deposition (CVA) set-up are reported in the chapter experimental setup Figure 3.6. The titanium with purity grade 2 (Ti(99.3%)) was used as the cathode source. Coatings were performed in the presence of argon gas (99, 99 % purity). Inside the chamber, the position of sample holder is fixed in front of the source and the distance between these objects was maintained at around 55 cm. All coatings were deposited on stainless steel substrates (AISI 304) sized 2cm x 3cm); substrates were cleaned in an ultrasonic bath with acetone for 10-15 minutes. For the measurement of the deposited weight on the substrate all bare substrates were weighed before and after depositions. From the change in the mass the thickness of the films were calculated by using the density of bulk titanium. The following describes the typical process for titanium coating by CVA. Initially the substrate was cleaned by argon plasma at 10^{-2} mbar and a negative bias voltage of 1000 Volt for 10 min. During the deposition of titanium, voltage and current were kept constant at 20 Volt and 80 amperes simultaneously. All deposition coatings were carried out at 10^{-3} mbar pressure.

5.3.1.2 Thermal oxidation of titanium coating

After the deposition of titanium from CVA the samples were oxidized by keeping them in a furnace in an oxygen atmosphere (oxygen flow of 200 sccm) at various temperatures ranging from 400°C to 700°C for periods of 1-7 h. After oxidation treatment, the samples were removed from the furnace and allowed to cool in air. The heating and the cooling rate was 10°C/min.

5.3.1.3 Cavitation erosion test experiments

Cavitation erosion experiments were performed to estimate the relative adherence. A schematic diagram of the cavitation test is shown and described in Figure 3.12. The cavitation erosion tests of the thermally oxidized titanium films were done in accordance with ASTM G32- 98 standard [118]. As mentioned in Figure 3.12, the main parts of the cavitation test composed of an ultrasound generator, a sonotrode with titanium tip, and a tank filled with de-ionized water which was used as the testing environment. Before the beginning of the test, the samples were cleaned and weighed. The lower end of the sonotrode was immersed 10 mm deep into a tank of the test liquid that is maintained at 20°C and ambient pressure for all experiments. The sonotrode is vibrating at 20 kHz. Peak-to peak displacement amplitude of 5 µm was used as is proposed in the ASTM standard. During the cavitation test, the high frequency vibration of the sonotrode produces a cavitation bubble field in front of the sample surface, which is originated by the pressure fluctuation at the tip of the sonotrode. Consequently, micro jets are induced by the imploding bubbles. They hit the surface, and, after a certain time, damage it. The weight of the sample is noted after it has been thoroughly dried, then returned to the tank for additional processing and again weighted. This test/interruption cycle is repeated in order to obtain a history of mass loss versus time. Finally, the behaviour of the plot mass loss versus erosion time was used to characterize the degree of erosion.

5.3.2 Results and discussion

5.3.2.1 Film structure

Figure 5.11 shows the X-ray diffraction patterns generated from three typical samples: uncoated steel substrate, steel substrate coated with titanium film and Ti coated steel substrate after oxidation at 620°C for 7 h. A Bruker D8 Advance X-ray spectrometer equipped with a grazing incidence optic was used. As a reference, the XRD pattern of the clean substrate is also presented in Figure 5.11: four diffraction peaks can be observed, reflecting the typical structure of stainless steel [181, 182]. After 20 min of titanium deposition by cathodic arc vacuum technique, film thickness of $\sim$ 1 µm was achieved. The XRD pattern changed: the reflection peaks of titanium were observed, which are identical to the standard pattern of bulk Ti. However, the reflections of the substrate are still visible. Moreover, no preferred orientation was observed in the titanium coating produced under these conditions m. However, the film changes after thermal oxidation. Several titanium films were oxidized for different periods (1, 3, 5, and 7 hours) and subsequently analysed by XRD. The appearance of peaks corresponding to the rutile phase in the diffraction pattern of 7 h oxidation suggests formation of the rutile phase over the Ti film. XRD pattern shows that rutile-TiO_2 also posses a random orientation as Ti films, and becomes the major phase after oxidation. The Ti peak intensity reduces drastically. In addition, no anatase phase was observed in all the oxidised samples see Figure (5.11c). Oxidation at such higher temperature in O_2environment facilitate the conversion of Ti films to rutile-TiO_2[183]

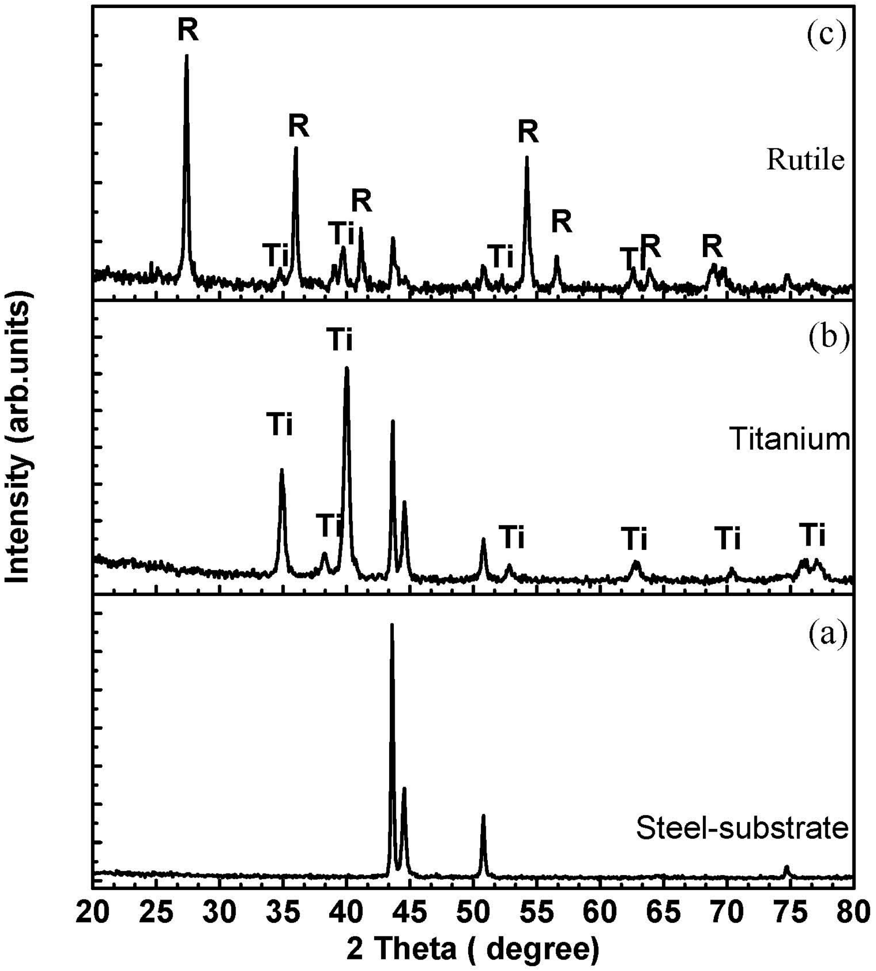

Figure 5.11: patterns of (a) a clean stainless steel substrate , (b) Titanium film, and (c) rutile films which were oxidized at 620°C in O_2 for 7h.

5.3.2.2 Chemical composition and surface morphology

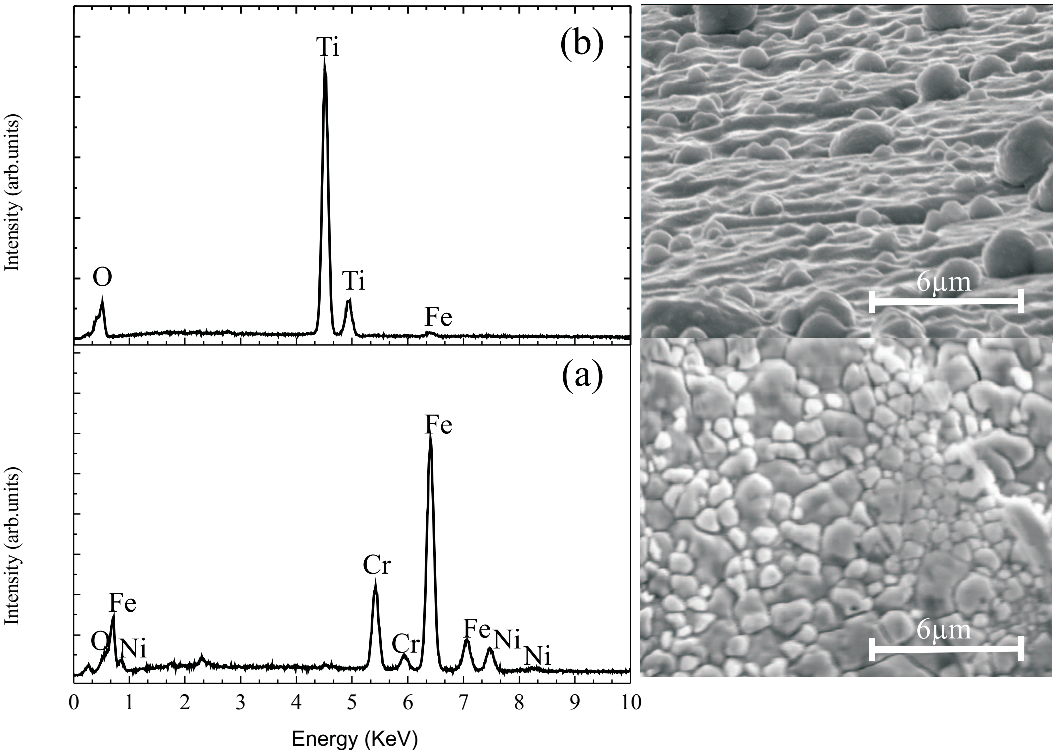

Figure 5.12: SEM images and EDX spectras (a) clean stainless steel substrate.(b) oxidized titanium coating (after oxidation at 620 °C for 7 h under oxygen atmosphere).

Figure 5.12 b shows the EDX- spectrum of a ~ 1 µm thick film, which was deposited within 20 min and oxidised at 620 °C. As a reference, the EDX-spectrum of the clean substrate is also presented in Figure 5.12 a. It reveals the typical spectrum of stainless steel [181, 5]. The spectrum of the film in Figure 5.12 b clearly differs from the spectrum of the substrate: all peaks of the substrate have completely disappeared due to shielding produced by the covering film. Furthermore, peaks of titanium and oxygen appear, indicating formation of titanium dioxide over Ti film. In order to support the EDX analysis of both surfaces, clean substrates and oxidised titanium films were also investigates by SEM see Figure 5.12 (a, and b). As right a reference, an image of the clean substrate is shown in Figure5.12a. Both images show the top view of the samples. However, before the deposition of titanium by CVA and the oxidation process, the clean stainless steel has a shining silver coloured surface and small islands were observed which are separated by small trenches of 1-2 µm depth [5]. After formation of TiO_2 the colour of the substrate changed: green coloured areas are seen and the trenches between the islands have nearly disappeared, indicating also the covering film.

5.3.2.3 Cavitation erosion test

In order to investigate the adhesion properties of the oxidized Ti films on the steel substrate, which have an influence on cavitation resistance, the incubation time and the maximum erosion rate have been measured for both the uncoated steel and Ti coated steel with rutile-TiO_2 layer at the top. Figure 5.13 shows the mass loss for the uncoated steel substrate and the rutile covered steel versus time. For the uncoated steel substrate, the incubation time of steel is around 90 min (area I). Further, the maximum erosion rate can be deduced from the slope of the mass loss (area II); it is around 6.37 mg/min. The endurance of the Ti coated steel with rutile-TiO_2 layer at the top against the cavitation erosion differs from the uncoated steel. Within the first 60 min of cavitation, the mass loss of the coated sample is very slightly higher than that of the uncoated sample. With increasing cavitation time the mass loss of the uncoated sample rises rapidly, whereas the mass loss rate of the rutile covered samples remains relatively constant. Consequently, the difference in mass loss between the coated and uncoated steel strongly increases. The incubation time is nearly the same for the coated and the uncoated steel. For the last four points of Figure 5.13 the maximum erosion rate for the coated sample is calculated from the slope to be 0.932 mg/min, considerably less than for the uncoated steel. Overall, the total mass loss of the thermally oxidized samples of Ti coated steel is around 3.5 times lower than that of the uncoated sample; this is quite a promising result. Finally, it should be noted that each data point is the average of three different measurements, which were performed on three equally prepared samples and the error bars are the standard deviations.

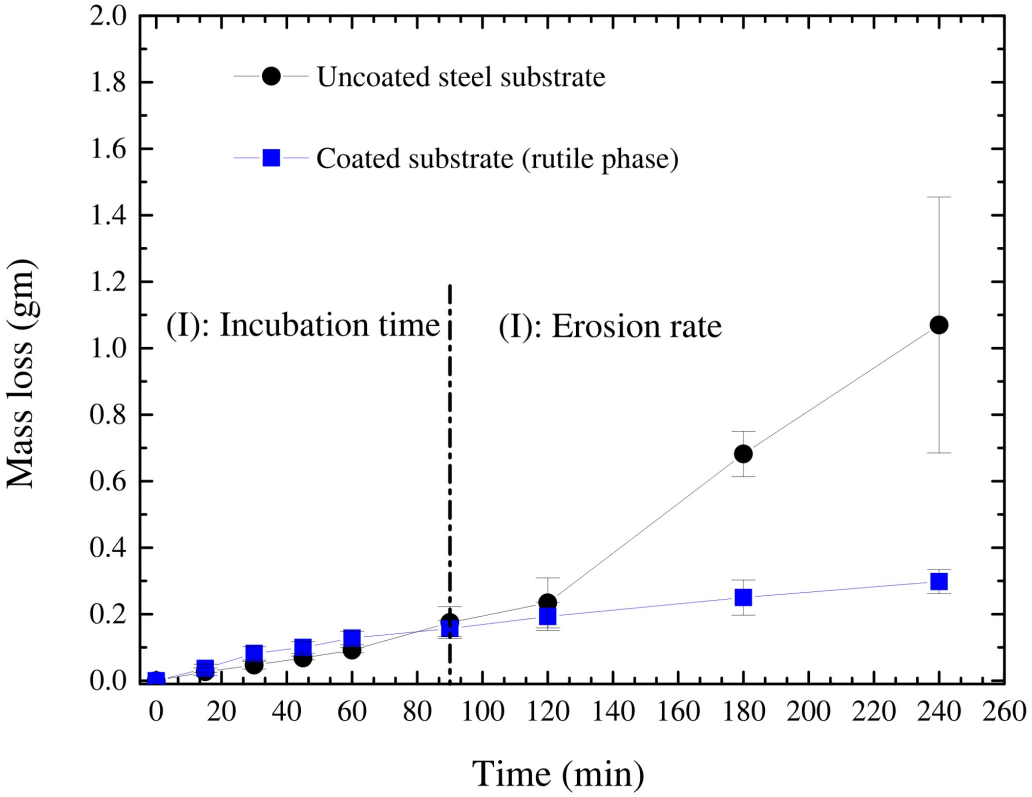

Figure 5.13: The variation of the mass loss versus attack time for uncoated steel and rutile coated steel . Each data point is the average of three cavitation test measurements.

SEM analysis The surface morphologies of the samples were also investigated by SEM in order to judge the cavitation damages visually. The uncoated steel was analysed before the cavitation test see Figure (5.14 a), after 30 min attack time Figure (5.14 b), and after 240 min attack time Figure (5.14 c). This analysis shows that, the beginning of the catitasion erosion starts slightly earlier before 30 min, which was also deduced from the mass loss calculations. After 30 min of the cavitation test, the surface of the uncoated steel shows obvious signs of the attack, as can be seen in Figure5.14(a, b). Whilst, the uncovered steel shows the typical grain structure of steel with flat islands of 10 µm diameter, before the cavitation test, several sharp-edged holes of around 2 µm diameter can be seen afterwards (see figure 5.14 b). As expected, the cavitation test damages become stronger after further cavitation, see Figure (5.14 c), when the grain structure of the steel is completely destroyed.

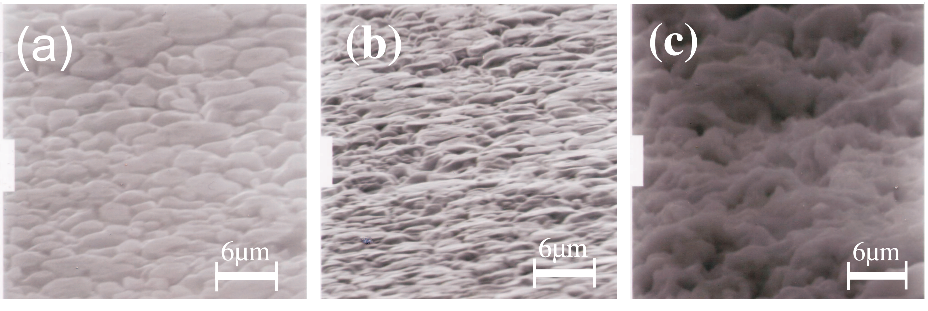

Figure 5.14: SEM images of an uncoated steel substrate (a-c) taken during cavitation erosion. (a) meaured before the cavitation erosion test, (b) measured after 30 min, (c) measured after 240 min.

Similary, the Ti coated steel with rutile-TiO_2 layer at the top was also analysed by SEM before the erosion test Figure (5.15a), after 30 min attack time Figure (5.15b), and after 240 min attack time Figure(5.15 c), in the left images the scale bar is 20 µm, in the right images the scale bar is 6 µm. After 30 min cavitation the surface of the coated sample figure (5.15b) is practically unchanged in comparison to its initial surface morphology Figure (5.15a). Here, in contrast to the uncoated steel, no grain structure of the steel is observed to compare the surface morphology, because they are already filled with the rutile coating. After 240 min cavitation figure 5.15 c the surface morphology of the rutile covered steel is changed in comparison to the sample subjected to the cavitation for 30 min and uncavitated sample surface morphologies (Figures 5.15a b). As expected, although the rutile covered steel was subjected to cavitation test for 240 min, no grain structure from the steel was observed thisprovides evidence that the coating remains. After 240 min attack time, the uncoated steel surface is highly damaged, while for the rutile covered sample the cavitation affects only the coating. The presented cavitation erosion experiments have shown that the rutile film is well adhering to the steel substrate. It is further show that the coating is improving the resistance of steel against intensive erosion. As a result, Ti coated steel with rutile-TiO_2 layer at the top offers a good protection for the steel, which should make it interesting for industrial application.

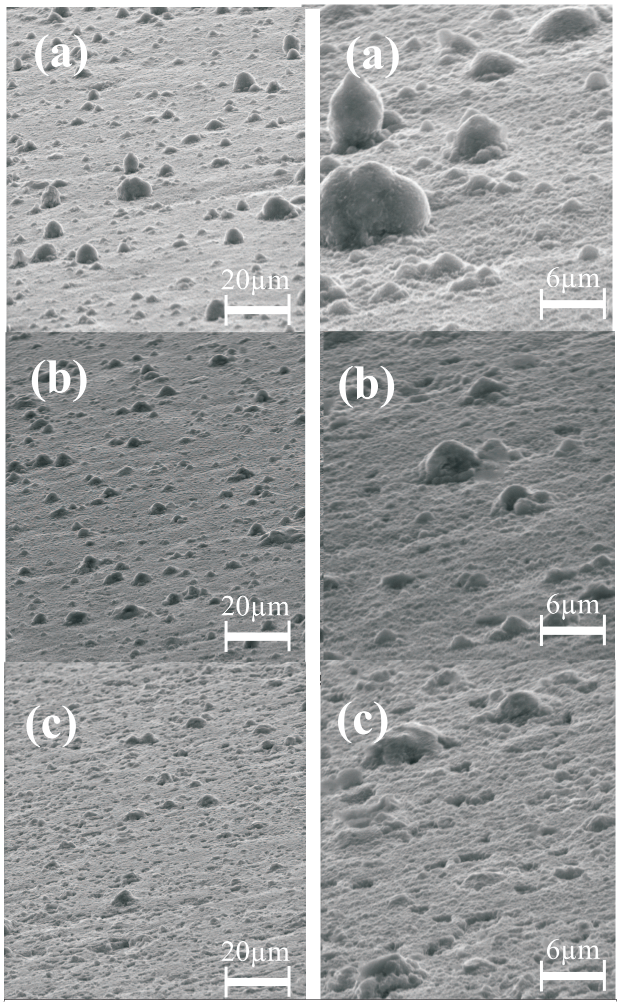

Figure 5.15: SEM images of rutile coated steel substrates, which were measured during cavitation erosion. (a) measured before the cavitation erosion test, (b) measured after 30 min, (c) measured after 240 min: left images the scale bar is 20 µm, right images the scale bar is 6 µm

5.3.2.4 Summary

The possibility of preparing crystalline titanium dioxide TiO_2 rutile phase on stainless steel substrate has been shown by the thermal oxidation of titanium. The titanium films were deposited by cathodic vacuum arc (CVA) and were thermally oxidized to grow rutile-TiO_2 phase at the top. With XRD and EDX analysis it was shown that the top layer of titanium films convert to rutile phase after 7 hours oxidation under O_2 atmosphere at 620°C. Cavitation erosion tests confirm that rutile-TiO_2 with a Ti inner layer is a well adhering coating for stainless steel substrate and protects the substrate effectively from erosion. Hence, Ti coated steel with rutile-TiO_2 layer at the top should be of interest for industrial applications.

6 Summary and conclusion

The objective of this research work was to deposit and characterise undoped and doped metal oxide thin films, such as zinc oxide (ZnO) and titanium dioxide TiO_2. The present thesis can be broadly classified into two parts. First part deals with ZnO films while the second part focuses on TiO_2 films. In the first part, un-doped and Al-doped ZnO thin films were deposited by two home built CVD-reactors. Firstly a halogen lamp reactor (HLR), which is a new user-made CVD- reactor activating the deposition process by the light radiation from halogen lamps. It has the advantage of heating the substrate rapidly without the need for a contact substrate heater. Halogen lamps are a convenient, efficient and environmentally clean thermal source. The acetylacetonates of zinc and aluminium were used as precursors in the presence of oxygen. The deposition experiments were performed at substrate temperatures of 400-600°C on silicon and at 450-600°C on borosilicate glass at a total pressure of 200 mbar.

The main results of the present process can be summarized as follows:

- With an accurate selection of deposition conditions it was possible to deposit high quality ZnO films on both substrates; silicon-(100)-oriented and borosilicate glass), where the X-ray diffraction shows only (002) and (004) peaks indicating a strong preferred orientation. Furthermore, the SEM analysis substantiate the observation from the X-ray diffraction.

- Deposition does not take place below 400°C deposition temperature.

- Homogeneous Al-doped ZnO films of 0.2 to 0.5 µm thickness were deposited for the first time from the acetylacetonates of zinc and aluminium using HLR. The films are highly transparent in the visible region.

- The Al-doped ZnO films have a relatively low resistance, around 2.48 $m\Omega cm$. Thus, these films are quite promising for the application as transparent conducting oxides.

- The electrical properties like band gap, which is dependent on the aluminium content, can be easily controlled by varying the gas flows through the evaporators. Precise aluminium doping was possible as proved by EDX.

- The room temperature photoluminescence exhibit two peaks corresponding to the band edge emission of ZnO and to a defect present between valence and conduction bands. The samples with typical aluminum concentration are encouraging to investigate Al-doped ZnO films as temperature sensors in the range of room temperature to 300°C.

- Both acetylacetonates are promising candidates as precursors for the deposition of un-doped and Al-doped ZnO films. They are commercially available, quite cheap, non-toxic and easy to handle, supporting the development of a low-cost industrial deposition process.

The second reactor is a hot wall reactor (HWR), which is a low cost CVD setup again. It was used for the deposition of un-doped and Al doped ZnO films. The deposition was performed on silicon-(100)-oriented and borosilicate glass substrates under atmospheric pressure avoiding the use of an expensive vacuum systems. Acetylacetonates of zinc and aluminum in presence of synthetic air were used as precursors. Both the temperature and distance into the CVD reactor strongly influenced the deposition.

The experimental results showed that at a furnace temperature of 450°C, a homogeneous deposition was achieved in the middle of the reactor. The growth rate of the CVD processes increased with increasing furnace control temperature, and this effect was stronger at 550°C where the growth rate varied along the direction of the gas inlet due to the depletion of the precursor. The profile of the growth rate along the reactor exhibited a pronounced maximum, located around the middle of the isothermal zone. A further increase in the distance resulted in a decrease of the growth rate. This is likely to be due to the temperature profile in the reactor. It was also found that the films thickness increases almost linearly with increasing deposition time. Thus, it is expected that thick films can be produced using the current setup. Analysis of the structure showed that the film growth of ZnO starts at a furnace temperature of 400°C, with polycrystalline behavior. Thus, no annealing process is needed. At 550°C crystalline films can be observed which consist of (002) and (103) reflections indicating a preferred orientation of the ZnO film The un-doped and Al-doped ZnO on glass substrates exhibit optical transparency in the visible range (400-800 nm) over 65 %. The band gap dependent on the aluminum content can be easily controlled by varying the gas flows through the evaporators. Precise aluminum doping was again proved by EDX. According to these results, the hot wall reactor set up would be another possibility to employ a relatively low cost deposition process.

The second part of this thesis was about the preparation and characterisation of undoped and doped titanium dioxide thin films. Based on the applications of titanium dioxide, this part has been splitted into two sections. In the first section, undoped and europium doped TiO_2 films were evaluated as a possible thermographic phosphor. These materials were synthesized by sol-gel method using dip coating technique. While annealing at different temperatures, anatase, rutile and mixed phases of TiO_2 develop as was confirmed by XRD. Luminescence studies revealed that Eu^{3+} doped anatase show reproducible phosphorescence suggesting them as suitable phosphor for temperature measurement. However, such possibilities are ruled out in case of Eu^{3+} doped rutile as it shows no phosphorescence. The phosphorescence intensity was found significantly high even for low europium concentrations. This helps in the development of cheap coatings as thermographic phosphor. The temperature performance in terms of the lifetime decay of the Eu^{3+} doped anatase films were reproducible for different coatings and depend slightly on europium concentration. Europium doped anatase was found suitable for temperature measurement within a range of 200 °C to 450 °C as the lifetime changes sufficiently as well as linearly within this range. In the second section, the rutile phase of titanium dioxide was investigated as protective coatings. Efforts have been made to deposit titanium coatings onto stainless steel by cathodic vacuum arc, and then partially convert the titanium coatings to rutile phase titanium oxide by thermal oxidation. The presence of rutile phase titanium dioxide and titanium metal were confirmed by XRD. Cavitation erosion was used for the first time to investigate the adhesion properties of these coatings. Cavitation erosion tests confirmed that rutile TiO_2 films with a Ti inter layer are well adherent to stainless steel substrates and protect the substrate from erosion. The total mass loss of the thermally oxidized samples of Ti coated stainless steel was found around 3.5 times lower than of the uncoated samples.

Future scope

In the present work, it has been shown that high quality film deposition can be done using HLR while HWR can be used as a cheap means of deposition. These studies were done with respect to only one dopant (Al) and in context to only one application (TCO). Further experiments can be planned to explore the potentials of these two systems in depositing ZnO films and doping them with various others elements such as, Cr, Co, Fe, etc. These dopant are known to modify the electrical, optical and magnetic properties of the host material (ZnO), making it suitable for various new application such as, spintronic devices, P-type semiconductors, etc. Likewise, anatase TiO_2 films dopant with Eu was study for thermographic phosphor applications. The study of thermographic phosphor properties of ZnO doped with others elements such as, Eu, Er, Tm, etc. also seems to be interesting and future experiments can be planned in this direction

Bibliography

[1] A. Elshabini-Riad and F.D. Barlow. *Thin film technology handbook*. McGraw-Hill Professional, 1998.

[2] K. L. Choy. Chemical vapour deposition of coatings. *Progress in Materials Science*, 48(2):57 – 170, 2003.

[3] W.S. Rees. *CVD of Nonmetals*. VCH Weinheim, 1996.

[4] Clarke D.R. Chambers, M.D. Doped oxides for high-temperature luminescence and lifetime thermometry. *Annual Review of Materials Research*, 39:325–359, 2009. cited By (since 1996) 0.

[5] C. Pflitsch, A. Muhsin, U. Bergmann, and B. Atakan. Growth of thin aluminium oxide films on stainless steel by MOCVD at ambient pressure and by using a hot-wall CVD-setup. *Surface and Coatings Technology*, 201(1-2):73–81, 2006.

[6] özgür, Y.I. Alivov, C. Liu, A. Teke, MA Reshchikov, S. Doğan, V. Avrutin, S.J. Cho, and H. Morkoc. A comprehensive review of ZnO materials and devices. *Journal of Applied Physics*, 98:041301, 2005.

[7] R.J.H. Clark and RJH Clark. *The chemistry of titanium and vanadium: an introduction to the chemistry of the early transition elements*. Elsevier, 1968.

[8] M. Cid, N. Stem, C. Brunetti, AF Beloto, and CAS Ramos. Improvements in

anti-reflection coatings for high-efficiency silicon solar cells. *Surface and Coatings Technology*, 106(2-3):117–120, 1998.

[9] I. Moreno, J.J. Araiza, and M. Avendano-Alejo. Thin-film spatial filters. *Optics letters*, 30(8):914–916, 2005.

[10] BS Richards. Single-material TiO2 double-layer antireflection coatings. *Solar Energy Materials and Solar Cells*, 79(3):369–390, 2003.

[11] S. Jäger. Dye-metal oxide composite thin films for decorative applications. *Thin Solid Films*, 286(1-2):154–158, 1996.

[12] F. Vaz, P. Cerqueira, L. Rebouta, SMC Nascimento, E. Alves, P. Goudeau, JP Riviere, K. Pischow, and J. De Rijk. Structural, optical and mechanical properties of coloured TiNxOy thin films. *Thin Solid Films*, 447:449–454, 2004.

[13] JE Gray and B. Luan. Protective coatings on magnesium and its alloys–a critical review. *Journal of alloys and compounds*, 336(1-2):88–113, 2002.

[14] G. Leftheriotis, S. Papaefthimiou, and P. Yianoulis. Development of multilayer transparent conductive coatings. *Solid State Ionics*, 136:655–661, 2000.

[15] G. Haacke. Transparent conducting coatings. *Annual Review of Materials Science*, 7(1):73–93, 1977.

[16] X. Wang, L. Zhi, and K. Mullen. Transparent, conductive graphene electrodes for dye-sensitized solar cells. *Nano Lett*, 8(1):323–327, 2008.

[17] JE Sanchéz, OM Sanchéz, L. Ipaz, W. Aperador, JC Caicedo, C. Amaya, MA Landaverde, F.E. Beltran, J. Muñoz-Saldaña, and G. Zambrano. Mechanical, tribological, and electrochemical behavior of Cr1-xAlxN coatings deposited by rf reactive magnetron co-sputtering method. *Applied Surface Science*, 256(8):2380–2387, 2010.

[18] YL Su and WH Kao. Tribological behavior and wear mechanisms of Ti-C: H/TiC/TiCN/TiN/Ti coatings when sliding against steel, bronze and aluminum alloy rods. *Journal of Materials Science*, 36(1):189–199, 2001.

[19] A. Beck, JG Bednorz, C. Gerber, C. Rossel, and D. Widmer. Reproducible switching effect in thin oxide films for memory applications. *Applied Physics Letters*, 77:139, 2000.

[20] Z. Liu, C. Lee, V. Narayanan, G. Pei, and E.C. Kan. Metal nanocrystal memories. I. Device design and fabrication. *Electron Devices, IEEE Transactions on*, 49(9):1606–1613, 2002.

[21] Hadis Morkoc and Ümit Özgür. *Zinc oxide: fundamentals, materials and device technology*. Vch Verlagsgesellschaft Mbh, 2009.

[22] B. Szyszka. Transparent and conductive aluminum doped zinc oxide films prepared by mid-frequency reactive magnetron sputtering. *Thin Solid Films*, 351(1-2):164–169, 1999. cited By (since 1996) 77.

[23] Rech B. Houben L. Wieder S. Schöpe G. Beneking C. Wagner H. Löffl A. Schock H.W. Kluth, O. Texture etched zno:al coated glass substrates for silicon based thin film solar cells. *Thin Solid Films*, 351(1-2):247–253, 1999. cited By (since 1996) 191.

[24] Yan F P Koki K Sasa S Yano M, Ogata K and Inoue. *Mater. Res. Soc. Symp. Proc.*, M:744 75, 2003.

[25] G. Torres Delgado, C.I. Zúñiga Romero, S.A. Mayén Hernández, R. Castanedo Pérez, and O. Zelaya Angel. Optical and structural properties of the sol-gel-prepared zno thin films and their effect on the photocatalytic activity. *Solar Energy Materials and Solar Cells*, 93(1):55 – 59, 2009. Selected Papers from

the Photovoltaics, Solar Energy Materials & Thin Films Symposium, Cancun, Mexico, 19 - 23 August 2007, XVI International Materials Research Congress.

[26] JH Lee, SY Lee, and BO Park. Fabrication and characteristics of transparent conducting In 2 O 3–ZnO thin films by ultrasonic spray pyrolysis. *Mater. Sci. Eng. B*, 127:267–271, 2006.

[27] Cho N.-I. Yun E.-J. Nam H.G. Lee, K.-H. Characterization of zno thin films grown on various substrates by rf magnetron sputtering. *Applied Surface Science*, 256(13):4241–4245, 2010. cited By (since 1996) 0.

[28] H.O. Pierson. *Handbook of chemical vapor depostion [ie deposition](CVD): principles, technology, and applications.* William Andrew, 1999.

[29] Kamei H. Tanizawa-M. Shiosaki T.-Kawabata A. Shimizu, M. Low temperature growth of zno film by photo-mocvd. *Journal of Crystal Growth*, 89(4):365–370, 1988. cited By (since 1996) 20.

[30] Monma A. Shiosaki-T. Kawabata A.-Yamamoto Y. Shimizu, M. Effects of uv light irradiation on the growth of zno films. *Journal of Crystal Growth*, 94(4):895–900, 1989. cited By (since 1996) 2.

[31] Chou P.C. Li-Q.L. Taraldsen G.S.-Ignatiev A. Zhong, Q. High-rate growth of purely a-axis oriented ybco high-tc thin films by photo-assisted mocvd. *Physica C: Superconductivity and its applications*, 246(3-4):288–296, 1995. cited By (since 1996) 20.

[32] Michio Arai Kazuo Nishiyama and Naozo Watanabe. Radiation annealing of boron-implanted silicon with a halogen lamp. *Jpn. J. Appl. Phys*, 19:563–566, 1980.

[33] Xiangping Li, Baolin Zhang, Huichao Zhu, Xin Dong, Xiaochuan Xia, Yongguo Cui, Keke Huang, and Guotong Du. Properties of zno thin films grown on silicon

substrates by photo-assisted metalorganic chemical vapor deposition. *Applied Surface Science*, 254(7):2081 – 2084, 2008.

[34] U. Diebold. The surface science of titanium dioxide. *Surface Science Reports*, 48(5-8):53–229, 2003.

[35] MC Garcia-Alonso, L. Saldana, G. Valles, JL Gonzalez-Carrasco, J. Gonzalez-Cabrero, ME Martinez, E. Gil-Garay, and L. Munuera. In vitro corrosion behaviour and osteoblast response of thermally oxidised Ti6Al4V alloy. *Biomaterials*, 24(1):19–26, 2003.

[36] H. Selhofer. Vacuum Thin Films, 1999.

[37] O. Enea, J. Moser, and M. Grätzel. Achievement of incident photon to electric current conversion yields exceeding 80% in the spectral sensitization of titanium dioxide by coumarin. *Journal of Electroanalytical Chemistry*, 259(1-2):59–65, 1989.

[38] A. Hagfeldt, B. Didriksson, T. Palmqvist, H. Lindström, S. Södergren, H. Rensmo, and S.E. Lindquist. Verification of high efficiencies for the grätzel-cell. a 7efficient solar cell based on dye-sensitized colloidal tio2 films. *Solar Energy Materials and Solar Cells*, 31(4):481–488, 1994.

[39] S.A. Akbar and C.C. Wang. *Electrochem. Soc. Interface*, 5:41, 1996.

[40] G. Vandrish. Ceramic Applications in Gas and Humidity Sensors. *Key Engineering Materials*, 122:185–224, 1996.

[41] Y. Choi, S. Yamamoto, T. Umebayashi, and M. Yoshikawa. Fabrication and characterization of anatase TiO2 thin film on glass substrate grown by pulsed laser deposition. *Solid State Ionics*, 172(1-4):105–108, 2004.

[42] C. Giolli, F. Borgioli, A. Credi, A.D. Fabio, A. Fossati, M.M. Miranda, S. Parmeggiani, G. Rizzi, A. Scrivani, S. Troglio, et al. Characterization of

TiO2 coatings prepared by a modified electric arc-physical vapour deposition system. *Surface and Coatings Technology*, 202(1):13–22, 2007.

[43] M. Adachi, Y. Murata, I. Okada, and S. Yoshikawa. Formation of titania nanotubes and applications for dye-sensitized solar cells. *Journal of the Electrochemical Society*, 150:G488, 2003.

[44] Y. Chen, J.C. Crittenden, S. Hackney, L. Sutter, and D.W. Hand. Preparation of a Novel TiO2-Based p- n Junction Nanotube Photocatalyst. *Environ. Sci. Technol*, 39(5):1201–1208, 2005.

[45] S. Ngamsinlapasathian, S. Sakulkhaemaruethai, S. Pavasupree, A. Kitiyanan, T. Sreethawong, Y. Suzuki, and S. Yoshikawa. Highly efficient dye-sensitized solar cell using nanocrystalline titania containing nanotube structure. *Journal of Photochemistry and Photobiology A: Chemistry*, 164(1-3):145–151, 2004.

[46] V. Gauthier, S. Bourgeois, P. Sibillot, M. Maglione, and M. Sacilotti. Growth and characterization of AP-MOCVD iron doped titanium dioxide thin films. *Thin Solid Films*, 340(1-2):175–182, 1999.

[47] M. Satou F. Fijimoto S. Miyaki, T. Kobayashi. *J. Vac. Sci. Technol*, A 9:3036, 1991.

[48] MO Abou-Helal and WT Seeber. Preparation of TiO2 thin films by spray pyrolysis to be used as a photocatalyst. *Applied Surface Science*, 195(1-4):53–62, 2002.

[49] D. Mardare, M. Tasca, M. Delibas, and GI Rusu. On the structural properties and optical transmittance of TiO2 rf sputtered thin films. *Applied Surface Science*, 156(1-4):200–206, 2000.

[50] H. Dong and T. Bell. Enhanced wear resistance of titanium surfaces by a new thermal oxidation treatment. *Wear*, 238(2):131–137, 2000.

[51] J.C. Yu, J. Yu, and J. Zhao. Enhanced photocatalytic activity of mesoporous and ordinary TiO2 thin films by sulfuric acid treatment. *Applied Catalysis B: Environmental*, 36(1):31–43, 2002.

[52] B. Samuneva, V. Kozhukharov, C. Trapalis, and R. Kranold. Sol-gel processing of titanium-containing thin coatings. *Journal of Materials Science*, 28(9):2353–2360, 1993.

[53] RF Bunshah. Handbook of Deposition Technology for Films and Coatings," Noyes Publication. *Inc., Park Ridge, NJ*, 1994.

[54] T.K. Toivo and JH Mark. The Chemistry of metal CVD, 1994.

[55] M.J. Hampden-Smith and T.T. Kodas. Chemical vapor deposition of metals: Part 1. An overview of CVD processes. *Chemical Vapor Deposition*, 1(1):8–23, 1995.

[56] M.A. Siddiqi, R.A. Siddiqui, and B. Atakan. Thermal stability, sublimation pressures and diffusion coefficients of some metal acetylacetonates. *Surface and Coatings Technology*, 201(22-23):9055–9059, 2007.

[57] C. Shaoqiang, Z. Jian, F. Xiao, W. Xiaohua, et al. Nanocrystalline ZnO thin films on porous silicon/silicon substrates obtained by sol-gel technique. *Applied Surface Science*, 241(3-4):384–391, 2005.

[58] Y.S. Kim, W.P. Tai, and S.J. Shu. Effect of preheating temperature on structural and optical properties of ZnO thin films by sol-gel process. *Thin Solid Films*, 491(1-2):153–160, 2005.

[59] R. Ghosh, B. Mallik, S. Fujihara, and D. Basak. Photoluminescence and photoconductance in annealed ZnO thin films. *Chemical Physics Letters*, 403(4-6):415–419, 2005.

[60] Saiki H. Takahashi Y. Ohya, Y. Preparation of transparent, electrically con-

ducting zno film from zinc acetate and alkoxide. *Journal of Materials Science*, 29(15):4099–4103, 1994. cited By (since 1996) 61.

[61] Sasaki C. Kimura T. Fujihara, S. Crystallization behavior and origin of c-axis orientation in sol-gel-derived zno:li thin films on glass substrates. *Applied Surface Science*, 180(3-4):341–350, 2001. cited By (since 1996) 86.

[62] C.J. Brinker and G.W. Scherer. *Sol-gel science: the physics and chemistry of sol-gel processing*. Academic Pr, 1990.

[63] A.C. Pierre. *Introduction to sol-gel processing*. Springer Netherlands, 1998.

[64] D. Shi. *Functional thin films and functional materials: new concepts and technologies*. Springer, 2003.

[65] H. Takikawa and H. Tanoue. Review of cathodic arc deposition for preparing droplet-free thin films. *Plasma Science, IEEE Transactions on*, 35(4):992–999, 2007.

[66] R.L. Boxman, D.M. Sanders, and P.J. Martin. *Handbook of vacuum arc science and technology: fundamentals and applications*. William Andrew Publishing, 1995.

[67] BK Tay, ZW Zhao, and DHC Chua. Review of metal oxide films deposited by filtered cathodic vacuum arc technique. *Materials Science and Engineering: R: Reports*, 52(1-3):1–48, 2006.

[68] S. Anders, A. Anders, M. Rubin, Z. Wang, S. Raoux, F. Kong, and I.G. Brown. Formation of metal oxides by cathodic arc deposition. *Surface and Coatings Technology*, 76-77(Part 1):167 – 173, 1995.

[69] J. Vetter, HJ Scholl, and O. Knotek. (TiCr) N coatings deposited by cathodic vacuum arc evaporation. *Surface and Coatings Technology*, 74:286–291, 1995.

[70] I.G. Brown. Cathodic arc deposition of films. *Annual Review of Materials Science*, 28(1):243–269, 1998.

[71] D.M. Sanders and A. Anders. Review of cathodic arc deposition technology at the start of the new millennium. *Surface and Coatings Technology*, 133:78–90, 2000.

[72] J. Charles A. Evans und S. Wilson C. Brundle. *Encyclopedia of Materials Charakterisation.* Butterworth-Heinemann, Boston, 1992.

[73] CR Brundle, C.A. Evans, and S. Wilson. *Encyclopedia of Materials Characterization: surfaces, interfaces, thin films.* Gulf Professional Publishing, 1992.

[74] L. Reimer. *Scanning electron microscopy: physics of image formation and microanalysis.* Springer Verlag, 1998.

[75] R.F. Egerton. *Physical principles of electron microscopy: an introduction to TEM, SEM, and AEM.* Springer, 2005.

[76] A.J. Garratt-Reed and D.C. Bell. *Energy-dispersive X-ray analysis in the electron microscope.* Garland Science, 2003.

[77] L.I. Maissel, R. Glang, and P.P. Budenstein. Handbook of thin film technology. *Journal of The Electrochemical Society*, 118:114C, 1971.

[78] H.B. Bebb and EW Williams. Semiconductors and Semimetals, edited by RK Willardson and AC Beer (Academic, New York, 1972). *Vol*, 8:182–392.

[79] J.I. Pankove. *Optical processes in semiconductors.* dover publications, 1975.

[80] A.H. Khalid and K. Kontis. Thermographic phosphors for high temperature measurements: principles, current state of the art and recent applications. *Sensors*, 8(9):5673–5744, 2008.

[81] SW Allison and GT Gillies. Remote thermometry with thermographic phos-

phors: instrumentation and applications. *Review of Scientific Instruments*, 68(7):2615–2650, 2009.

[82] W.M. Yen, S. Shionoya, and H. Yamamoto. *Phosphor handbook*. CRC Press Boca Raton, 2007.

[83] J. Brübach, J. Janicka, and A. Dreizler. An algorithm for the characterisation of multi-exponential decay curves. *Optics and Lasers in Engineering*, 47(1):75 – 79, 2009.

[84] LJ Dowell and GT Gillies. Precision limits of lifetime estimation algorithms as determined by Monte Carlo simulation: A comparison of theory and experiment. *Review of scientific instruments*, 59(8):1310–1315, 1988.

[85] T. Sun, ZY Zhang, KTV Grattan, and AW Palmer. Analysis of double exponential fluorescence decay behavior for optical temperature sensing. *Review of scientific instruments*, 68(1):58–63, 1997.

[86] A. Omrane. *Thermometry using laser-induced emission from thermographic phosphors: development and applications in combustion*. KFS AB,, 2005.

[87] K. Levenberg. A method for the solution of certain problems in least squares. *Quarterly of Applied Mathematics*, 2:164–168, 1944.

[88] DW Marquardt. An algorithm for least-squares estimation of nonlinear inequalities. *Siam J. Appl. Math*, 11:431–441, 1963.

[89] Eckert Christopher. *Thermographische Phosphorschichten auf Basis von dotiertem Al2O3 und dotiertem Yttrium stabilisiertem ZrO2: Hergestellt mit CVD- und Sol-Gel-Verfahren*. PhD thesis, Fakultät für Ingenieurwissenschaften » Ingenieurwissenschaften - Campus Duisburg » Abteilung Maschinenbau » Institut für Verbrennung und Gasdynamik, 2010.

[90] FM Smits. Measurement of sheet resistivities with the four-point probe. *Bell Syst. Tech. J*, 37(3):711–18, 1958.

[91] D.K. Schroder. *Semiconductor material and device characterization.* Wiley-IEEE Press, 2006.

[92] FM Smits. Measurement of sheet resistivities with the four-point probe. *Bell Syst. Tech. J*, 37(3):711–718, May,1958.

[93] M.G. Buehler and W.R. Thurber. Measurement of the resistivity of a thin square sample with a square four-probe array. *Solid-State Electronics*, 20(5):403–406, 1977.

[94] D.S. Perloff. Four-point sheet resistance correction factors for thin rectangular samples. *Solid-State Electronics*, 20(8):681–687, 1977.

[95] M. Ohring. *The materials science of thin films: deposition and structure.* Academic Pr, 2002.

[96] D.R. Lide. *CRC handbook of chemistry and physics: a ready-reference book of chemical and physical data.* CRC Pr I Llc, 2004.

[97] CX Xu, XW Sun, ZL Dong, and MB Yu. Zinc oxide nanodisk. *Applied Physics Letters*, 85:3878, 2004.

[98] WI Park, YH Jun, SW Jung, and G.C. Yi. Excitonic emissions observed in ZnO single crystal nanorods. *Applied Physics Letters*, 82:964, 2003.

[99] H.T. Ng, J. Li, M.K. Smith, P. Nguyen, A. Cassell, J. Han, and M. Meyyappan. Growth of epitaxial nanowires at the junctions of nanowalls. *Science*, 300(5623):1249, 2003.

[100] Jinsu Yoo, Jeonghul Lee, Seokki Kim, Kyunghoon Yoon, I. Jun Park, S.K. Dhungel, B. Karunagaran, D. Mangalaraj, and Junsin Yi. High transmittance

and low resistive zno:al films for thin film solar cells. *Thin Solid Films*, 480-481:213 – 217, 2005. EMRS 2004.

[101] M.A. Contreras, B. Egaas, K. Ramanathan, J. Hiltner, A. Swartzlander, F. Hasoon, and R. Noufi. Progress toward 20% efficiency in Cu (In, Ga) Se2 polycrystalline thin-film solar cells. *Progress in Photovoltaics: Research and Applications*, 7(4):311–316, 1999.

[102] E. FORTUNATO, D. GINLEY, H. HOSONO, and D.C. PAINE. Transparent conducting oxides for photovoltaics. *MRS bulletin*, 32(3):242–247, 2007.

[103] S. Flickyngerova, R. Ovadekova, I. Novotny, V. Tvarozek, J. Labuda, V. Breternitz, and Ch. Knedlik. Preparation of nanostructured thin-film interfaces applicable in biosensors. *Vacuum*, 82(2):303 – 306, 2007. Proceedings of the 11th Joint Vacuum Conference (JVC-11).

[104] Oleg Lupan, Sergiu Shishiyanu, Lee Chow, and Teodor Shishiyanu. Nanostructured zinc oxide gas sensors by successive ionic layer adsorption and reaction method and rapid photothermal processing. *Thin Solid Films*, 516(10):3338 – 3345, 2008.

[105] B. Wacogne, MP Roe, TJ Pattinson, and CN Pannell. Effective piezoelectric activity of zinc oxide films grown by radio-frequency planar magnetron sputtering. *Applied Physics Letters*, 67:1674, 1995.

[106] Q. Wang, Y. Qin, G.J. Xu, L. Chen, Y. Li, L. Duan, Z.X. Li, Y.L. Li, and P. Cui. Low-voltage zno varistor fabricated by the solution-coating method. *Ceramics International*, 34(7):1697 – 1701, 2008.

[107] Hui Lu, Yuele Wang, and Xian Lin. Structures, varistor properties, and electrical stability of zno thin films. *Materials Letters*, 63(27):2321 – 2323, 2009.

[108] C. Yang, K. Hong, J. Jang, D.S. Chung, T.K. An, W.S. Choi, and C.E. Park.

Solution-processed flexible ZnO transparent thin-film transistors with a polymer gate dielectric fabricated by microwave heating. *Nanotechnology*, 20:465201, 2009.

[109] Sylvie Faÿ, Jérôme Steinhauser, Sylvain Nicolay, and Christophe Ballif. Polycrystalline zno: B grown by lpcvd as tco for thin film silicon solar cells. *Thin Solid Films*, 518(11):2961 – 2966, 2010. Transparent Oxides for Electronics and Optiocs (TOEO-6).

[110] J. Winkler and S. Marmé. Titania as a sorbent in normal-phase liquid chromatography* 1. *Journal of Chromatography A*, 888(1-2):51–62, 2000.

[111] G. San Vicente, A. Morales, and M. T. Gutierrez. Preparation and characterization of sol-gel tio2 antireflective coatings for silicon. *Thin Solid Films*, 391(1):133 – 137, 2001.

[112] R. Adams. TiO2: A brillant future. *European coatings journal*, (6):395–398, 1996.

[113] A.E.Muhsin. *Titel.* PhD thesis, University of Duisburg-Essen, 2007.

[114] S.L. Flegler, J.W. Heckman, and K.L. Klomparens. *Scanning and transmission electron microscopy: an introduction.* WH Freeman New York, 1993.

[115] S.L. Flegler, J.W. Heckman, and K.L. Klomparens. *Elektronenmikroskopie.* Spektrum Akad. Verl., 1995.

[116] C. Pflitsch, B. Curdts, V. Buck, and B. Atakan. Wear properties of MOCVD-grown aluminium oxide films studied by cavitation erosion experiments. *Surface and Coatings Technology*, 201(22-23):9299–9303, 2007.

[117] H. Ollendorf and D. Schneider. A comparative study of adhesion test methods for hard coatings. *Surface and coatings technology*, 113(1-2):86–102, 1999.

[118] Astm g32-98- standard test method for cavitation erosion using vibratory apparatus (1998).

[119] Y.C. Huang, Z.Y. Li, H. Chen, W.Y. Uen, S.M. Lan, S.M. Liao, Y.H. Huang, C.T. Ku, M.C. Chen, T.N. Yang, et al. Characterizations of gallium-doped ZnO films on glass substrate prepared by atmospheric pressure metal-organic chemical vapor deposition. *Thin Solid Films*, 517(18):5537–5542, 2009.

[120] XL Chen, BH Xu, JM Xue, Y. Zhao, CC Wei, J. Sun, Y. Wang, XD Zhang, and XH Geng. Boron-doped zinc oxide thin films for large-area solar cells grown by metal organic chemical vapor deposition. *Thin Solid Films*, 515(7-8):3753–3759, 2007.

[121] B.Y. Oh, M.C. Jeong, D.S. Kim, W. Lee, and J.M. Myoung. Post-annealing of Al-doped ZnO films in hydrogen atmosphere. *Journal of Crystal Growth*, 281(2-4):475–480, 2005.

[122] R.W. Birkmire and E. Eser. Polycrystalline thin film solar cells: Present status and future potential. *Annual Review of Materials Science*, 27(1):625–653, 1997.

[123] WJ Jeong, SK Kim, and GC Park. Preparation and characteristic of ZnO thin film with high and low resistivity for an application of solar cell. *Thin Solid Films*, 506:180–183, 2006.

[124] S. Roy and S. Basu. Improved zinc oxide film for gas sensor applications. *Bulletin of Materials Science*, 25(6):513–515, 2002.

[125] Yinzhen Wang, Haili Wang, Shuzhi Li, Shengming Zhou, Ying Hang, Jun Xu, Jiandong Ye, Shulin Gu, and Rong Zhang. Annealing effect on properties of zno thin films grown on linbo3 substrates by mocvd. *Journal of Crystal Growth*, 284(3-4):319 – 323, 2005.

[126] Dong Chan Kim, Bo Hyun Kong, Sang Ouk Jun, Hyung Koun Cho, Dong Jun

Park, and Jeong Yong Lee. Pressure dependence and micro-hillock formation of zno thin films grown at low temperature by mocvd. *Thin Solid Films*, 516(16):5562 – 5566, 2008. Thin Films 2006, Singapore.

[127] A. Dadgar, N. Oleynik, D. Forster, S. Deiter, H. Witek, J. Bläsing, F. Bertram, A. Krtschil, A. Diez, J. Christen, and A. Krost. A two-step metal organic vapor phase epitaxy growth method for high-quality zno on gan/al2o3 (0 0 0 1). *Journal of Crystal Growth*, 267(1-2):140 – 144, 2004.

[128] J.S. Kim, H.A. Marzouk, P.J. Reucroft, and C.E. Hamrin Jr. Characterization of high quality c axis oriented zno thin films grown by metal organic chemical vapor deposition using zinc acetate as source material. *Thin Solid Films*, 217(1-2):133 – 137, 1992.

[129] Y. Kashiwaba, K. Sugawara, K. Haga, H. Watanabe, B. P. Zhang, and Y. Segawa. Characteristics of c-axis oriented large grain zno films prepared by low-pressure mo-cvd method. *Thin Solid Films*, 411(1):87 – 90, 2002.

[130] Natsume Y. Hirayama T. Sakata H. Ogawa, M.F. Preparation and electrical properties of undoped zinc oxide films by cvd. *Journal of Materials Science Letters*, 9(11):1351–1353, 1990. cited By (since 1996) 24.

[131] K. Kamata, J. Nishino, S. Ohshio, K. Maruyama, and M. Ohtuki. Rapid Formation of Zinc Oxide Films by an Atmospheric-Pressure Chemical Vapor Deposition Method. *Journal of the American Ceramic Society*, 77(2):505–508, 1994.

[132] D.R. Lide. *CRC handbook of chemistry and physics.* CRC press, 1993.

[133] Christian Pflitsch, Dorothee Viefhaus, Ulf Bergmann, and Burak Atakan. Organometallic vapour deposition of crystalline aluminium oxide films on stainless steel substrates. *Thin Solid Films*, 515(7-8):3653 – 3660, 2007.

[134] T. Arii and A. Kishi. Humidity controlled thermal analysis. *Journal of Thermal Analysis and Calorimetry*, 83(1):253–260, 2006.

[135] T. MARUYAMA and A. NAKAI. *J. Appl. Phys*, 28:L346, 1989.

[136] T. Maruyama and J. Shionoya. Zinc oxide thin films prepared by chemical vapour deposition from zinc acetate. *Journal of Materials Science Letters*, 11(3):170–172, 1992.

[137] Rakhi Khandelwal, Amit Pratap Singh, Avinashi Kapoor, Sorin Grigorescu, Paola Miglietta, Nadya Evgenieva Stankova, and Alessio Perrone. Effects of deposition temperature on the structural and morphological properties of thin zno films fabricated by pulsed laser deposition. *Optics & Laser Technology*, 40(2):247 – 251, 2008.

[138] P. Prepelita, R. Medianu, F. Garoi, N. Stefan, and F. Iacomi. On the structural and electrical characteristics of zinc oxide thin films. *Thin Solid Films*, 518(16):4615–4618, 2010.

[139] JC Lodder, T. Wielinga, and J. Worst. Rf-sputtered Co-Cr layers for perpendicular magnetic recording I: Structural properties. *Thin solid films*, 101(1):61–73, 1983.

[140] Zhaohui Qiao, Chitra Agashe, and Dieter Mergel. Dielectric modeling of transmittance spectra of thin zno:al films. *Thin Solid Films*, 496(2):520 – 525, 2006.

[141] AF Aktaruzzaman, GL Sharma, and LK Malhotra. Electrical, optical and annealing characteristics of ZnO: Al films prepared by spray pyrolysis. *Thin Solid Films*, 198(1-2):67–74, 1991.

[142] K. Ellmer. Resistivity of polycrystalline zinc oxide films: current status and physical limit. *Journal of Physics D: Applied Physics*, 34:3097, 2001.

[143] Y. Igasaki and H. Saito. The effects of deposition rate on the structural and

electrical properties of ZnO: Al films deposited on (112¯ 0) oriented sapphire substrates. *Journal of Applied Physics*, 70(7):3613–3619, 2009.

[144] Ki Cheol Park, Dae Young Ma, and Kun Ho Kim. The physical properties of al-doped zinc oxide films prepared by rf magnetron sputtering. *Thin Solid Films*, 305(1-2):201 – 209, 1997.

[145] Byeong-Yun Oh, Min-Chang Jeong, Woong Lee, and Jae-Min Myoung. Properties of transparent conductive zno:al films prepared by co-sputtering. *Journal of Crystal Growth*, 274(3-4):453 – 457, 2005.

[146] W. Tang and D.C. Cameron. Aluminum-doped zinc oxide transparent conductors deposited by the sol-gel process. *Thin Solid Films*, 238(1):83 – 87, 1994.

[147] YG Wang, SP Lau, HW Lee, SF Yu, BK Tay, XH Zhang, KY Tse, and HH Hng. Comprehensive study of ZnO films prepared by filtered cathodic vacuum arc at room temperature. *Journal of Applied Physics*, 94:1597, 2003.

[148] R. Al Asmar, JP Atanas, M. Ajaka, Y. Zaatar, G. Ferblantier, JL Sauvajol, J. Jabbour, S. Juillaget, and A. Foucaran. Characterization and Raman investigations on high-quality ZnO thin films fabricated by reactive electron beam evaporation technique. *Journal of crystal growth*, 279(3-4):394–402, 2005.

[149] J. Tauc. Amorphous and liquid semiconductors. 1974.

[150] NF Mott, EA Davis, and RA Street. States in the gap and recombination in amorphous semiconductors. *Philosophical Magazine*, 32(5):961–996, 1975.

[151] S.T. Tan, B.J. Chen, X.W. Sun, X. Hu, X.H. Zhang, and S.J. Chua. Properties of polycrystalline zno thin films by metal organic chemical vapor deposition. *Journal of Crystal Growth*, 281(2-4):571 – 576, 2005.

[152] E. Ziegler, A. Heinrich, H. Oppermann, and G. Stöver. Electrical properties and

non-stoichiometry in ZnO single crystals. *physica status solidi (a)*, 66(2):635–648, 1981.

[153] BE Sernelius, K.F. Berggren, Z.C. Jin, I. Hamberg, and CG Granqvist. Band-gap tailoring of ZnO by means of heavy Al doping. *Physical Review B*, 37(17):10244–10248, 1988.

[154] ST Tan, BJ Chen, XW Sun, WJ Fan, HS Kwok, XH Zhang, and SJ Chua. Blueshift of optical band gap in ZnO thin films grown by metal-organic chemical-vapor deposition. *Journal of Applied Physics*, 98:013505, 2005.

[155] ST Tan, BJ Chen, XW Sun, WJ Fan, HS Kwok, XH Zhang, and SJ Chua. Blueshift of optical band gap in ZnO thin films grown by metal-organic chemical-vapor deposition. *Journal of Applied Physics*, 98:013505, 2005.

[156] M.E. Fragalà, G. Malandrino, M.M. Giangregorio, M. Losurdo, G. Bruno, S. Lettieri, L.S. Amato, and P. Maddalena. Structural, Optical, and Electrical Characterization of ZnO and Al-doped ZnO Thin Films Deposited by MOCVD. *Chemical Vapor Deposition*, 15(10-12):327–333, 2009.

[157] C. Gumus, OM Ozkendir, H. Kavak, and Y. Ufuktepe. Structural and optical properties of zinc oxide thin films prepared by spray pyrolysis method. *Journal of optoelectronics and advanced materials*, 8(1):299, 2006.

[158] YG Wang, SP Lau, HW Lee, SF Yu, BK Tay, XH Zhang, KY Tse, and HH Hng. Comprehensive study of ZnO films prepared by filtered cathodic vacuum arc at room temperature. *Journal of Applied Physics*, 94:1597, 2003.

[159] YW Chen, YC Liu, SX Lu, CS Xu, CL Shao, C. Wang, JY Zhang, YM Lu, DZ Shen, and XW Fan. Optical properties of ZnO and ZnO: In nanorods assembled by sol-gel method. *The Journal of chemical physics*, 123:134701, 2005.

[160] J.V. Hoene, R.G. Charles, and W.M. Hickam. Thermal Decomposition of Metal

Acetylacetonates: Mass Spectrometer Studies. *The Journal of Physical Chemistry*, 62(9):1098–1101, 1958.

[161] S. V. Sotirchos. Effects of residence time and reaction conditions on the deposition of silica, alumina, and aluminosilicates from ch3sicl3, alcl3, co2, and h2 mixtures. *Chem. Vap. Deposition*, 7, No. 4:157–166, 2001.

[162] Y. Natsume and H. Sakata. Electrical conductivity and optical properties of ZnO films annealed in hydrogen atmosphere after chemical vapor deposition. *Journal of Materials Science: Materials in Electronics*, 12(2):87–92, 2001.

[163] N.P. Dasgupta, S. Neubert, W. Lee, O. Trejo, J.R. Lee, and F.B. Prinz. Atomic Layer Deposition of Al-doped ZnO Films: Effect of Grain Orientation on Conductivity. *Chemistry of Materials*, 2010.

[164] ZQ Xu, H. Deng, Y. Li, QH Guo, and YR Li. Characteristics of Al-doped c-axis orientation ZnO thin films prepared by the sol-gel method. *Materials Research Bulletin*, 41(2):354–358, 2006.

[165] K.H. Kim, K.C. Park, and D.Y. Ma. Structural, electrical and optical properties of aluminum doped zinc oxide films prepared by radio frequency magnetron sputtering. *Journal of Applied Physics*, 81(12):7764–7772, 2009.

[166] M. Chen, X. Wang, YH Yu, ZL Pei, XD Bai, C. Sun, RF Huang, and LS Wen. X-ray photoelectron spectroscopy and auger electron spectroscopy studies of Al-doped ZnO films. *Applied Surface Science*, 158(1-2):134–140, 2000.

[167] T. Minami, S. Suzuki, and T. Miyata. Transparent conducting impurity-co-doped ZnO: Al thin films prepared by magnetron sputtering. *Thin solid films*, 398:53–58, 2001.

[168] Jianguo Lu, Zhizhen Ye, Jingyun Huang, Lei Wang, and Binghui Zhao. Synthesis

and properties of zno films with (1 0 0) orientation by ss-cvd. *Applied Surface Science*, 207(1-4):295 – 299, 2003.

[169] S.Y. Kuo, W.C. Chen, and C.P. Cheng. Investigation of annealing-treatment on the optical and electrical properties of sol-gel-derived zinc oxide thin films. *Superlattices and Microstructures*, 39(1-4):162–170, 2006.

[170] E. Burstein. Anomalous optical absorption limit in InSb. *Physical Review*, 93(3):632–633, 1954.

[171] H. W. Lee, S. P. Lau, Y. G. Wang, K. Y. Tse, H. H. Hng, and B. K. Tay. Structural, electrical and optical properties of al-doped zno thin films prepared by filtered cathodic vacuum arc technique. *Journal of Crystal Growth*, 268(3-4):596 – 601, 2004. ICMAT 2003, Symposium H, Compound Semiconductors in Electronic an d Optoelectronic Applications.

[172] GG Rusu, M. Girtan, and M. Rusu. Preparation and characterization of ZnO thin films prepared by thermal oxidation of evaporated Zn thin films. *Superlattices and Microstructures*, 42(1-6):116–122, 2007.

[173] Viefhaus D. Atakan B. Pflitsch, C. Cvd of thin ruby films on si(100) and stainless steel for surface temperature sensor applications. *Chemical Vapor Deposition*, 13(8):420–426, 2007. cited By (since 1996) 9.

[174] B. Atakan . C. Pflitsch, R.A. Siddiqui. Phosphorescence properties of sol-gel derived ruby measured as functions of temperature and cr3+ content. *Applied Physics A: Materials Science and Processing*, 90(3):527–532, 2008. cited By (since 1996) 8.

[175] C. Legrand-Buscema, C. Malibert, and S. Bach. Elaboration and characterization of thin films of TiO2 prepared by sol-gel process. *Thin solid films*, 418(2):79–84, 2002.

[176] G. Blasse and B.C. Grabmaier. *Luminescent materials.* Springer-Verlag Berlin, 1994.

[177] T. Kano. *Principal phosphor materials and their optical properties, in Phosphor Handbook.* 2006.

[178] H. Aizawa, H. Uchiyama, T. Katsumata, S. Komuro, T. Morikawa, H. Ishizawa, and E. Toba. Fibre-optic thermometer using sensor materials with long fluorescence lifetime. *Measurement Science and Technology*, 15:1484, 2004.

[179] D. Siva Rama Krishna and Y. Sun. Effect of thermal oxidation conditions on tribological behaviour of titanium films on 316L stainless steel. *Surface and Coatings Technology*, 198(1-3):447–453, 2005.

[180] D. Krishna and Y. Sun. Thermally oxidised rutile-TiO2 coating on stainless steel for tribological properties and corrosion resistance enhancement. *Applied Surface Science*, 252(4):1107–1116, 2005.

[181] RA Lula. Stainless steel. 1985.

[182] D. Peckner and I.M. Bernstein. *Handbook of stainless steels.* McGraw-Hill, 1977.

[183] D. Siva Rama Krishna and Y. Sun. Effect of thermal oxidation conditions on tribological behaviour of titanium films on 316L stainless steel. *Surface and Coatings Technology*, 198(1-3):447–453, 2005.

Curriculum Vitae

Personal data

Name	Nebatti Ech-Chergui Abdelkader
Date and Place of birth	7^{th}January 1975, Oran, Algeria
Nationality	Algerian
Marital satus	Single

Education

From 02/2008	Ph.D Student, chair of Thermodynamics, Institute of combustion and gas dynamics, department of mechanical engineering, university of duisburg-essen, campus duisburg (Germany)
09/2001-10/2004	Magister degree of Physic, department of physic in es-senia oran university (Algeria)
10/1994-06/2000	High studies diploma in physic(Option: Condensed matter), department of physic in es-senia oran university (Algeria)
09/1991-06/1994	High school certificate (Baccalaureat), el karma high school, Oran (Algeria)

Publications

1. Abdelkader Nebatti, Christian Pflitsch, Christopher Eckert, Burak Atakan. Sol-Gel-Deposition of thin TiO_2: Eu^{3+} thermographic phosphor films. *Progress in Organic Coatings* 67: 356-360, 2010
2. Abdelkader E. Nebatti, Christian Pflitsch, Christopher Eckert, Burak Atakan. Rapid thermal (RT) MOCVD of undoped and Al doped ZnO thin films. *ECS Transactions* 25: 459-465, 2009